Unveiling the exoplanetary atmospheres

using ground-based high-resolution transmission spectroscopy

Dissertation with the aim of achieving a doctoral degree
in the
Faculty of Mathematics, Informatics and Natural Sciences

Department of Physics
Hamburg University

Submitted by
Sara Khalafinejad

Hamburg
December 2017

Day of oral defense: 15.02.2018

Evaluators of the dissertation:
Prof. Dr. Jürgen Schmitt
Prof. Dr. Stefan Dreizler

Evaluators of the defense:
Prof. Dr. Jochen Liske
Prof. Dr. Jürgen Schmitt
Prof. Dr. Stefan Dreizler
Prof. Dr. Robi Banerjee
Prof. Dr. Manuel Güdel

"I would rather discover a new cause of nature than be the King of Persia"

Democritus

Abstract

With several thousand exoplanets discovered to date we are now entering the era of an in-depth characterization of these worlds. Studying exoplanetary atmospheres is crucial for understanding planet formation and evolution, and to find an extraterrestrial habitable environment. Transmission spectroscopy is a powerful technique to identify chemical compositions and to infer physical properties of transiting exoplanetary atmospheres. One of the main difficulties in this kind of studies is to disentangle the signal of the planet from the one of the star. Due to the large absorption cross sections, atomic sodium is expected to produce a relatively large transmission signal.

My thesis aims at introducing an optimized framework for high-resolution transmission spectroscopy in narrow wavelength bands around the broad atomic lines of sodium.

For this study, transit observations of two hot-Jupiters are selected: HD 189733b, which orbits an active K-type star, is observed using the ultraviolet and visual echelle spectrograph (UVES) at the Very Large Telescope; WASP-17b, which orbits an F-type star, is observed with the Magellan Inamori Kyocera echelle (MIKE) at the Magellen Telescopes. I obtain the excess light curves in narrow passbands of about 1 to 3 Å centered on each sodium line. To extract the exoplanetary absorption signal from these raw light curves, I first model the impeding effects of stellar flaring activity through investigations of the Ca II H&K, H_α, and the Ca II infrared triplet lines. In addition, I take into account the differential limb-darkening of the star. Finally, as the novel component of this light curve modelling I consider the changing planetary radial velocity to explain a "bump" that is typically observed in the atmospheric transit light curves. This leads to the determination of the shape of the exoplanetary sodium line.

Using this approach, I succeed in the detection of sodium in HD 189733b in spite of severe stellar flaring activity. On the contrary, the host star in the WASP-17 system is not showing any strong signature of activity. Therefore, in addition to applying the light curve approach I construct the transmission spectrum of WASP-17b in the region of the sodium lines. The observed spectrum is then compared to a simple planetary atmospheric model, which results in the retrieval of atmospheric parameters such as temperature and radius at 0.1 bar.

This work proofs that the detection of sodium is a diagnosis of the physical properties of exoplanet atmospheres and shows that if changes in radial velocity are considered, it is possible to estimate the shape of the exoplanetary spectral features in the active stars without the need to construct the transmission spectrum. The workflow that is developed in this thesis is ready for a quick application to other exo-worlds.

Zusammenfassung

Mit mehreren tausend bis heute entdeckten Exoplaneten betreten wir nun die Ära einer eingehenden Charakterisierung dieser Welten. Das Studium exoplanetarer Atmosphären ist entscheidend für das Verständnis der Planetenentstehung und -entwicklung sowie für das Auffinden einer auerirdischen habitablen Umgebung. Die Transmissionsspektroskopie ist eine leistungsfähige Technik, um chemische Zusammensetzungen zu identifizieren und physikalische Eigenschaften von bedeckenden exoplanetaren Atmosphären abzuleiten. Eine der Hauptschwierigkeiten bei dieser Art von Studien besteht darin, das Signal des Planeten von dem des Sterns zu separieren. Aufgrund der groen Absorptionsquerschnitte wird erwartet, dass atomares Natrium ein relativ groes Transmissionssignal erzeugt.

Ziel meiner Doktorarbeit ist die Einführung eines optimierten Rahmens für die hochauflösende Transmissionsspektroskopie in schmalen Wellenlängenbereichen um die breiten Atomlinien von Natrium.

Für diese Studie werden Transitbeobachtungen von zwei heien Jupitern ausgewählt: HD-189733b, das einen aktiven Stern vom K-Typ umkreist, wird unter Verwendung des UV- und visuellen Echelle-Spektrographen (UVES) am Very Large Telescope beobachtet; WASP-17b, das einen Stern vom F-Typ umkreist, wird mit dem Magellan Inamori Kyocera Echelle (MIKE) an den Magellenteleskopen beobachtet. Ich erhalte die Lichtexzesskurven in schmalen Durchlabereichen von ungefähr 1 bis 3 AA zentriert auf jeder Natriumlinie. Um das Exoplanetenabsorptionssignal aus diesen rohen Lichtkurven zu extrahieren, modelliere ich zunächst die behindernden Effekte der stellaren Flareaktivität durch Untersuchungen der Ca II H & K, H $_{\alpha}$ - und der Ca II-Infrarottriplettlinien. Auerdem berücksichtige ich die Mitte-Rand-Verdunkelung des Sterns. Als neue Komponente dieser Lichtkurvenmodellierung betrachte ich schlielich die sich ändernde planetare Radialgeschwindigkeit, um einen typischen "Bump" zu erklären, der typischerweise in den atmosphärischen Transitlichtkurven beobachtet wird und zur Bestimmung der Form der exoplanetaren Natriumlinie führt.

Mit diesem Ansatz gelang es mir, Natrium in HD 189733b trotz starker Flareaktivität nachzuweisen. Im Gegensatz dazu zeigt der Heimatstern im WASP-17-System keine starke Aktivitätssignatur. Deshalb konstruiere ich zusätzlich zum Lichtkurvenansatz das Transmissionsspektrum von WASP-17b im Bereich der Natriumlinien. Das beobachtete Spektrum wird dann mit einem einfachen planetarischen Atmosphärenmodell verglichen, das atmosphärische Parameter wie Temperatur und Radius bei 0,1 bar wiedergibt.

Diese Arbeit zeigt, dass die Detektion von Natrium eine Diagnose der physikalischen Eigenschaften der Exoplanetenatmosphäre ist, und dass, wenn Änderungen der Radialgeschwindigkeit berücksichtigt werden, die Form der exoplanetaren Spektraleigenschaften in den aktiven Sternen ohne die Notwendigkeit der Konstruktion des Übertragungsspektrums bestimmt werden kann. Der in dieser Arbeit entwickelte Arbeitsablauf ist bereit für eine schnelle Anwendung auf anderen Exoplaneten.

Persian summary

چکیدهٔ فارسی

شناسایی جو سیارات فراخورشیدی با بهره‌گیری از روش طیف‌بینی زمین‌بنیاد عبوری با توان تفکیک بالا

سارا خلفی‌نژاد

تا به امروز چندین هزار سیارهٔ فراخورشیدی (فراسیاره) کشف شده‌اند و ما اکنون وارد دورهٔ شناخت ژرفتر ویژگی‌های این سیاره‌ها می‌شویم. مطالعهٔ جوّ فراسیاره‌ها برای فهمیدن چگونگی شکل‌گیری و تکامل دیگر سیاره‌ها و همچنین یافتن یک محیط زیست‌پذیر فراتر از زمین بسیار مهم است. طیف‌بینی عبوری یک روش قدرتمند برای شناسایی ترکیب‌های شیمیایی و ارزیابی خواص فیزیکی اتمسفر فراسیاره‌های گذرا است. در این روش، در هنگام گذر، مقدار اندکی از نور ستاره از میان جوّ سیاره عبور می‌کند و در برخی طول موج‌ها با توجه به ترکیبات شیمیایی موجود در جو، جذب می‌شود. در نتیجه، نور عبور کرده از جو، شامل اطلاعات مفیدی از سیاره است. یکی از مشکلات اصلی این نوع مطالعات، جداسازی سیگنال سیاره از سیگنال ستاره مادر است. انتظار می‌رود با توجه به اندازهٔ بالای سطح مقطع جذبی سدیم، سیگنال عبوری این عنصر نسبتاً بزرگ بشود که بنابراین برای این‌گونه مطالعات مناسب است. هدف این پایان‌نامه، ارائهٔ یک چارچوب بهینه برای طیف‌بینی عبوری با توان تفکیک بالا در نوارهای باریک طول موج در طیف سدیمِ اتمی است.

رصدهای گذر دو داغ‌برجیس (hot-Jupiter) متورم برای فراکافت و بررسی انتخاب شده‌اند: نخست HD 189733b، که به دور یک ستارهٔ فعالِ نوع K می‌گردد و با بهره‌گیری از «طیف‌نگار اشل فرابنفش و مرئی» (UVES) که بر روی «تلسکوپ بسیار بزرگ» (VLT) نصب شده، رصد شده‌است. دوم WASP-17b، که به دور ستارهٔ نوع F می‌گردد، با «طیف‌نگار اشل ماژلان ایناموری کیوسرا» (MIKE) که بر روی «تلسکوپ‌های ماژلان» نصب شده رصد شده‌است.

در این کار، من منحنی‌های نوری جوی را در نوارهای باریک حدود ۱ تا ۳ آنگستروم در مرکز هر خط سدیم محاسبه می‌کنم. برای استخراج سیگنال جذبی فراسیاره از این منحنی‌های نوری خام، ابتدا اثرات بازدارندهٔ فعالیت شراره‌ای ستاره مادر را با استفاده از بررسی خط هیدروژن آلفا (Hα) و خطوط سه‌گانهٔ مادون قرمز کلسیم (Ca II IRT) و Ca II H & K ، مدل‌سازی می‌کنم. علاوه بر این، اثر تاریکی لبهٔ ستاره را نیز در نظر می‌گیرم. در نهایت، به عنوان جزء جدیدِ این مدل‌سازیِ منحنیِ نوری، سرعت شعاعیِ سیاره را برای توضیح برآمدگیِ معمول در مرکزِ منحنیِ نوری به کار می‌برم. این امر منجر به تعیین شکل سدیم جوّی فراسیّاره می‌شود. با استفاده از این رویکرد، علی‌رغم فعالیت ستاره‌ای شدید، سدیم را در سیارهٔ HD 189733b آشکارسازی می‌کنم. از آن سو، ستارهٔ میزبان در سیستم WASP-17 فعالیت شراره ای شدیدی نشان نمی‌دهد؛ بنابراین، علاوه بر اِعمالِ روشِ منحنی نوری، طیف عبوری WASP-17b در منطقهٔ خطوط سدیم را نیز بدست می‌آورم. سپس طیف مشاهده شده با یک مدل اتمسفر سیاره‌ای ساده مقایسه می‌شود که منجر به بازیابی پارامترهای جوی مانند دما و شعاع در ۰/۱ بار می‌گردد.

این پایان‌نامه نشان می‌دهد که آشکارسازی سدیم یک روش تشخیص خواص فیزیکی جو فراسیاره‌ها است و بیان می‌دارد که اگر تغییرات در سرعت شعاعی در نظر گرفته شود، تخمین شکل خطوط طیفی سیاره بدون نیاز به به دست آوردن طیف عبوری ممکن می‌شود. روشی که در این پایان‌نامه توسعه یافته‌است، قابل اعمال سریع بر روی دیگر فراسیاره‌ها نیز است.

Preface

This thesis contains four chapters. The first chapter is the general introduction to the exoplanet detection and atmospheric characterization, which conveys the motivation and the required background of the research.

The second chapter presents the high-resolution transmission spectroscopy of the hot-Jupiter HD 189733b, to detect and characterize the atomic composition of the atmosphere of this exoplanet. The majority of this chapter is published in the Astronomy and Astrophysics Journal, as the article *'Exoplanetary atmospheric sodium revealed by orbital motion, Narrow-band transmission spectroscopy of HD 189733b with UVES'* (Khalafinejad et al., 2017). The chapter additionally includes a supplementary section (last section). The co-authors of the publication are C. von Essen, H. J. Hoeijmakers, G. Zhou, T. Klocová, J.H.M.M. Schmitt, S. Dreizler, M. Lopez-Morales, T.-O. Husser, T.O.B. Schmidt, R. Collet. All the text is written by me, with some modifications made by the co-authors of the paper. All the analysis are done by me, except the calculation of the differential limb-darkening coefficient which is based on a code developed by Carolina von Essen using PHOENIX angle resolved spectra (see Section 2.3.2.2). Any difference compared to the published manuscript is written inside square brackets.

The third chapter focuses on probing the atmosphere of the hot-Jupiter WASP-17b using the spectral features of the atomic sodium. The whole chapter, except the supplementary materials (last section), is recently submitted to Astronomy and Astrophysics Journal as the article, *'The atmosphere of WASP-17b: Optical high-resolution transmission spectroscopy'*, which will be accepted after revision. The co-authors of the article are M. Salz, P. Cubillos, G. Zhou, C. von Essen, T.-O. Husser, D. D. R. Bayliss, M. Lopez-Morales, S. Dreizler and J. H. M. M Schmitt. The majority of the text is written by me. Michael Salz has contributed to a part of Section 3.3.1, and Patricio Cubillos has presented Section 3.7.3.1. Other co-authors have contributed with scientific discussion and minor modifications of the text. All the analysis is performed by me except the major part of the analysis of H_α and Ca II infrared triplet, which is done by Micheal Salz. The development of the theoretical atmospheric model and retrieval of the atmospheric parameters was performed by Patricio Cubillos. In this chapter also differences with respect to the submitted manuscript are indicated inside square brackets.

The fourth chapter firstly presents a summary of the thesis as well as the lessons I learned from my work along my PhD. In the second part of this chapter, a future outlook regarding the field of exoplanetary detection and characterization is given.

Contents

For my parents

تقدیم به پدر و مادرم

Chapter 1

Introduction

Our curiosity about ourselves, our planet and the universe that we live in has prompted us to look for an answer to the question: Are there Earth-like and habitable planets elsewhere in the universe? It is an old question of mankind, but in the current time, with the enormous advances in science and technology, we are very close to find the answer. Extrasolar planets, in short exoplanets, are planets that orbit stars other than our Sun. Until recently, our knowledge about the planets and planetary systems was limited to the Solar System and our instrumental limitations did not allow us to look any further. But finally in 1990s, the existence of the first exoplanets was confirmed (Wolszczan & Frail, 1992; Mayor & Queloz, 1995) and since then, mainly thanks to several dedicated exoplanet searches, such as Kepler (Borucki et al., 2003; Basri et al., 2005), CoRoT[1] (Catala et al., 1995), HATNet[2] (Hartman et al., 2004a), WASP[3] (Kane et al., 2003; Pollacco, 2005), and HARPS[4] (Pepe et al., 2000), a few thousand exoplanets (Schneider, 2011) have been discovered and this number is rapidly increasing.

Exoplanets are very diverse, showing a wide variety of physical and orbital parameters that can be completely different from our Solar System planets. For instance, we have discovered many Jupiter-mass exoplanets that are orbiting their host stars in distances of a fraction of Mercury's distance from the Sun (see the upper left population in Figure 1.1). These so-called "hot-Jupiters" have had important impacts on planetary migration scenarios since their discovery (Lin et al., 1996). Other interesting exoplanet populations are so-called super-Earth and sub-Neptune planets with radii between 1-3 $R_{\oplus}$[5] that are the most commonly found planets from the Kepler telescope (e.g., Fressin et al., 2013), but do not exist in our Solar System. More recent statistical studies of exoplanets have shown that the radius distribution of exoplanets is bimodal. The majority

[1] COnvection ROtation and planetary Transits
[2] Hungarian-made Automated Telescope Network
[3] Wide Angle Search for Planets
[4] High Accuracy Radial velocity Planet Searcher
[5] $R_{\oplus}$ is the radius of Earth

of exoplanets are super-Earths and sub-Neptunes, having radii of about 1.3 and 2.4 $R_\oplus$ respectively. There is a gap in the number of exoplanets from ∼1.5 to 2.0 $R_\oplus$ (Fulton et al., 2017). The origin of this gap is a subject of debate and one of the more likely explanations is photoevaporation. In this scenario a small difference in the atmospheric hydrogen/helium envelope can cause the planet to turn into a rocky planet or to stay a gaseous planet, leaving a valley in between (Fulton et al., 2017; Owen & Wu, 2017). Due to observational biases, the detection and characterization of giant planets used to be the most common, but the focus today is shifting towards finding and characterizing smaller rocky planets, driven by exciting advances in our current and future instrumental capabilities (see Chapter 4). Recent discoveries of some rocky, terrestrial exoplanets (e.g., Berta-Thompson et al., 2015; Anglada-Escudé et al., 2016; Gillon et al., 2017), have brought us closest to finding a true Earth analogue.

Typically, through the exoplanetary detection, orbital and dynamical properties of these systems can be measured. However, to investigate their physical and chemical properties, an in-depth characterization of the their atmosphere is required. Exoplanetray atmospheric characterization is essential to understand the origin of planets and their formation environment, clouds, climate, and atmospheric dynamics. Ultimately it is important to detect and interpret possible biosignatures and study the unique environment for the emergence of life (Seager, 2014).

In this chapter, I first briefly review the exoplanetary detection techniques, then I report on the current status and different techniques of exoplanetary atmospheric studies. I also introduce the effects that impede the exo-atmospheric[6] detection and finally, I introduce the aims of this thesis.

1.1 Detection of exoplanets

There are a handful of different techniques for the detection of exoplanets. An overview of confirmed exoplanets is shown in the mass vs. semi-major axis diagram in Figure 1.1: the vast majority of exoplanets have been discovered by transit and radial velocity techniques, which contain a wealth of information on dynamical and physical characteristics of these planets. Particularly the transit technique is biased towards massive and close-in (semi-major axis < 1 AU) exoplanets. Most of the hot and large exoplanets with large semi-major axes have been discovered through direct imaging. These exoplanets are found at the upper right tail of the plot. In addition, a small fraction of exoplanets has been detected through transit timing variation (TTV), pulsar timing variations, gravitational microlensing, and astrometry. In all of the detection techniques, except direct imaging, the planet cannot be directly observed, however its footprints can be found in

[6]The term "exo-atmosphere" is a short form for the "exoplenatary atmosphere".

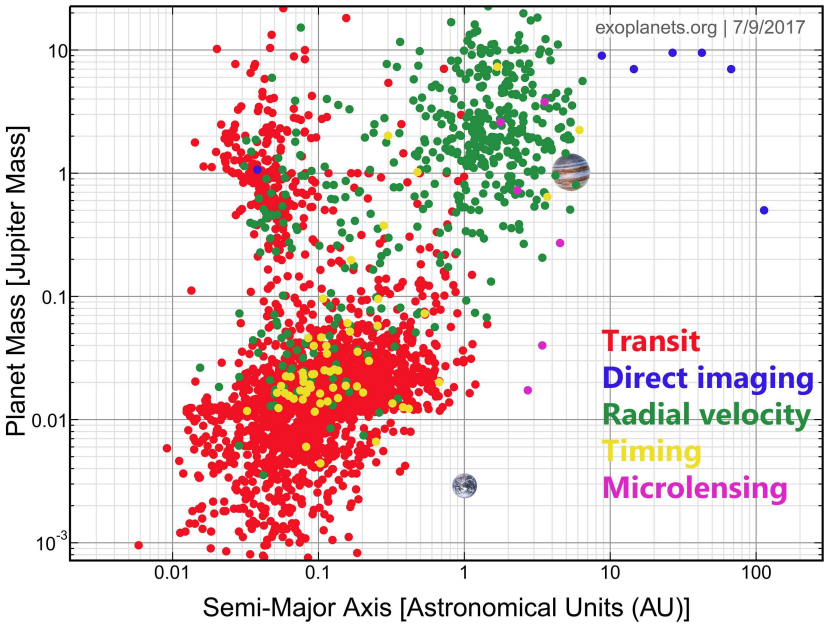

FIGURE 1.1: Known exoplanets detected and confirmed as of July 2017. The color of each data point represent the original detection method. The majority of exoplanets are discovered by transit (red) and radial velocity (green) techniques. Some are discovered through timing variations (yellow), which consists of both pulsar timing and transit timing and a hand full of them through direct imaging (blue) and microlensing (pink) methods. Exoplanets with other detection techniques are ignored in this plot. Solar System planets are also shown as reference points (extracted from http://exoplanets.org/).

changes of the behaviour of the host star; i.e., changes of radial velocity, position, or flux of the star. In the following subsections these techniques are further explained.

1.1.1 Radial velocity technique

The radial velocity technique led to the first exoplanet discovery around a main sequence star in 1995 (Mayor & Queloz, 1995). Due to mutual gravitational interactions between the star and the planet, the host star shows a wobbling motion. The radial velocity technique detects this wobbling motion through the periodic Doppler shift of stellar spectral lines. The observed wavelength shift ($\Delta\lambda$) and the radial velocity variations (v) at each time (t) and wavelength (λ) are related to each other by, $\frac{\Delta\lambda(t)}{\lambda} = \frac{v(t)}{c}$, where c is the speed of light. Measuring temporal changes of the stellar radial velocity, results in a radial velocity curve (see two samples in Figure 1.2), which contains information on the physical parameters of the system. For instance, the repetition of the pattern of the curve reveals the orbital period (P) of the planet and the tilt of the curve telltales the orbital eccentricity (e). In addition, the lower limit on the mass of the planet ($M_{\rm P} \sin i$, where i is the inclination of the orbit) can be determined. The following equation express the relation of these parameters with each other:

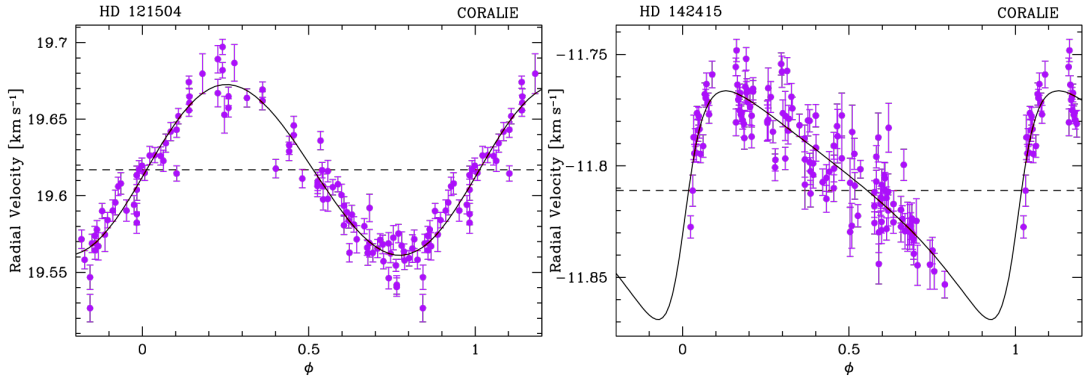

FIGURE 1.2: Phase-folded radial velocity curves of the systems, HD 121504 and HD 142415, observed through CORALIE survey (Mayor et al., 2004). **Left:** The modeling of the radial velocity curve of HD 121504 reveals an eccentricity of 0.03 (close to a circular orbit) for the exoplanet. **Right:** The modeling of the radial velocity curve of HD 142415 shows that the exoplanetary orbit is elliptical with an eccentricity of 0.5 (taken from Mayor et al., 2004).

$$K = \left(\frac{2\pi G}{P}\right)^{\frac{1}{3}} \frac{M_{\rm P} \sin i}{(M_* + M_{\rm P})^{2/3}} \frac{1}{\sqrt{1-e^2}} \tag{1.1}$$

where K is the radial velocity curve semi-amplitude, G is the gravitational constant and M_* and M_P are the stellar and planetary mass respectively.

As the first detection technique, radial velocity has been around several years before the transit method. Combination of this with the long-term availability and stability of radial velocity measurements, has resulted in numerous planet detections beyond 1 AU with orbital periods much larger than one year. One of the main obstacles in detection of smaller exoplanets is the stellar activity such as spots and plages that cause modulations in the radial velocity curve on the same level as these exoplanets (e.g., Dumusque et al., 2011). Nevertheless, using ground-based high-resolution and stable spectroscopic instruments such as HARPS, some of the nearest terrestrial exoplanets, such as Alpha Centauri b and Proxima Centauri b have been discovered (Dumusque et al., 2012; Motalebi et al., 2015; Anglada-Escudé et al., 2016) through radial velocity measurements. In addition to the detection, the radial velocity technique is extensively used for follow up observations and mass determination of exoplanetary candidates found by the transit method (e.g., Pont et al., 2005; Bouchy et al., 2009; Mayor et al., 2014).

1.1.2 Transit and transit timing variation

When a planet passes in front of its parent star from our vantage point, it slightly dims the flux we receive from the star (see Figure 1.3). Thus, it creates a dip in the light curve of the system. Larger planets block more light and therefore create deeper dips. The fractional dimming of the stellar flux is equal to the ratio of the area of the projected disk of the planet and the star as shown in Equation 1.2.

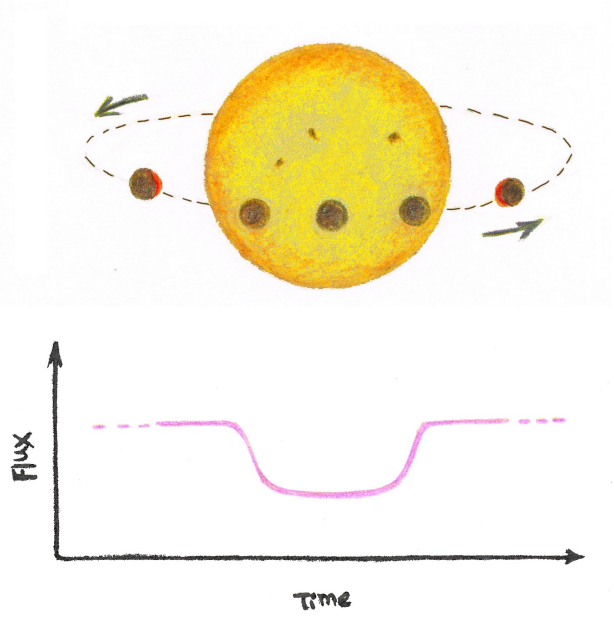

FIGURE 1.3: The exoplanetary transit and the transit light curve (time axis is not in scale). When the planet transits it blocks a part of the light that comes from the star.

$$\frac{\Delta F}{F} = \left(\frac{R_{\rm P}}{R_*}\right)^2 \tag{1.2}$$

In this equation, F is the total stellar flux and ΔF is the amount of change in F during the transit. $R_{\rm P}$ and R_* represent the planetary radius and stellar radius, respectively. In addition, the transit duration contains further information about the system geometry as seen by the following relation (Haswell, 2010),

$$T_{dur} = \frac{P}{\pi} \sin^{-1}\left(\frac{\sqrt{(R_* + R_{\rm P})^2 - a^2\cos^2 i}}{a}\right) \tag{1.3}$$

where a is the semi-major axis of the orbit.

Transits occur only when the inclination of the orbit is close to 90 degrees. The geometric probability of occurrence of a transit is $\frac{R_*}{a}$. Therefore, transits are not very likely to happen: In the Solar System, this probability is about 10% for a hot-Jupiter and only about 0.5% for an Earth analogue. Nevertheless, currently this method is the most successful in detection of exoplanets. Large transit surveys such as Kepler space mission and WASP ground-based telescopes have greatly contributed to the discovery of exoplanets. Precise light curves obtained through Kepler observations have been a key for the detection of Earth-size exoplanets.

These small exoplanets have been found both through transit light curves directly (e.g., Quintana et al., 2014) or through the perturbations that they cause in the transit times of giant exoplanets in multiple systems. The later method is known as transit timing variation (TTV) and has been used to detect several non-transiting small exoplanets

in exoplanetary systems with at least one transiting exoplanet (e.g., Holman & Murray, 2005; Carter et al., 2012). In addition, the TTV method can be used to determine the masses and upper limits on eccentricities of transiting planetary systems (e.g., Gillon et al., 2017), independent from the radial velocity follow-up.

Transits provide a great opportunity for orbital and dynamical characterization of exoplanetary systems. The measurement of the planetary size (planet to star radius ratio), period, inclination, spin-orbit misalignment of the system and star-planet obliquity are some of the observational rewards that can be obtained through transits (e.g., Seager & Mallén-Ornelas, 2003; Sackett, 1999). In addition, a transit offers the opportunity for characterization of the planetary atmosphere (see Section 1.2). Moreover, combining the mass measurement obtained from radial velocity (or TTV) with the radius obtained through the transit method, results in the determination of the mean planetary density, which provides clues about the bulk composition of exoplanets (e.g., Motalebi et al., 2015; Zeng et al., 2016).

1.1.3 Direct imaging technique

The most natural idea that comes to the mind for detecting exoplanets is to take their images. However, imaging exoplanets is very challenging due to the very high contrast between the brightness of the star and the planet and the close angular proximity of the planet to the host star. For a Jupiter-like exoplanet around a Sun-like star, the brightness contrast between the planet and the star is about $\sim 10^{-9}$ in the optical region of the spectrum and $\sim 10^{-8}$ in the infra-red region (Traub & Oppenheimer, 2010) and for younger exoplanets the brightness contrast in IR reaches $\sim 10^{-5}$ - 10^{-6}. Hence, very high spatial resolution and high contrast imaging methods are needed even for the detection of nearby, young, hot, and large exoplanets that are in the late stages of planet formation.

Despite these difficulties, using high contrast imaging techniques, we can discover and characterize such systems. Methods such as, polarimetric differential imaging (PDI,Quanz et al. 2011), stellar Point Spread Function (PSF) subtraction (e.g., Lagrange et al., 2009) or coronagraphy (e.g., Currie et al., 2012) in combination with precise adaptive optics (AO) can be used to remove the star from the image and detect the hot, young exoplanets at large angular separations from heir host stars. A sample of a directly imaged system is shown in Figure 1.4.

The first direct imaging exoplanet was a planetary-mass object around a brown dwarf detected in 2004 (Chauvin et al., 2004). There are still only a hand-full of exoplanets discovered with this technique, however, great improvements are expected in the near future using the Mid-infrared ELT[7] Imager and Spectrograph (METIS, e.g., Quanz et al., 2015).

[7]Extremely Large Telescope

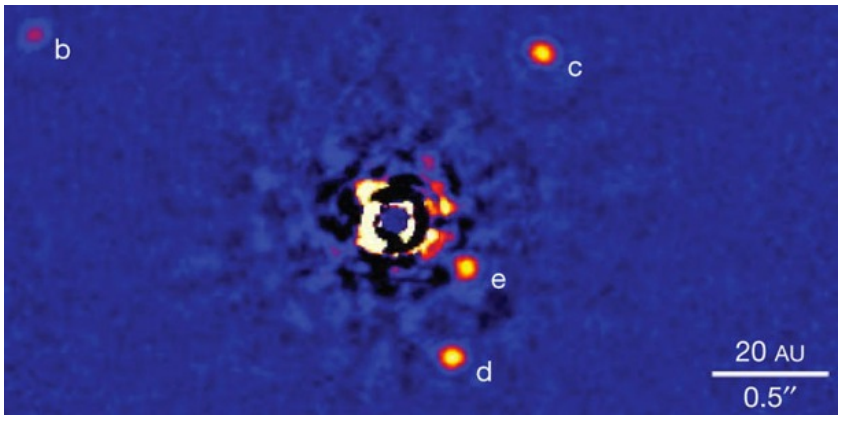

FIGURE 1.4: The direct image of the system HR 8799. After subtraction of the stellar PSF, four exoplanets have been discovered and they are shown in letters b to e. (Marois et al., 2010)

1.1.4 Other techniques

In this subsection, I briefly introduce some of the other techniques used to detect exoplanets.

Microlensing: This method is based on the gravitational lensing phenomenon, in which a massive object bends the light coming from a background object like an optical lens would do. As a result, the light of the background object is distorted and magnified and its apparent brightness is increased during the lensing event. The lens object can be a star with a planet and when the planet lines up with the star from our line of sight the lens power (and the magnification) is increased. This causes a short blip in the brightness of the background source which is known as microlensing event (see Figure 1.5). Microlensing can be used for the detection of small exoplanets at large orbital distances. Through microlensing, the planet-star mass ratio and their projected separation can be estimated, however, no orbital parameter can be obtained. Moreover, no follow-up observations are possible for such systems, since the phenomena cannot be re-examined, and these systems are normally too far away for other detection methods. These exoplanets are often used for statistical analysis, because they are not biased to massive close-in planets (e.g., Gould et al., 2014; Yee et al., 2014).

Astrometry: The wobbling motion, which is caused by the star-planet gravitational interaction, may be observed through precise tracking of the position of the star. When the planet is massive and far out from the star, the center of mass is further from the star and thus the amplitude of the reflex motion of the star becomes larger. Currently, there are only two exoplanets detected with this technique (Muterspaugh et al., 2010; Sahlmann et al., 2014). The required precision is about 10 μas and the Gaia space mission (Bienayme & Turon, 2002; Gaia Collaboration et al., 2016) is well capable of

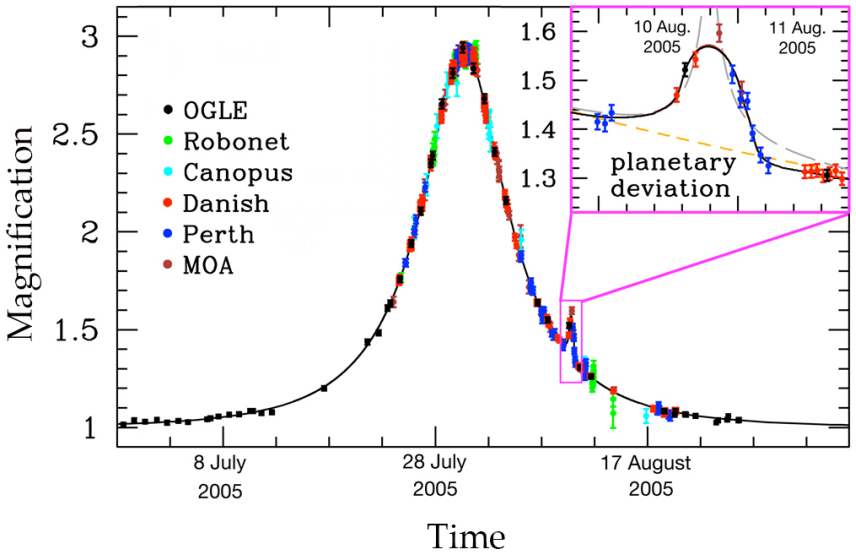

FIGURE 1.5: The discovery of an exoplanet of 5.5 Earth-masses through the microlensing method. The main increase of the flux is due to the magnification of the background source by the host star, which lasts in the order of a month. The blip in the right wing of the curve is due to the extra magnification by the exoplanet, which takes less than a day (Adopted from Beaulieu et al., 2006).

achieving such a precision. Gaia was launched at the end of 2013; the nominal length mission ends after 5 years and the extended length mission after 10 years. By the end of these missions, thousands of new exoplanets are expected to be found (Perryman et al., 2014; Ranalli et al., 2017).

Pulsar timing: The first exoplanet was detected in 1992 using the pulsar timing technique (Wolszczan & Frail, 1992)[8]. The rotation of a pulsar is highly regular, thus, slight anomalies in the timing of its observed radio pulses can be the signature of a perturbing body such as a planet. A few dozen exoplanets have been detected by this technique. These planets are interesting to be studied, because, they have either survived the catastrophic formation history of the neutron star or they formed as a secondary planet population in a disk surrounding the neutron star.

Eclipse timing variation: Variations in the timing of the eclipse in close binary stars can be caused by a circumbinary planet that induces gravitational perturbations. This method is known as eclipse timing variation (ETV) and can be used to determine the mass and the orbital parameters of the perturbing body, which is very similar to the TTV method. The idea of finding an exoplanet with this technique has been around since the 1990s (Schneider & Chevreton, 1990), and was later developed and used in

[8]later in 1995 the first exoplanet around the main sequence star, 51 Pegasi, was detected (Mayor & Queloz, 1995), which in some texts is also known as the first exoplanetary detection.

many studies (e.g., Schwarz et al., 2011; Borkovits et al., 2015).

Full-phase photometric variation: Similar to the inferior planets in the Solar System, exoplanets (except those with face-on orbit) show different planetary phases during revolution around their host star. As a result the flux of the system periodically changes by the planetary orbital phase. Long-term and precise photometic monitoring of the stars can result in detection of exoplanets around them. Attempts for using this method has been started for some time (e.g., Faigler & Mazeh, 2011; Placek et al., 2014; Shporer & Hu, 2015) and recently Millholland & Laughlin (2017) have developed an algorithm for extraction of non-transiting exoplanetary candidates from the treasury of Kepler data. This method has also been used for the atmospheric characterization of exoplanets (see Section 1.2.2 and 1.2.3).

1.2 Atmospheric characterization of exoplanets

It has been nearly two decades since we have reached required tools and techniques to investigate exoplanetary atmospheres. So far, a large number of these studies has been made through spectroscopic observations of exoplanets during transits. The study of orbit induced variations in the emitted and reflected light of exoplanets and direct imaging are other atmospheric characterization techniques that can be applied on both transiting and non-transiting exoplanets. Different techniques can be complementary to each other, because different wavelengths probe different layers of exoplanetary atmospheres. Understanding the atomic and molecular composition, estimation of the average temperature and temperature-pressure profile, and parameters such as albedo are currently among the main topics of interest in the observational study of exoplanetray atmospheres. Although the principles of atmospheric studies is the same in both terrestrial and giant planets, so far observational limitations have only allowed the characterization of giant gaseous exoplanets. However, this limitation will face a revolution by the commence of the upcoming missions such as transiting exoplanet survey satellite (TESS, Ricker et al., 2015), James Webb space telescope (JWST, Gardner et al., 2006), and characterising Exoplanet satellite (CHEOPS, Broeg et al., 2013), which are expected to detect and characterize small exoplanets as well as the giant ones (See Chapter 4).

Transiting exoplanets provide the opportunity for atmospheric characterization in three cases: During the primary and secondary transits and via phase curve variations (see Figure 1.6) or radial velocity variations (see Section 1.2.3). This thesis focuses on transmission spectroscopy during the primary transit. Thus, in the following I mainly explain transmission spectroscopy and only briefly introduce the other methods.

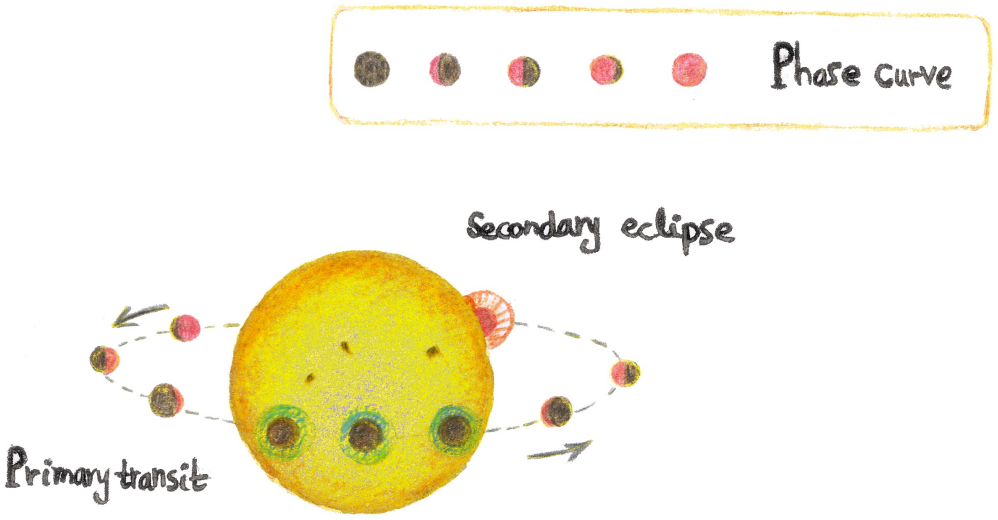

FIGURE 1.6: Atmospheric characterization in transiting systems. The exoplanet can be characterized in three cases: During the primary and secondary transits, as well as via phase or radial velocity variations over the orbit.

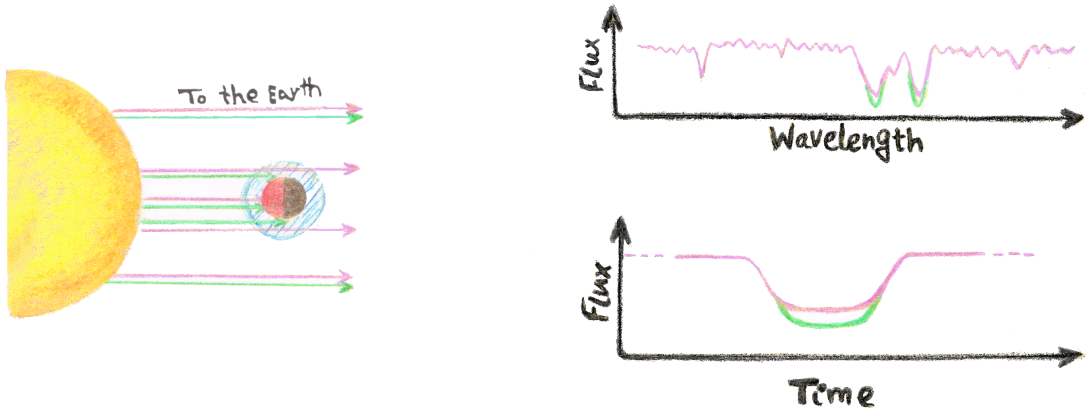

FIGURE 1.7: Transmission Spectroscopy. A schematic illustration of transmission spectroscopy: The green color represents the stellar light that is absorbed by the exoplanetary atmosphere. As a result the corresponding spectral lines show an additional absorption and the transit light curve shows an additional dimming at this wavelength (green) compared to neighboring wavelength bands (magenta).

1.2.1 Transmission spectroscopy

1.2.1.1 Principles

During primary transit a small fraction of the stellar light passes through the exoplanetary atmosphere; depending on the atmospheric constituents, at a certain wavelength, the light may be absorbed or scattered. As shown in Figure 1.7, the additional absorption of the stellar light at the wavelength specific of the exoplanetary composition results in a light curve with larger depth compared to the neighboring pass bands. This also demonstrates that the opacity of the atmosphere and the radius of the exoplanet are wavelength-dependent. We can therefore obtain the transmission spectrum of an exoplanetary atmosphere by multi-wavelength measurements of the depth of the transit light curve. In primary transits we are facing the night-side of the exoplanet and the optical transmission spectra originate from the planetary day-night terminator. The excess absorption depth, as shown in equation 1.4, is proportional to the ratio of the area of the atmospheric annulus divided by the area of the star.

$$\frac{\delta F_{\rm excess}}{F} = \frac{(R_{\rm P} + nH)^2 - R_{\rm P}}{R_{\rm s}^2} \simeq \frac{2R_{\rm P}(nH)}{R_*^2}, \tag{1.4}$$

In this equation, $\delta F_{\rm excess}$ is the additional absorption of the flux by the exoplanet's atmosphere. nH is the thickness of the atmospheric annulus, which is several times ($n \sim$ 5-10) the atmospheric scale height (H). By definition the scale height is the vertical distance over which the pressure of the atmosphere changes by a factor of Euler's number e (~ 2.72). Assuming hydrostatic equilibrium and the ideal gas law, the scale height is estimated by the following equation,

$$H = \frac{kT}{\mu g} \tag{1.5}$$

where k is Boltzmann's constant, T is the atmospheric temperature, μ is the mean molecular weight of the atmosphere, and g is the surface gravity of the planet. The scale height of a hot-Jupiter is on the order of 100 km and for an Earth-like planet it is about 10 km. Thus the expected variations of the stellar flux for a Jupiter-like planet is up to about 0.1% and for an Earth-like planet is up to 0.01% relative to the stellar continuum. This explains the rarity of atmospheric characterizations of terrestrial exoplanets compared to hot-Jupiters up to now.

1.2.1.2 General applications

Transit spectroscopy leads to a wealth of information about the ongoing chemical and physical processes on exoplanets. In principle, the identification of the chemical composition of the atmosphere (e.g., Burrows, 2014; Fischer et al., 2016; Bento et al., 2014;

Deming et al., 2013; Désert et al., 2008) and the study of the clouds/hazes (e.g., Gibson et al., 2013; Kreidberg et al., 2014; Pont et al., 2013) are the first main goals in transmission spectroscopy. These observations put constraints on exoplanetary atmospheric models and will eventually result in unveiling the physical properties of the atmosphere e.g., temperature-pressure profile, average temperature (e.g., Huitson et al., 2012) and estimation of number densities of species (e.g., Brogi et al., 2016; Heng et al., 2015). Even obtaining information on atmospheric winds (e.g., Louden & Wheatley, 2015) and the evaporation of atmospheres (e.g., Vidal-Madjar et al., 2003; Bourrier et al., 2016) are possible through transmission spectroscopy.

In the optical region the atomic doublet lines of sodium and resonance lines of potassium have larger absorption cross sections. At a typical temperature of a hot-Jupiter ($\sim$ 1000 K) these species are predicted to show strong absorption features in the transmitted light (Seager & Sasselov, 2000; Fortney et al., 2010). Besides individual species, the presence of atmospheric haze can be investigated in the blue part of the optical wavelengths and clouds can be studied throughout the optical red and IR part of the transmission spectrum. In addition, in the visible wavelength range, using very high-resolution and stabilized spectrographs, we are able to search for molecular features of metal oxides and hydrates such as TiO, MgH in hot gaseous exoplanets (e.g., Sedaghati et al., 2017; Hoeijmakers et al., 2015) and in the future O_2 in rocky exoplanets (e.g., Rodler & López-Morales, 2014). The successful detection of an exoplanetary atmosphere using transmission spectroscopy was pioneered by Charbonneau et al. (2002), who detected sodium in the atmosphere of the hot-Jupiter HD 209458b using Hubble Space Telescope (HST). As of now, species such as hydrogen, carbon, oxygen, sodium, and potassium have been detected in the UV-optical region in hot-Jupiters (e.g., Vidal-Madjar et al., 2003, 2004; Sing et al., 2011; Huitson et al., 2012). In some cases we have seen featureless spectra that can be the signature of cloud decks (e.g., Gibson et al., 2013; Kreidberg et al., 2014; Nortmann et al., 2016). The scattering slope in the optical-blue part of the spectrum, has been interpreted as the footprint of atmospheric hazes in hot-Jupiters atmospheres (e.g., Sing et al., 2013; Pont et al., 2013). In addition in the IR region, signatures of molecules such as CO, CO_2 H_2O have been detected through transmission spectra (e.g., Tinetti et al., 2010; Sing et al., 2016).

1.2.1.3 Instruments and techniques

Two types of spectral instruments can be used for transmission spectroscopy: Based on the subject of study, broad- and narrow-band transmission spectroscopy can be applied using low- and high-resolution instruments respectively. These two approaches provide complementary information in understanding of the exoplanetary atmospheres.

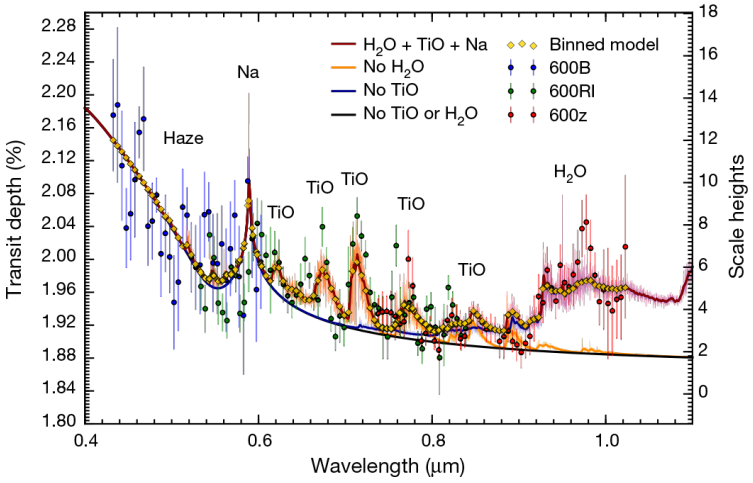

FIGURE 1.8: Transmission Spectrum of WASP-19b. The plot shows the transit depth (which is proportional to the square of the planetary radius) at different wavelengths. Solid lines with different colors show atmospheric models with different compositions. The scattering slope that indicates the existence of haze, and the absorption signal of sodium can be seen in the blue-ward part of the optical spectrum. Molecular absorption of TiO and H_2O are visible in the green and red part of the spectrum receptively (taken from Sedaghati et al., 2017).

Low-resolution technique: Low-resolution ($\mathcal{R} \sim 1000$) spectrographs are used to obtain the broad-band transmission spectra. During the transit observation, spectra from the host star as well as at least one reference star in the field are captured to apply spectro-photometry in wavelength bins of usually $\sim$ 50 Å. Measurement of the depth of the transit light curve in each wavelength bin results in a low-resolution transmission spectrum of the exoplanet. Broad-band exoplananetary spectra allow us to infer whether clouds or hazes are present in the atmosphere of the observed planet. The information regarding the haze can be inferred from the shape of the scattering slope in the blue part of the optical spectrum (see Figure 1.8) and clouds are one possible explanation for observing a featureless spectrum towards the red wavelengths. The presence of high-altitude cloud/haze layers partially (or completely) obscures the atomic/molecular features. In clear atmospheres low-resolution, broad-band transmission spectra allow the detection of atoms and molecules (e.g., Na, K, TiO, H_2O; e.g., Pont et al. 2013; Sedaghati et al. 2016; Sing et al. 2016; Sedaghati et al. 2017). So far, hot-Jupiter transmission spectra have revealed a diversity of planetary atmospheres (Sing et al., 2016). As an example, the spectrum of the inflated hot-Jupiter WASP-19b is shown in Figure 1.8. This figure shows sodium, titanium oxide, and water absorption by comparison with an atmospheric model spectrum. Other important outcomes of broad-band techniques are the determination of the average atmospheric temperature (e.g., Huitson et al., 2012), vertical temperature structure of lower atmosphere (e.g., Vidal-Madjar et al., 2011), and the deduction of the shape of the continuum of the exoplanetry spectrum.

High-resolution technique: High-resolution spectra can be used in two cases:

Narrow-band technique: At resolution of about 20,000 or higher, if the spectral lines are deep and broad, one can select a narrow integration passband ($\sim$ 1 Å) inside the core of the lines, e.g. atomic lines of Na and K, and measure the excess absorption (e.g., Jensen et al., 2011). This technique is the main focus of this thesis and is extensively explained in chapters 2 and 3. The comparison of the observational measurements with the exoplanetary atmospheric models allows to constrain the characteristics of the atmosphere such as the number densities of these species and the temperature-altitude profile (e.g., Wyttenbach et al., 2015). Even in the case of an obscured atmospheres with hazes and low-level clouds, high-resolution observations allow to infer information on the atmospheric constituents with the narrow-band analysis (Kempton et al., 2014; Morley et al., 2015). To constrain the vertical temperature structure of the upper atmosphere, the absorption depths in the core (regions with lower density) of the high-resolution planetary spectral lines are needed. Such information is a complementary to the low-resolution data that determines the absorption depths far in the wings (regions with higher density) and unveils the lower altitudes. Last but not least, the narrow-band technique has also been used at hydrogen Balmer alpha line (H_α) to investigate the bow shocks that transit prior to the exoplanet (Cauley et al., 2015).

High dispersion technique: Due to the orbital motion of the exoplanet its radial velocity varies (unless the orbital inclination is zero). Hence, the spectral features induced in the exoplanet's atmosphere are Doppler shifted with respect to the stellar spectral lines. At very high spectral dispersion ($\mathcal{R} \sim$ 100,000) most of the stellar and planetary absorption lines are individually resolved. The Doppler shift of planetary atmospheric features, which is often about $\pm$20 kms^{-1} during a planetary transit, can be used to discern them from the dominating stellar spectrum in which they are embedded. With the numerous narrow absorption lines of molecules, transmission spectra can be cross-correlated with a template spectrum to co-add the effect of all individual lines (e.g., using the ExoMol molecular line list, Tennyson et al. 2016). Molecular lines are mostly formed in the IR range, but if the transiting planet is hot enough (T $\geq\sim$ 2000 K), one can also detect transmitted signatures of metal oxides and hydrates in the visible region of the spectrum even at trace abundances (Hoeijmakers et al., 2015). This method is applicable not only to the transmitted but also to emitted and reflected light. Hence it can also be used for the case of non-transiting exoplanets (see Section 1.2.3).

1.2.2 Secondary eclipse and phase curve

After primary transit, the planet continues to traverse its orbit. When it reaches the superior conjunction, the planet becomes occulted by the star and a secondary eclipse

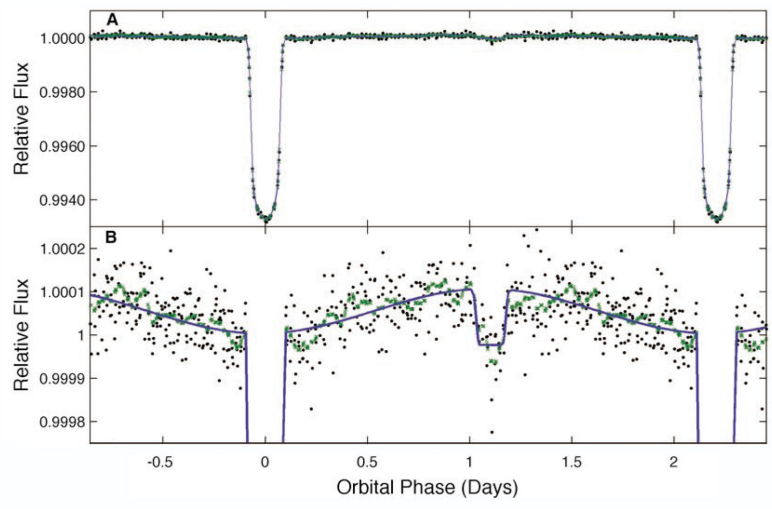

FIGURE 1.9: Full-phase Kepler transit light curve of HAT-P-7b, including the primary transit, secondary eclipse and the phase curve. **Panel A** is the light curve with the full depth and **panel** B is the light curve expanded to see the secondary and the phase curve (Adopted from Borucki et al. 2009)

occurs. The secondary eclipse configuration is illustrated in Figure 1.6 and as an example a full transit light curve of HAT-P-7b, including the secondary eclipse, is shown in 1.9. Similar to transmission spectroscopy, the secondary transit light curve depth varies at different wavelengths. Hence, emission spectra from the full day-side of the planet can be constructed using the wavelength dependence of the emission signals, which depend on the planetary compositions (e.g., Deming et al., 2005; Pont et al., 2012; Kreidberg et al., 2015; Bean et al., 2013; Brogi et al., 2016). In contrast to the primary transit, with which we can study the planetary terminators, in secondary eclipse we are able to investigate the entire day-side properties of exoplanetary atmosphere. The information from the atmosphere of the exoplanet in this orientation comes from thermal emission (in near-IR to mid-IR) and reflection (in optical and near-UV).

Assuming the planet to be a black body emitter, in the IR wavelength region the depth of the occultation light curve (ΔF_{occ}) is approximated as,

$$\frac{\Delta F_{\rm occ}(\lambda)}{F(\lambda)} \approx \left(\frac{R_{\rm p}}{R_*}\right)^2 \frac{\beta_\lambda(T_{\rm eq})}{\beta_{\lambda(T_{\rm eff})}} \tag{1.6}$$

where $\beta_\lambda(T)$ is black body flux, T_{eff} is stellar effective temperature, and T_{eq} is the planetary equilibrium temperature,

$$T_{\rm eq} = T_{\rm eff}(\frac{R_*}{a})^2(f(1-A))^4. \tag{1.7}$$

In this equation, a is the semi-major axis, A is the bond albedo and f is the heat redistribution factor which is equal to $\frac{1}{4}$ for an isotropic model, where the heat is efficiently redistributed over the day and night-side of the exoplanet.

While the planet is moving between primary to secondary eclipses, from our vantage point, the exoplanetary flux varies with the orbital phase (see Figure 1.6). This variation, known as phase curve, is shown in panel B of Figure 1.9. Since in the IR wavelength region, the star-planet brightness contrast reaches its minimum, the effect becomes more easily detectable in the thermal emission. The phase light curve provide information on day-night temperature difference on exoplanets. Through both secondary eclipse and phase curve analysis it is possible to study the heat distribution and estimate the global atmospheric temperature and albedo (e.g., Knutson et al., 2007; Crossfield et al., 2010; Demory et al., 2012, 2016; Dyudina et al., 2016; Kilpatrick et al., 2017).

1.2.3 Atmospheric studies of non-transiting systems

As mentioned earlier in Section 1.1.2, the transit probability is small and a large number of discovered exoplanets are not transiting. There are a few techniques for unveiling the properties of the atmospheres of the non-transiting exoplanets. I introduce these techniques in the following. I note that these methods can also be applied on transiting exoplanets.

High dispersion technique: The high dispersion spectroscopy, which is introduced in 1.2.1.3, is a great method to unambiguously detect molecules in exoplanetary atmospheres and it has resulted in the detection and abundance estimation of CO, CO_2, and H_2O in the IR wavelength range in the day-side emission spectrum of non-transiting exoplanets (e.g., Brogi et al., 2012; Lockwood et al., 2014; Birkby et al., 2017). Through this method, the orbital inclination of non-transiting exoplanets can be determined as well (e.g., Rodler et al., 2012).

High contrast imaging: Using Integral Field Spectroscopy (IFS), it is possible to obtain the exoplanetry atmospheric spectrum in the direct imaging technique. An IFS allows gathering of spectra over a grid in the two-dimensional field of view. Hence, it is possible to study an extended object, such as a protoplanetary disk or an exoplanet orbiting its host star (e.g., Sparks & Ford, 2002). Instruments such as the Gemini Planet Finder (GPI, Macintosh et al., 2014) and spectro-polarimetric high-contrast exoplanet research (SPHERE, Mesa et al., 2011) are capable of performing such studies. The atmospheres of the directly imaged exoplanets have been investigated in the mid-IR region through spectroscopic observations. Since these systems are still within their debris disk or at the late stages of planet formation, in most of them either the scattered light from the star (Currie et al., 2012) or a very cloudy and hazy atmosphere (Currie et al., 2013) has been detected. As other examples, the planet, HR 8799c shows signatures of water and carbon monoxide (Konopacky et al., 2013) and HD 8799b has a hydrogen-rich cloudy atmosphere with signatures of carbon dioxide and methane (Barman et al.,

2011). Further, investigations of other exoplanets in the multi-planetary system HR 8799 have shown that two of the exoplanets (HR 8799d and HR 8799e) in this system show spectra similar to those of brown dwarfs of type L6-L8 (Zurlo et al., 2016; Bonnefoy et al., 2016). A recent idea for the direct imaging of nearby smaller exoplanets with the current facilities, is to enhance the contrast level between the planet and the star, by combining the high contrast imaging with the high dispersion spectroscopy (Lovis et al., 2017). As mentioned in Section 1.1.3, so far direct imaging has only worked for a hand-full of very young and hot giant exoplanets at large orbital distances. But the next-generation ground-based telescopes such as ELT, will be capable of characterizing smaller exoplanets and exoplanets with an angular separation of ∼50 mas from their host stars.

Variations in the thermal emission or reflection: Similar to phase curves in transits, variations in the thermal emission in non-transiting exoplanets can be used to probe the exoplanet atmosphere (e.g., Selsis et al., 2011). Similarly, the reflected stellar light from the exoplanet, can be captured in the optical region during the phase curve variation. The presence or absence of an atmosphere makes a considerable difference in the heating distribution and potentially this can be used in the future to detect the atmospheres of small rocky exoplanets (e.g., Kreidberg & Loeb, 2016).

1.3 Impeding effects

Issues hindering the analysis of transmission spectroscopy can be grouped into two categories: Those related to the host star and those related to environmental/instrumental systematics. Consideration of these error sources is a crucial step in the successful characterization of exoplanetary atmospheres. These non-exoplanetary effects are further explained in the following.

1.3.1 Stellar effects

Variations in the host stars spectrum inevitably influence the exoplanetary observations and may lead to a wrong interpretation of the data if ascribed to the planet. Stellar activity such as flares, spots, and plages and the effects of stellar rotation (Rossiter-McLaughlin effect) alter the shape of stellar spectral lines. The magnitude of these effects can reach or even exceed the level of the exoplanetary signals. Depending on the stellar type, the differential limb-darkening can be another error source. In the following subsections I will describe the negative influences of stellar activity, stellar limb-darkening and stellar rotation on transmission spectra, and will introduce methods for their identification.

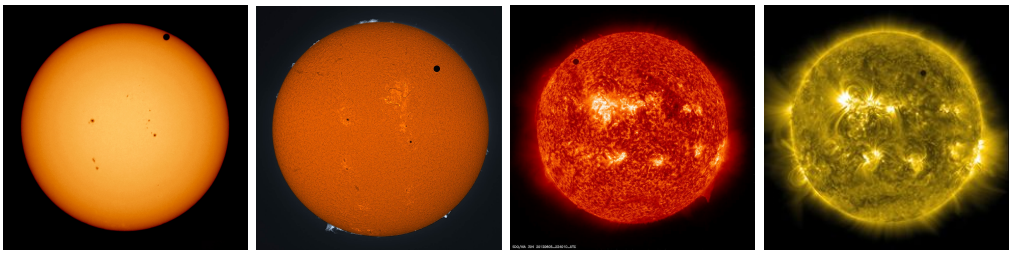

FIGURE 1.10: Transit of Venus in four wavelength filters. The panels from **left to right** show the optical broadband, optical H_α line (6563 Å), UV (He II at 304 Å) and X-ray (Fe IX at 171 Å) images of the Sun during the Venus transit in 2012 (H_α image credit: C. Hetlage, the rest of images are taken from the NASA Solar Dynamics Observatory).

1.3.1.1 Stellar activity

Understanding different activity related processes that are occurring on the surface and in upper atmospheric layers of the host star is crucial in the detection and characterization of exoplanets. Figure 1.10 shows four images of the Sun during the Venus transit in 2012. These images are taken at optical board-band, H_α, UV and X-ray wavelengths and they all show some signatures of stellar activity in different layers of the solar atmosphere. These layers from bottom to top are, photosphere, chromosphere, transition region and corona. In the optical broadband image, the light mainly originates in the photosphere, where spots and limb-darkening (see Section 1.3.1.2) are observable. Through a narrow-band Hα filter, dark solar spots and bright areas in their vicinity known as "plage regions", as well as solar granulation can be studied. Hot areas in the upper chromosphere and lower transition region can be seen in the UV image. Through the X-ray image, we can observe the corona and coronal flares. Flares are caused by the re-connection of magnetic flux in the corona, and usually influence the layers beneath the corona (e.g., the choromosphere and the transition regions) as well. As the figure shows, activity features of the Sun reach or even exceed the relative size of the transiting planet. In addition, the planet may pass over any of these regions. The Venus transit example clearly shows what can be expected when exoplanets traverse over stellar active regions: Anomalies in the photometric or spectroscopic measurements are caused (see Llama & Shkolnik, 2015).

The impact of stellar spots, plages, and flares on transmission spectroscopy and the available methods for the identification of such stellar features are described below.

Spots and Plages: The spots that are not located in the path of the exoplanetary transit are known as un-occulted spots. The un-occulted spots appear brighter in longer wavelengths and darker in shorter wavelengths. Similar to the planet that blocks the stellar light, un-occulted spots reduce the stellar light that reaches us. Considering that the planetary radius is measured based on the total obscuration of the stellar flux,

spots cause an over estimation of the planetary radius. This overestimation is more prominent in shorter wavelengths, thus this wavelength-dependent effect, produces a fake Rayleigh scattering slope. Similarly, stellar plages exhibit a higher contrast in shorter wavelengths and can mimic the same effect as un-occulted spots. In contrast, if spots are covered by an exoplanet, the dark regions on the stellar surface are reduced during the occultation. Therefore, occulted spots cause an underestimation of the planetary radius, which is stronger in shorter wavelengths (Oshagh et al., 2014). Hence another wavelength-dependent effect which is not caused by the exoplanetary atmosphere is made.

It is not possible to directly image other stars, but there are methods to identify and monitor their activity. For example, in high signal-to-noise photometric time series of a transit, anomalies in the light curve could be due to the passage of a planet over a dark or bright spot of the star (e.g., Pont et al., 2007; Wolter et al., 2009; Mancini et al., 2015). If the planet covers a dark stellar spot, the net area of darker regions on the stellar disk is reduced, thus the flux we receive slightly increases. Plages have a similar but reverse effect, meaning that for a short time the flux in the light curves additionally decreases. Observing spots in the primary transit light curve is a clue for the existence of more spots on the stellar surface (e.g., Sedaghati et al., 2017). However, studying of the un-occulted dark and bright regions is not easy and usually requires long-term monitoring of the target host star. For instance, one method to map spots in a relatively rapidly rotating star (roughly ~ 15 kms$^{-1} < v \sin(i) <\sim 120$ kms^{-1}) is the Doppler imaging technique (e.g., Strassmeier, 2002; Wolter et al., 2005). This technique is based on monitoring of the deformations of the high-resolution spectral lines which are caused by stellar spots. The spectral line deformation caused by the spot rotates with the star according to the spot's Doppler velocity.

In addition, since stellar activity is directly correlated with the strength of the stellar magnetic fields, a polarimetric study of the host star, known as Zeeman Doppler imaging, can be used to identify the stellar spots (e.g., Piskunov & Kochukhov, 2002; Kochukhov et al., 2004; Lüftinger et al., 2010). These methods cannot be used for slow rotating (roughly slower than 10 kms^{-1}) stars. Only long-term observations of these stars can result in some clues about their temperature variations and activity cycles and thus the expected relative amount of spots(e.g., O'Neal et al., 1996; Catalano et al., 2002; Gray, 2004; Frasca et al., 2005). The positive aspect of slow rotators is that in general these stars are magnetically less active and can often be assumed to be non-active host stars.

Flares: The flaring activity of a host star can strongly change the shape of stellar spectral lines and increase the amount of flux that we receive from the system. Hence, if a flare happens during a transit observation, the shape of the exoplanetary transit light

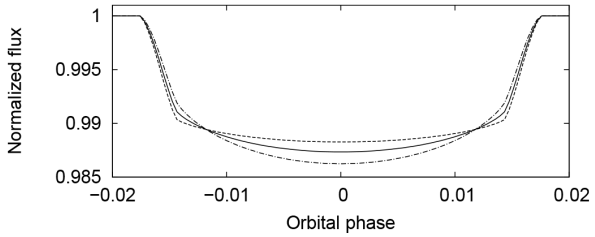

FIGURE 1.11: Differential limb-darkening effect. The transit light curves at different wavelength bands have different limb-darkening coefficients which effect the shape and depth of light curves. (Adopted from Czesla et al. 2015).

curve and its atmospheric excess light curve changes as well. Therefore, the identification of stellar flares and mitigating their impact are important steps in analysis of transit observations and particularly in transmission spectroscopy. Flares can be easily recognized in X-ray data, but when dealing with transmission spectroscopy X-ray observations are usually not available. Stellar flares can be identified by measuring variations in the strength of chromospherically active spectral lines such as H_α (6563 Å), Ca II H & K (3968, 3934 Å), and Ca II IRT (8498, 8542, 8662 Å) lines (e.g., Chmielewski, 2000; Cincunegui et al., 2007).

One of the standard methods for the evaluation of the strength of the Ca II H & K (3968, 3934 Å) lines is the Mount Wilson S-index (Duncan et al., 1991). The S-index is proportional to the integrated flux in the line cores divided by reference bands in the continuum near the line and was originally measured using narrow-band photometric filters. The S-index can also be used in high-resolution spectra to identify stellar flaring activity. With a similar approach, the indices in other activity indicating lines are also measurable. Observing similar behaviour in the temporal changes of different indices is a confirmation on the occurrence and the shape of the influence of the flaring event (e.g., Klocova et al., 2017, see also Section 2.6.1).

1.3.1.2 Stellar differential limb-darkening

From the upper layers of the stellar photosphere, almost all the photons can escape, but deeper into the stars, less photons are able to escape. At an *optical depth* equal to 1, only $1/e$ (where e is Euler's number) of photons can leave the photosphere and at a distance equal to a few optical depth, the star becomes totally opaque. The optical depth of 2/3 is often used to define the photosphere height (Eddington Approximation).

The radial temperature decrease through the atmospheric layers of a star is responsible for the so called limb-darkening effect: When we look at the center of a stellar disk, escapes from deeper and hotter regions while, the radiation from the stellar edge comes from layers that are relatively higher and thus cooler. Hence, in the optical range of the spectrum, the limb of a star appears darker compared to the center. Equation

7 in Chapter 2 quantifies how the intensity of stellar light changes from the center to the limb. Limb-darkening is a wavelength-dependent effect, which can be seen in Figure 1.10. Optical, UV, and X-ray images show a different limb-darkening behaviour in the Sun. In contrast to the photosphere (optical wavelengths), in the corona (X-ray) we see limb-brightening. The corona is optically thin, thus looking at the limb, we see through more material compared to the center. Changes of the limb-darkening with wavelength is known as differential limb-darkening effect. This means that the limb-darkening coefficients (also introduced in Equation 7 in Chapter 2) vary at different wavelengths. Thus, as shown in Figure 1.11 the transit light curve has a different shape and depth at different wavelength bands. As a result, the differential limb-darkening must be taken into account before interpreting an exoplanetary atmospheric signal (e.g., Czesla et al., 2015; Müller, 2016).

1.3.1.3 Rossiter-McLaughlin effect

While the star is rotating, one quadrant of the stellar surface is moving toward us (blue-shifted) and the other quadrant moves away from us (red-shifted). As a result, stellar rotation causes broadening of stellar lines. When a planet transit its parent star, based on the transit trajectory, a fraction of the red- and blue-shifted part of the star will be covered at different times. Originating from the study of eclipsing binaries, this phenomenon is known as Rossiter-McLaughlin (RM) effect (Rossiter, 1924; McLaughlin, 1924). The RM effect alters the broadening of the spectral lines thus slightly deforms the spectral line shape. The effect therefore has an imprint on the radial velocity curves. As shown in Figure 1.12-right, when a blue-shifted region is covered, the star appears redder and when a red-shifted region is blocked, the star becomes bluer (Ohta et al., 2005; Winn, 2007; Gaudi & Winn, 2007). The RM effect is useful in exoplanetary characterization. First of all, using the RM effect, we can figure out the projected trajectory of the exoplanet on the stellar disk and infer prograde or retrograde motion (Winn et al., 2011) of the exoplanet (see Figure 1.12-left). Hence, we can obtain the projected spin-orbit angle (e.g., Sanchis-Ojeda et al., 2013) and the stellar obliquity (e.g., Cegla et al., 2016). In addition, the RM effect is a wavelength dependent phenomenon and similar to transmission spectroscopy it depends on the effective size of the planet that covers the star. It can be used to characterize exoplanetary atmospheres (Snellen, 2004; Dreizler et al., 2009), such as the measurement of the atmospheric Rayleigh scattering slope (e.g., Di Gloria et al., 2015; Yan et al., 2015).

In high-resolution observations of planetary transit the RM effect can negatively affect the analysis of transmission spectroscopy due to the deformation of the spectral lines. The deformation of a line is illustrated in Figure 1.12-right. The second row in this illustration depicts the case in which the rotational broadening is much larger than other broadening mechanisms (e.g., thermal broadening, pressure broadening). The

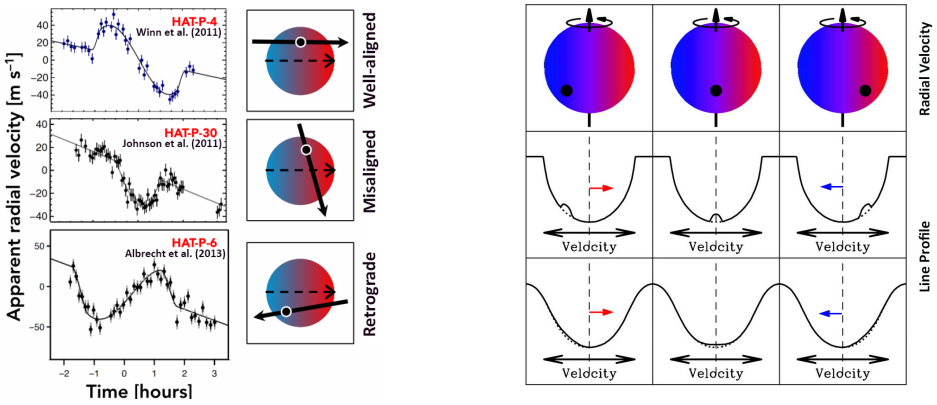

FIGURE 1.12: Demonstration of the RM effect. **Left:** Rossiter-McLaughlin effect reveals the projected trajectory of the transit through study of the radial velocity curve. Three cases of well-aligned (Winn et al., 2011), misaligned (Johnson et al., 2011) and retrograde (Albrecht et al., 2013) motions are shown (Adopted from https://web.astro.princeton.edu/research/planetary-astrophysics). **Right:** The shape of the spectral line profile varies as a result of RM effect (Adopted from Gaudi & Winn 2007).

last row, illustrates the RM effect on a spectral line when the stellar rotational is not dominating. RM effect causes a misalignment in the line centers of spectral lines in exposures taken at different times. If the trajectory covers the same amount in red as in the blue-shifted part of the star, then the deformation is symmetric and averages out in the integration. However, most of the time the trajectory is not completely symmetric, hence corrections must be taken into account for achieving accurate interpretations about the exo-atmospheric conditions (e.g., Louden & Wheatley, 2015; Wyttenbach et al., 2017).

1.3.2 Environmental and instrumental effects

Besides the influence of the host star on observations of exoplanets, also the used equipment and environmental conditions can play a role. The ideal case in astronomical observations is when the only source of noise is the photon noise. However, environmental and instrumental effects do not allow to easily achieve the photon noise limit. Focusing on ground-based optical and near infrared observations, the main environmental limiting factor is the contamination of spectra (or photometric data) by the Earth's atmosphere or the so-called telluric effects. These comprise the absorption or emission by the Earth's atmospheric constituents (e.g., absorption by water vapor and oxygen), seeing, wind, humidity and temperature changes. There are several techniques for mitigation of some of these effects. For instance, observations of fast rotating A- or B-type stars as telluric standards, or constructing telluric models using radiative transfer codes that simulate the interaction of the incoming light with the Earth's atmosphere (Moehler et al., 2014; Smette et al., 2015; Rudolf et al., 2016), can be used to remove a major part of the contamination of the telluric lines. Optimization of the removal of the

telluric contamination in the specific wavelength regime where we perform the transmission spectroscopy is required to reach the photon noise limit in the analysis. This is however outside the scope of this thesis, but must be carefully considered in the future, specifically when we are dealing with the characterization of Earth-size exoplanets.

Generally, both ground- and space-based observations may suffer from instrumental limitations and systematics, such as blaze patterns in spectroscopy or tilts and periodic deformations in the raw light curves in photometry. Most of these issues are corrected in the pipelines of the corresponding instruments. However, instrumental systematics might still exist, due to imperfections in the design of the pipeline or appearance of instrumental effects that were previously unknown to the pipeline. Understanding such systematics and developing an algorithm for their mitigation in a transit observation are important steps in the data analysis (e.g., Nortmann et al., 2016; Gibson et al., 2013; Wakeford et al., 2016).

1.4 This thesis

In the optical region of the spectrum, transmission spectroscopy has been the most successful method for unveiling the chemical and physical properties of exoplanetary atmospheres. Considering our current observing facilities, the extended atmospheres of hot-Jupiters are good targets for atmospheric characterizations. Current ground-based instruments are capable of performing such studies, however optimal extraction of exoplanetary atmospheric signals is required with careful handling of the aforementioned non-planetary issues. In this thesis, I develop a framework for the optical high-resolution narrow-band transmission spectroscopy technique, taking into account the dominant effects of the host star. Since sodium has a relatively large absorption cross section, I mainly focus on the investigation of this element. As a novel section of this framework, I created a model to explain a *bump* that has been typically observed in the exo-atmospheric transit light curves near the mid- transit time, by studying the *changing planetary RV* during the transit. I apply my framework to the data sets of two hot-Jupiters and extract some of their physical characteristics.

In Chapter 2, I focus on the high-resolution narrow-band transmission spectroscopy of the hot-Jupiter HD 189733b using ultraviolet and visual echelle spectrograph (UVES) mounted on Very Large Telescope (VLT). The host star is an active K-type star, which is affected by a flare during the observation. After modelling the impact of the stellar flaring activity, differential limb-darkening, and changing planetary radial velocity on the excess light curves, I detect sodium in this target's atmosphere and measure the additional absorption in different passbands. This analysis allows to measure the shape of an exoplanetary spectral line directly from the excess light curves.

In Chapter 3, I use observations of the Magellan Inamori Kyocera echelle (MIKE) spectrograph on the Magellan telescopes and apply the narrow-band technique on WASP-17b, which is orbiting a F-type star. I investigate the atmospheric excess absorption light curves of this target with a similar method is explained in Chapter 2. Since no flaring event is detected during the observation of this target, I additionally obtain the transmission spectrum in the sodium region through division of in-transit by out-of-transit spectra. Ultimately, through comparison of the observational results with the planetary retrieval atmospheric models I constrain the atmospheric temperature and the radius of the exoplanet. The results of analysis of HD 189733b and WASP-17b are then compared to each other and the framework is ready for quick application on other targets.

In Chapter 4, I summarize the work and discuss the advantages and limitations of the technique that I have developed. Finally, I present an outlook on the future of transmission spectroscopy and the upcoming missions and telescopes aiming at the detection and characterization of Earth-size exoplanets.

Chapter 2

Exoplanetray atmospheric sodium revealed by orbital motion

Context: During primary transits, the spectral signatures of exoplanet atmospheres can be measured using transmission spectroscopy. We can obtain information on the upper atmosphere of these planets by investigating the exoplanets' excess sodium absorption in the optical region. However, a number of factors can affect the observed sodium absorption signature. We present a detailed model correcting for systematic biases to yield an accurate depth for the sodium absorption in HD 189733b.

Aim: The goal of this work is to accurately measure the atomspheric sodium absorption light curve in HD 189733b, correcting for the effects of stellar differential limb-darkening, stellar activity, and a "bump" caused by the changing radial velocity of the exoplanet. In fact, owing to the high cadence and quality of our data, it is the first time that the last feature can be detected even by visual inspection.

Method: We use 244 high-resolution optical spectra taken by the UVES instrument mounted at the VLT. Our observations cover a full transit of HD 189733b, with a cadence of 45 seconds. To probe the transmission spectrum of sodium we produce excess light curves integrating the stellar flux in passbands of 1 Å, 1.5 Å, and 3 Å inside the core of each sodium D-line. We model the effects of external sources on the excess light curves, which correspond to an observed stellar flare beginning close to mid-transit time and the wavelength dependent limb-darkening effects. In addition, by characterizing the effect of the changing radial velocity and Doppler shifts of the planetary sodium lines inside the stellar sodium lines, we estimate the depth and width of the exoplanetary sodium feature.

Results: We estimate the shape of the planetary sodium line by a Gaussian profile with an equivalent width of $\sim 0.0023 \pm 0.0010$ Å, thereby confirming the presence of sodium in the atmosphere of HD 189733b with excess absorption levels of 0.72 ± 0.25 %, 0.34 ± 0.11 %, and 0.20 ± 0.06 % for the integration bands of 1 Å, 1.5 Å, and 3 Å, respectively. Using the equivalent width of the planetary sodium line, we produce a first order estimate of the number density of sodium in the exoplanet atmosphere.

S. Khalafinejad, C. von Essen, H. J. Hoeijmakers, et al.
*A&A, **598**, A131 (2017)*

2.1 Introduction

The first transiting hot-Jupiter, HD 209458b, was discovered more than a decade ago (Charbonneau et al., 2000). Since then a few thousand transiting exoplanets have been detected with various transit surveys from ground-based facilities (e.g., Hartman et al., 2004b; Pollacco et al., 2006), and from space (e.g., Borucki et al., 2010; Koch et al., 2010). This has provided a fertile ground for studying the exoplanet population from a global point of view (Sing et al., 2016), and has opened a window to a deeper characterization of planetary systems.

Transiting systems allow the study of their atmospheres via reflection and transmission spectroscopy (see the review paper by Burrows, 2014, and references therein). During primary transit, the exoplanet blocks part of the stellar light. If the planet has an atmosphere, an additional fraction of the stellar light can be absorbed by the materials present in its atmosphere. Since this absorption takes place at discrete wavelengths, the planet size and the transit light-curve depth will appear larger or smaller, depending on the wavelength of the observation. As a result, the variations in the transit depth as a function of wavelength can reveal the presence of different atomic and molecular species (e.g., Charbonneau et al., 2002; Tinetti et al., 2007; Vidal-Madjar et al., 2011; Crossfield et al., 2011; Désert et al., 2009; Hoeijmakers et al., 2015; Nikolov et al., 2015), clouds (Gibson et al., 2013; Kreidberg et al., 2014), and hazes (Pont et al., 2013).

Most of the spectro-photometric measurements of exoplanet atmospheres have been performed through space-based observations (e.g., Deming et al., 2013; Sing et al., 2016). Although these instruments have superior stability and sensitivity, their low spectral resolution can only constrain some atmospheric models. So far, high-resolution spectroscopy has only been performed using ground-based facilities, and despite the added complications posed by the Earth's atmosphere, ground-based high-resolution studies have added valuable contributions to our understanding of exoplanetary atmospheres. For example, at resolutions of $R \sim 10^5$, the absorption lines of individual chemical species can be spectroscopically resolved (Birkby et al., 2013; Rodler et al., 2012; de Kok et al., 2013; Lockwood et al., 2014; Brogi et al., 2012), as can the orbital motion, diurnal rotation of the planet, and exo-atmospheric wind speed (Snellen et al., 2010, 2015; Louden & Wheatley, 2015; Brogi et al., 2012). Even large-scale dynamics in the upper atmosphere have already been detected (see, e.g., Kulow et al., 2014; Ehrenreich et al., 2015).

Studies of the optical transmission spectra (mainly performed by the Hubble Space Telescope, HST) have revealed that many hot-Jupiters have featureless spectra with strong Rayleigh scattering slopes toward short wavelengths (Pont et al., 2008; Sing et al., 2011; Huitson et al., 2012; Nikolov et al., 2015; Sing et al., 2016). This has been attributed to the presence of high-altitude clouds and haze layers that effectively obscure absorption features by making the upper atmosphere opaque. In these cases,

only species that are present in the uppermost layers of the atmosphere can be observed. Indeed, models indicate that only a handful of such species are expected to be present in the optical region (see, e.g., Fortney et al., 2010; Seager & Sasselov, 2000; Brown, 2001), in consequence making neutral sodium one of the most intensively studied alkali metals to date.

Exoplanetary sodium absorption was first detected by Charbonneau et al. (2002) in the atmosphere of HD 209458b by analyzing spectro-photometric data obtained by the HST during transit. Then, Redfield et al. (2008) claimed the first ground-based detection of sodium in HD 189733b and in the same year, Snellen et al. (2008) reported the ground-based detection of sodium in HD 209458b. Altogether, sodium has been detected in a handful of hot-Jupiter atmospheres: HD 209458b (Charbonneau et al., 2002; Snellen et al., 2008), HD 189733b (Redfield et al., 2008; Jensen et al., 2011; Huitson et al., 2012), WASP-17b (Wood et al., 2011; Zhou & Bayliss, 2012), and XO-2b (Sing et al., 2012) are classical examples. Recently, Wyttenbach et al. (2015) reported the ground-based detection of sodium in HD 189733b using observations collected during three transits with the HARPS spectrograph. Cauley et al. (2016) also analyzed the pre-transit and in-transit phases at different atomic absorption lines, consisting of sodium.

In this [chapter], similar to Redfield et al. (2008) and Wyttenbach et al. (2015), we present the results of our efforts in the detection of atmospheric sodium in the transmission spectrum of the hot-Jupiter HD 189733b. We analyze a single transit observed with the high-resolution Ultraviolet and Visual Echelle Spectrograph (UVES) at ESO's Very Large Telescope and we apply a detailed modeling of the systematics. We also estimate the equivalent width of the exoplanetary sodium line using the deformations introduced in the excess light curves by the changing radial velocity of the planet, and with it we estimate the abundance of sodium in the atmosphere. In Section 2.2 we describe our observations and the data reduction steps. We continue in Section 2.3 with a detailed description of the data analysis, the transmission spectroscopy method, and the modeling procedure. We show our results and the discussions in Section 2.4, and conclude in Section 2.5. [Finally, in Section 2.6 we provide some complementary materials regarding the study of a flare in HD 189733b, the construction of the transmission spectrum for this planet, and the background information on the statistical tool that is used in this chapter]

2.2 Observations and data reduction

2.2.1 Our target

The hot-Jupiter HD 189733b orbits a bright (V$\sim$ 7.7) and active K-type star every $\sim$2.2 days. HD 189733b has an atmosphere with a scale height of about 200 km (Désert et al., 2011). Thanks to its large scale height and bright host star, this exoplanet has

TABLE 2.1: Adopted values for the orbital and physical parameters of HD 189733 during the fitting procedures in this work.

Parameter	Symbol	Value	Reference
Orbital inclination	i (°)	85.710 ± 0.024	Agol et al. (2010)
Semi-major axis	a (a/R_S)	8.863 ± 0.020	Agol et al. (2010)
Planet to star radius ratio	R_P/R_S	0.1565	Sing et al. (2011)
Mid-transit time	T_0 (BJD_{TDB})	2454279.436714 ± 0.000015	Agol et al. (2010)
Orbital Period	P (days)	2.21857567 ± 0.00000015	Agol et al. (2010)
Stellar effective temperature	T_{eff} (Kelvin)	4875 ± 43	Boyajian et al. (2015)
Stellar surface gravity	log g (dex)	4.56 ± 0.03	Boyajian et al. (2015)
Metallicity	[Fe/H]	-0.030 ± 0.08	Torres et al. (2008)
Stellar radius	R_S ($R_\odot$)	0.756 ± 0.018	Torres et al. (2008)
Stellar rotation period	P_S (days)	11.953 ± 0.009	Henry & Winn (2008)

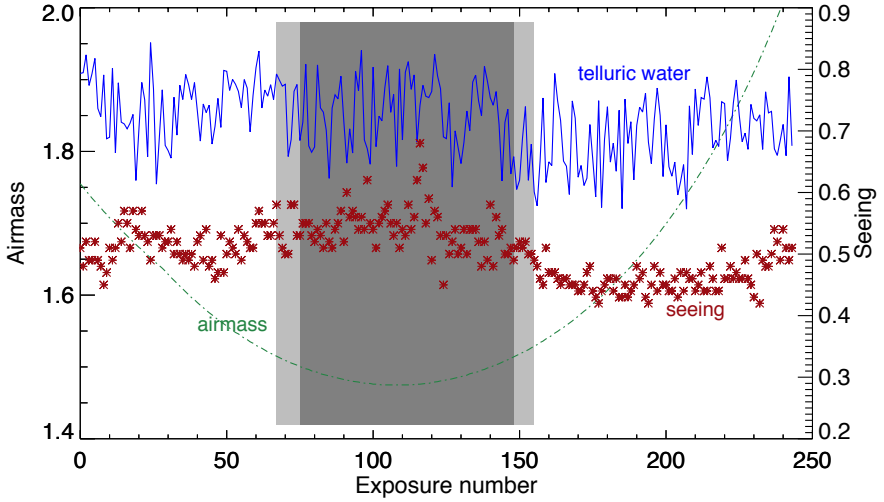

FIGURE 2.1: Sky conditions during our observations. The airmass is indicated with a green dashed line and the red cross points indicate the seeing, in arcsec. The measured strength of several strong telluric water lines are shown with solid blue lines. These values are artificially shifted to fit inside the plot. Gray areas show the time between transit ingress and egress. Dark gray is the transit at full depth.

turned into one of the favorite targets for atmospheric characterization. Especially in the case of ground-based studies, HD 189733b is an excellent "testbed" to explore new exoplanet atmospheric observation and characterization techniques. The orbital and physical parameters of this system adopted in this work are summarized in Table 2.1. To be consistent with current data, we adopt the planet-to-star radius ratio obtained by the Sing et al. (2011) HST observations around the sodium wavelength. However, we note that within the precision of our data other reasonable values of R_P/R_S would have produced similar results to the ones presented in this work.

2.2.2 Observing log and instrumental setup

During the night of July 1, 2012, a transit of HD 189733b was observed using UVES (Dekker et al., 2000) mounted on Kueyen, UT2 (Program ID: 089.D-0701 A). During the observations 244 spectra were acquired: 67 exposures before ingress, 88 exposures during transit, and 89 exposures after egress. The first 29 spectra have an exposure time of 30 seconds, while all of the rest were exposed for 45 seconds. The data were taken using the dichroic beam splitter with central wavelengths around 760 nm in the red arm and 437 nm in the blue arm. Our target lines are located in the red arm, where the slit width was 0.7" and the spectral resolution is about 60 000. We estimate a signal-to-noise ratio around the sodium lines of approximately 100. The sky conditions (airmass, seeing, and telluric water) are shown in Figure 2.1. As the figure shows, the depths of water lines follow a trend similar to the seeing. However, the water lines do not clearly correlate with airmass. We calculate the strength of the water lines by measuring and averaging the equivalent widths of the six strongest water lines and the values for airmass and seeing are extracted from the image headers.

2.2.3 Data reduction

The initial data reduction and extraction of 1-D spectra were performed using the UVES pipeline, version 5.2.0 (Czesla et al., 2015). The subsequent analysis related to this work was conducted using Interactive Data Language (IDL) and Python 2.7. The sequence of the reduction processes are summarized below.

2.2.3.1 Spectrum normalization

The first step was to normalize the continuum of the spectra in the region around the sodium lines. During the initial reduction we removed the instrumental blaze function from each individual spectral order. However, the spectra were still not properly normalized since we observed variations in the continuum. To correctly normalize the spectra we first obtained the average spectrum of all the available reduced spectra. Then we divided this average spectrum into 60 wavelength regions within a range of 400 Å around the sodium lines. By linearly interpolating the maximum values within each bin we obtained the shape of the continuum in the averaged spectrum. Finally, each individual spectrum was divided by this interpolation.

2.2.3.2 Spectrum alignment

Owing to the Earth's rotation and instrumental instabilities, the wavelength solution of our spectra slightly drifts (up to about $\pm$ 1 km/s). To correct for these shifts we identified 80 stellar absorption lines in a range of 400 Å around the sodium lines. We then fitted a Gaussian profile to each one of the line cores to obtain the position of each

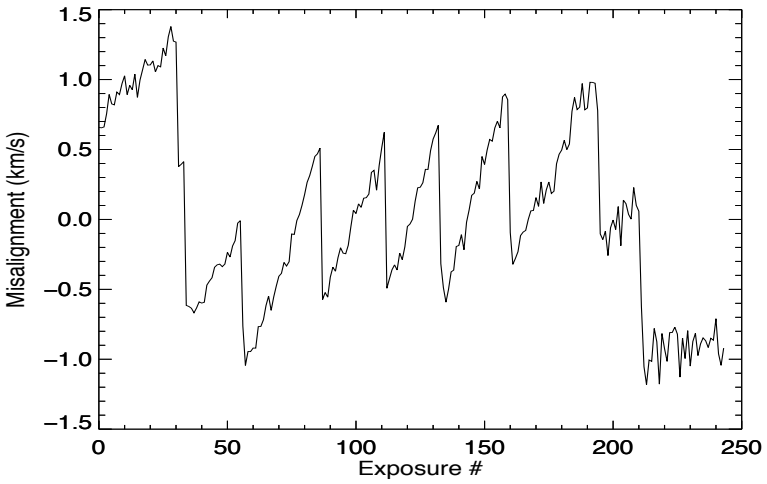

FIGURE 2.2: Misalignment of each spectrum with respect to a reference spectrum taken in the middle of the observing run.

line center. For each line we then calculated the time-averaged line position and thus obtained the deviation of each line in each order of each exposure. The strongest component is a wavelength-independent offset caused by the entire spectrum being shifted on the detector. There may also be wavelength-dependent deviations caused by a magnification, i.e., a scaling of the image of the spectra on the detector, so we performed a linear fit to the values of the misalignment of all lines in the exposure to obtain a 2-D map of the misalignment (shift map) as a function of wavelength. By re-interpolating all exposures to this map, all absorption spectra were aligned, and thus placed in the same reference frame. The amplitude of the fitted linear shift is plotted in Figure 2.2, which shows that the spectra drift in time according to a saw-tooth pattern, also identified and described by Czesla et al. (2015). The value of the shift in pixels rises to about ± 0.5 px. To study the wavelength stability of this dataset, Czesla et al. (2015) also obtained the radial velocity variations of the telluric water lines in time. Since they show the same saw-tooth behavior, we consider this to be an instrumental effect that is likely produced by the movement of the stellar seeing disk inside the slit. After removing the telluric water lines (see Section 2.2.3.3), we aligned all spectra to a common rest-frame using the shift map.

2.2.3.3 Telluric correction

The Earth's telluric water and oxygen lines are removed using the telluric absorption model described in Husser & Ulbrich (2014) and Husser et al. (2015). This model determines the parameters for the stellar and Earth atmospheres simultaneously, and fits the widths and depths of the lines. Each spectrum is then divided by its corresponding telluric model to correct for telluric effects. It should be noted here that visual inspection of the telluric sodium lines in the spectra at the expected location revealed no telluric

sodium feature. In addition, the object distance is relatively close (∼19 pc), which agrees with the observed lack of interstellar sodium.

2.3 Data analysis and modeling

2.3.1 Excess light curve

Since the absorption cross-section of species in the atmosphere is wavelength-dependent, the planetary radius as measured by the depth of the transit light curve is wavelength-dependent as well. We therefore can infer the presence of an absorbing species by obtaining the transit light curve at that wavelength at which a given species is expected to absorb (integration band), and compare it with the transit light curve at a wavelength where the exoplanet atmosphere is transparent (reference band). This comparison is made by computing the ratio of the two light curves, referred to as the "excess light curve", where the additional absorption at the wavelength of interest as the transit progresses can be seen (Snellen et al., 2008). In the case of sodium, we are interested in finding the excess absorption around the optical sodium D_1 and D_2 lines. We specifically introduce a central band

$$F_{\rm center}(t) = \int_{\lambda_0-\Delta\lambda}^{\lambda_0+\Delta\lambda} F(\lambda,t)d\lambda \ , \tag{2.1}$$

where $F_{\rm center}$ describes the integrated flux inside the target line that is expected to change in time (t) in the case of exoplanetary atmospheric absorption, and λ_0 is the central wavelength of the target absorption line. We then define left and right reference bands

$$F_{\rm left}(t) = \int_{\lambda_0-N\Delta\lambda}^{\lambda_0-M\Delta\lambda} F(\lambda,t)d\lambda \ , \tag{2.2}$$

and

$$F_{\rm right}(t) = \int_{\lambda_0+P\Delta\lambda}^{\lambda_0+O\Delta\lambda} F(\lambda,t)d\lambda \ , \tag{2.3}$$

where M, N, O, and P are suitably chosen coefficients that determine the location and width of the reference bands in the continuum close to the sodium lines, and $\Delta\lambda$ is half the integration band width. From $F_{\rm left}$, $F_{\rm right}$, and $F_{\rm center}$ we construct the relative line flux, $F_{\rm line}$, defined as

$$F_{\rm line}(t) = \frac{2F_{\rm center}(t)}{F_{\rm left}(t) + F_{\rm right}(t)}. \tag{2.4}$$

The parameter $F_{\rm line}$ is the flux ratio of the integration and reference bands, which determines the excess light curve. In this fashion, all flux variations that affect the central

and the left and right reference bands in the same way cancel out, while variations that affect only the central band such as absorption by the exoplanetary atmosphere remain.

In our analysis we first locate the centroids of each sodium D-line in every reduced spectrum by fitting a Voigt profile. Then we chose flux integration passbands of 1 Å, 1.5 Å, and 3 Å centered on each line to characterize the extra Na I absorption from the planetary atmosphere. The smallest passband width is set by the signal-to-noise ratio in the deep cores of the Na I lines; the aperture needs to be wide enough to include enough photons to be sensitive to small variations in the depth of the Na I lines. The upper limit in the width of the passband is given by the value at which the planetary Na I signal blends with the noise. Specifically, our 3 Å integration aperture upper limit is determined empirically by comparing the standard deviations in the light curves for each passband to that of the reference continuum. The standard deviation of the reference continuum light curve, where one does not expect to have any planetary atmospheric signal, is 0.83 parts per thousand (ppt), which we attribute to random noise. In the case of the Na I line passbands, the standard deviations of the light curves are 1.9 ppt, 1.4 ppt, and 0.85 ppt for the 1 Å, 1.5 Å, and 3 Å passbands, respectively. These values clearly indicate the presence of an additional signal in the 1 Å and 1.5 Å passbands, while the noise level of the 3 Å passband is similar to that of the reference continuum, placing the signal and the noise at the same level. The three integration bands are illustrated in Figure 2.3, left, together with the sections of the spectrum we used as reference continuum. For a comparative analysis of our results with those of other authors, our integration passbands are close to the integration passbands of Snellen et al. (2008), Albrecht (2008), and Wyttenbach et al. (2015). Our reference bands are fixed to the same values for all the integration bands, and are placed closer to the upper wings of the sodium lines to minimize the difference between the limb-darkening (LD) coefficients in the integration and reference bands (see Section 2.3.2.2). We also place them in a location free of strong absorption features. Taking all of this into account, our reference passbands have a width of 1 Å and are placed on each side of each sodium line, as indicated in Figure 2.3. The reference bands between the lines are taken to be the same for both sodium D-lines, otherwise for the D_2 line a fraction of the reference band would fall inside the deep iron line in between the sodium lines.

Finally, we use Equation 2.4 to obtain the relative strength of the sodium absorption features in each exposure. The excess light curves we obtain by using this approach on the sodium D_2 line for the integration bands of 1.5 Å are shown in Figure 2.3, right, and we call it the "raw excess light curve". As the figure shows, the raw excess light curve does not look transit-like and is probably highly affected by external physical, environmental, or instrumental effects. In the next sections we investigate the source of these effects and use them to produce a detailed model fit to the data.

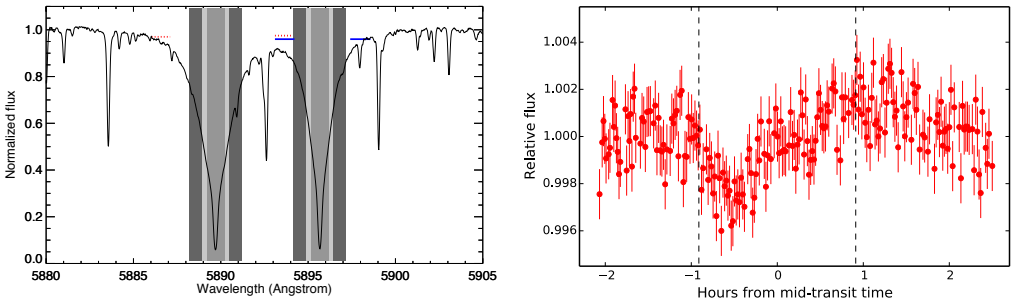

FIGURE 2.3: Integration bands and derived excess light curve. **Left**: Gray shaded areas show the integration bands with passband of 1 Å, 1.5 Å, and 3 Å, centered at the core of each sodium line. The red and blue intervals show the passbands of the reference bands for D_2 and D_1, respectively. **Right**: The raw excess light curve shown with the red circles for the 1.5 Å integration band inside the sodium D_2 line. Dashed vertical lines indicate times of ingress and egress.

2.3.2 Model components and parameters

Before drawing any conclusions on the HD 189733b atmosphere, the external effects present in the raw excess light curves have to be taken into consideration. In total, we identify three main effects: the occurrence of a stellar flare (Czesla et al., 2015; Klocova et al., 2017) starting close to mid-transit time (A); a wavelength-dependent limb-darkening (B); and the observed changes in the line profile produced when the planetary sodium line moves inside the stellar sodium line, induced by the planetary orbital motion (C). In the next sections we explain each effect separately and specify their fitting parameters. The magnitudes of the individual errors for the excess light curves are determined in two ways, by computing the standard deviation of data points between the 30th and 100th exposures, and by computing the standard deviation of the residual light curves produced by subtracting a least-squares fit of the four model components arranged as in Equation 2.9 to the data. For a more conservative approach, the values of the errors are assigned by choosing the largest value between the two approaches.

2.3.2.1 Stellar flare (component A)

HD 189733 has been characterized as a highly active K-type star (e.g., Poppenhaeger et al., 2013). As a result, our observations are prone to being contaminated by stellar flares and/or spots. Indeed, we detect a rising pattern of flux that starts right after the mid-transit point, identified as a stellar eruption. Usually, a clear evidence of a stellar flare can be derived from the measurements of the equivalent widths of emission lines in the cores of Ca II H and K and Hα lines originating in the chromospheric layers (e.g., Klocova et al., 2017). By analyzing these spectral lines, we confirmed the presence of a flare, which – as predicted – effectively took place close to mid-transit time (see top panel

D_2 Core/Ref.	1 Å left fixed ref.	1 Å core	1.5 Å core	3 Å core	1 Å right fixed ref.
λ-range (Å)	[5886.04 , 5887.10]	[5889.42 , 5890.48]	[5889.19 , 5890.71]	[5888.49 , 5891.41]	[5893.38 , 5894.44]
u_1,u_2	0.6856, 0.0760	0.6051 , 0.0149	0.5961 , 0.0318	0.5987 , 0.0556	0.7078 , 0.0187
D_1 Core/Ref.	1 Å left fixed ref.	1 Å core	1.5 Å core	3 Å core	1 Å right fixed ref.
λ-range (Å)	[5893.38 , 5894.44]	[5895.40 , 5896.45]	[5895.17,5896.68]	[5894.46,5897.39]	[5897.51 , 5898.57]
u_1,u_2	0.7078 , 0.0187	0.6813 , 0.0081	0.6244 , 0.0477	0.6300, 0.0606	0.6649 , 0.0947

TABLE 2.2: Limb-darkening coefficients (u_1,u_2) for the sodium D_2 and D_1 integration bands (Core) and fixed reference (Ref.) bands with the specified wavelength ranges (λ-range). Errors of the limb-darkening coefficients are not shown to avoid visual contamination, but are in all cases on the order of 10^{-3}-10^{-4}.

of Figure 11 in Czesla et al., 2015). Although this feature is identified using the Ca II H and K lines, stellar flares might affect other spectral lines. For instance, neutral sodium in the lower stellar atmosphere can be contaminated by this kind of eruption (Cessateur et al., 2010). Therefore, in our specific case of study it is important to consider this time-dependent change in the core of the line as part of our model budget. To mitigate the flare, we made use of the variations in the equivalent width of the Ca II K line (Klocova et al., 2017), and we call this model component the flare profile, $\mathrm{flr}_{\mathrm{Ca}}(t)$. To quantify to what extent the flare correlates with our raw sodium excess light curve, we used a Pearson's correlation analysis. The six computed values of Pearson's coefficient, computed from the two sodium lines times three integration bands, range between 0.25 and 0.45, and their corresponding p-values are in five of the six cases smaller than 10^{-3}. For the 3 Å integration band and the D_2 line, the p-value is 0.02. In these cases, the computed p-values indicate the probability of an uncorrelated system producing data sets that have a Pearson correlation at least as extreme as that computed from these data sets. In other words, they indicate that the null hypothesis, which states that the raw excess light curve and the flare are uncorrelated, can be rejected with high significance. Thus, there is enough statistical evidence that the flare has to be taken into consideration. To mitigate the stellar activity present in our excess light curves, we fitted a scaled version of the Ca II K flare profile to the raw excess light curves with the expression

$$\mathrm{flr}_{\mathrm{Na}}(t) = \mathrm{FL}_{\mathrm{scale}} \cdot \mathrm{flr}_{\mathrm{Ca}}(t) \ , \tag{2.5}$$

where $\mathrm{FL}_{\mathrm{scale}}$ is the fitting parameter that scales the flare, and $\mathrm{flr}_{\mathrm{Na}}$ is the model component that accounts for the stellar flare. Our best-fit model for the Na D_2 line at 1.5 Å integration width, showing its isolated flare component, can be seen in Figure 2.4-A as a solid black line, plotted along with the raw excess light curve in red points.

2.3.2.2 Wavelength dependent limb-darkening effect (component B)

Stellar limb darkening is wavelength-dependent. Thus, the limb-darkening coefficients inside the broad and deep lines are different from the neighboring continuum. Since the

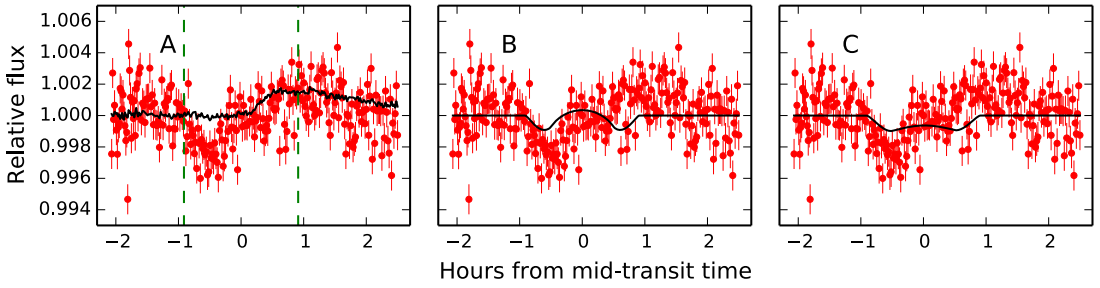

FIGURE 2.4: Individual model components plotted over the excess light curve for Na D_2 at 1.5Å. **Panel A:** Best-fit flare model component. In this panel the green dashed lines indicate the beginning and the end of the transit; **panel B:** Best-fit differential limb-darkening model component; **panel C:** Best-fit changing RV model component, which includes the exoplanetary atmospheric excess absorption in addition to a bump at the center. The final best-fit model, which is the combination of all the model components, is shown in Figure 2.6.

construction of the excess light curve relates the core of the Na D-lines to their near continuum, the difference in limb-darkening values will have an impact on the shape of the excess light curve (see, e.g., Charbonneau et al., 2002; Sing et al., 2008; Czesla et al., 2015). We can formulate this effect using the relation

$$LD = \frac{2 \times \mathrm{LC_{core}}}{\mathrm{LC_{left}} + \mathrm{LC_{right}}} \,, \tag{2.6}$$

where LD is the wavelength dependent limb-darkening model, $\mathrm{LC_{core}}$; $\mathrm{LC_{left}}$ and $\mathrm{LC_{right}}$ are the transit light-curve models from Mandel & Agol (2002) using the orbital parameters tabulated in Table 2.1, which have their own limb-darkening coefficients at the core of the sodium line, and at the left and right reference passbands, respectively (see the limb-darkening model in Figure 2.4-B and Figure 2 of Czesla et al. 2015). To take this effect into consideration we first computed the limb-darkening coefficients in all relevant (integration and reference) passbands using the PHOENIX angle-resolved synthetic spectra (Hauschildt & Baron, 1999; Husser et al., 2013) implementing the method detailed in von Essen et al. (2013). PHOENIX requires effective temperature, surface gravity and metallicity of the star as input, for which we adopted the values $\mathrm{T}_{eff} = 4900$ K, [Fe/H] = 0, and $\log g = 4.5$, closely matching the stellar parameters of HD 189733 listed in this work in Table 2.1. The derived angle-dependent intensities were then fitted with a quadratic limb-darkening law,

$$\frac{I(\mu)}{I(1)} = 1 - u_1(1-\mu) - u_2(1-\mu)^2 \,, \tag{2.7}$$

where $\mathrm{I}(\mu)/\mathrm{I}(1)$ corresponds to the normalized stellar intensity, u_1 and u_2 correspond respectively to the linear and quadratic limb darkening coefficients, and μ is $\cos\theta$, where θ is the angle between the normal to the stellar surface and the line of sight to the observer. In this fashion, $\mu = 0$ refers to the limb, while $\mu = 1$ corresponds to the

center of stellar disk. To carry out the fit between the integrated stellar intensities and Equation 2.7, we consider the μ values between 0.1 and 1 to avoid the steep intensity gradient appearing close to the stellar limb that, if accounted for, would have to be fitted with an added exponential growth to the quadratic function. Since the orientation of the HD 189733b orbit does not produce a nearly grazing transit, the time that the planet spends in the 0-0.1 μ-region is very short and our simplification is justified. The derived values for the sodium D_2 and D_1 lines in their corresponding integration and reference bands are listed in Table 2.2. Here it should be noted that since the integration band widths are, in this work, between 1 and 3 Å, we re-computed the PHOENIX spectra, increasing the spectral sampling to ∼0.1 Å.

As previously mentioned, using the computed limb-darkening values we produce three light-curve models (Mandel & Agol, 2002) and calculate the wavelength dependent limb-darkening model introduced in Equation 2.6. The sensitivity of our data is not high enough to consider the limb darkening coefficients as fitting parameters. Therefore, this model is taken into account but with all their values fixed. The limb-darkening model is shown in Figure 2.4-B as a black line, overplotted onto the raw excess light curve.

2.3.2.3 Planetary radial velocity (component C)

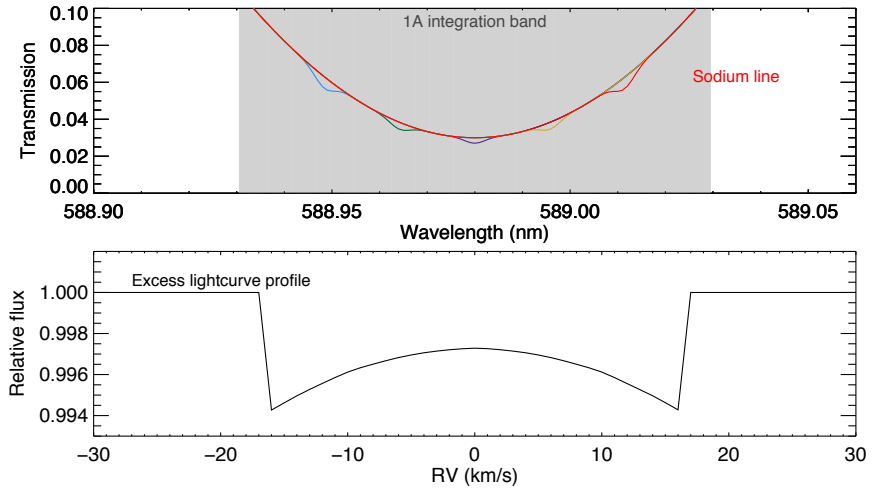

FIGURE 2.5: **Top**: Schematic shift of the planetary sodium line inside the stellar sodium line during the transit. The size of the planetary line has been exaggerated. The gray area corresponds to 1 Å integration band. **Bottom**: Effect of the planetary line shift on the excess light curve with the integration passband of 1 Å, causing a bump that reaches its maximum level around the mid-transit point. We note that the x-axis is also proportional to the transit time, with zero set on the mid-transit point.

Because the planet is moving during its transit on a curved orbit, its radial velocity changes. Hot-Jupiters often have orbital speeds on the order of 100 km/s, which can result in an in-and-out transit radial velocity variation larger than ±10 km/s. This change in radial velocity causes the entire transmission of the exoplanet to be Doppler

shifted, and has already been used to detect molecules in the atmospheres of hot-Jupiters (e.g., Snellen et al., 2010; Brogi et al., 2012; Rodler et al., 2012, using very high-resolution spectra, R∼100 000). In our case as illustrated in Figure 2.5-top, the sodium line originating in the planetary atmosphere shifts between the lower wing and the core of the stellar sodium line. During this shift, the planet atmosphere always absorbs a certain fraction of starlight. In other words, the relative absorption of stellar flux by the planet atmosphere is always the same. This causes the excess light curve to increase at transit center; when the stellar flux is at minimum level, the planetary sodium line is close to the center of the core of the stellar line and the radial velocity of the planet is close to 0. Near ingress and egress, the planetary sodium line is not located in the direct vicinity of the stellar line core. The planetary sodium line at these times is embedded in a part of the stellar line wing where the stellar flux is higher than in the core. Here it absorbs the same fraction of starlight, but this absorption is larger in absolute terms. This causes a "bump" in the bottom of the transit, which is illustrated in Figure 2.5-bottom. This effect was first mentioned by Albrecht (2008) and can also be tentatively seen in the results of the sodium core analysis by Snellen et al. (2008), Zhou & Bayliss (2012), Wyttenbach et al. (2015), and Cauley et al. (2016). In the particular case of HD 189733b, during transit the radial velocity of the exoplanet changes between -16 km/s and +16 km/s. This results in a Doppler shift of approximately ±0.31 Å around the core of the stellar sodium line. We note that with this amount of shift, the exoplanetary sodium absorption line is always embedded in the stellar sodium line of the K-type. To model the radial velocity effect, we time-averaged all out-of-transit spectra to obtain the shape of the stellar sodium lines at high signal-to-noise, and used this as the stellar sodium line template. We represented the planetary line as a Gaussian profile with depth, A_{Na}, and width (Gaussian sigma), σ_{Na}, both considered in this work as fitting parameters. This Gaussian profile is injected into the time-averaged sodium lines calculating the expected radial velocity of the planet (V_R) during each exposure (see Equation 2.8). In other words, we create 244 spectra by multiplying the moving planetary sodium line Gaussian profiles by the time-averaged normalized stellar spectrum. We call this new series of spectra the "convolved spectra". The radial velocity of the planet at each exposure is calculated as

$$\Delta V_R = \frac{2\ \pi\ a}{P} \times \sin[2\ \pi\ \left(\frac{t - t_c}{P}\right)]\ , \tag{2.8}$$

but is converted into wavelength shift to position the center of the Gaussian profile over the stellar sodium template. Here, P is the orbital period, a is the semi-major axis, t is the time of observation for each frame, and t_c is the mid-transit time. The convolved spectra were then integrated following equation 2.4. The result is a numerical model that we call the "initial RV model". In the initial RV model, even the exoplanetary

Gaussian profiles taking place outside transit are also taken into account. However, in transmission spectroscopy the planetary atmosphere is invisible before ingress and after egress. To extract the time span in which the transit takes place and also to correct for the shape of the RV model during ingress and egress, the initial RV model is multiplied by a transit model that has an offset of zero and a normalized depth of one. The result gives us the final RV model. Figure 2.5 is a mock model that illustrates the changing radial velocity effect on the excess light curve for an integration passband of 1 Å. In the figure, the planetary and stellar sodium lines are both represented by Gaussian profiles. Finally, our RV model, as a component of the best-fit model, is plotted over the data in Figure 2.4-C. We note that this model is not completely symmetric since the two stellar sodium lines are not fully symmetric.

2.3.3 Final model and best-fit parameters

The overall model we use to fit the data must be a combination of the model components just introduced (A, B, C) plus a normalization constant (offset or D) for the flare component. None of the model components can reproduce the data when treated individually, thus a combination is required. We choose a model consisting of a multiplication of all of the components plus the offset. The final model is shown in equation 2.9. Since we are dealing with very small effects, the multiplication or summation of the components would both give the same results (see also Czesla et al. 2015):

$$\begin{aligned} M(t_i) &= \mathrm{flr}_{\mathrm{Na}}(t) \times LD(t) \times RV(t) + offset \\ &\equiv A \times B \times C + D \end{aligned} \tag{2.9}$$

The final model (Equation 2.9) has four fitting parameters in total: The flare scaling parameter ($\mathrm{FL}_{\mathrm{scale}}$), the amplitude ($\mathrm{A}_{\mathrm{Na}}$) and width ($\sigma_{\mathrm{Na}}$) of the planetary sodium Gaussian profile, and the normalization constant (offset). Throughout this work, to explore the best-fit parameters and their associated uncertainties we perform a Markov chain Monte Carlo (MCMC) analysis, using the affine invariant ensemble sampler *emcee* (Foreman-Mackey et al., 2013). We employ 100 walkers, with 360 chains each, where the initial positions are synthesized from a Gaussian distribution about our best estimates. All the free parameters have uniform prior imposed. We allow a burn-in phase of $\sim$ 50% of the total chain length, beyond which the MCMC is converged. The posterior probability distribution is then calculated from the latter 50% of the chain.

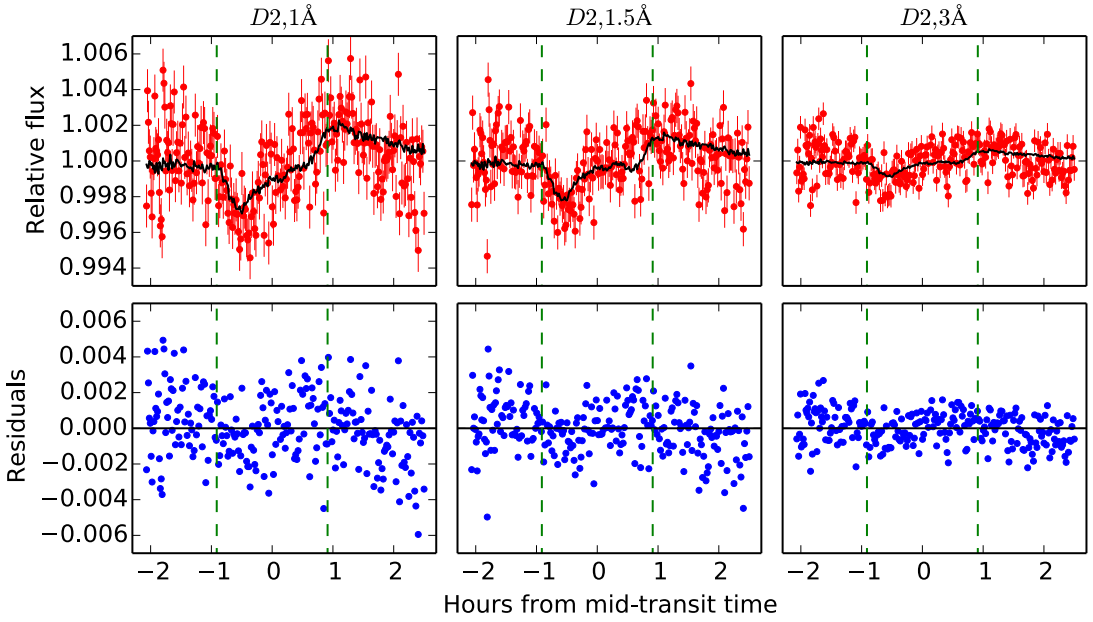

FIGURE 2.6: **First row:** Raw excess light curves on sodium D_2 for integration passbands of 1 Å, 1.5 Å, and 3 Å inside the core of each sodium line. The best-fit model is plotted on top in black. **Second row:** Residuals for each passband D_1.

2.4 Results and discussion

2.4.1 Best-fitting model and errors

Our best-fitting values of the MCMC procedure are summarized in Table 3.3. To illustrate the quality of our fit, Figure A.1 [on page 47] shows the posterior distributions and the correlation plots for all the fitting parameters, computed here as an example for the 1.5 Å excess light curve around the sodium D_2 line. The five remaining excess light curves produce similar plots. As the posterior distributions in Figure A.1 show, the σ_{Na} and A_{Na} parameters are degenerate and the rest of parameters are not correlated at all or only very weakly. However, in this work we use them to calculate the equivalent width of the sodium line (equivalently an area, nothing more than a direct multiplication of both parameters). Therefore, the degeneracy between parameters does not affect our results.

The best-fit model for sodium D_2 passbands and the corresponding residuals are shown in Figure 2.6. As the figure shows, the transit depth, the flare profile amplitude, and the bump strength decrease when the integration passbands increase. In smaller passbands, the planetary signal is more pronounced because there is a higher contrast between the exoplanetary absorption and stellar absorption. Moreover, in smaller integration passbands fewer points are added together and thus – compared to wider passbands where the random noise cancels out better – the light curve is more scattered.

To ensure that equation 2.9 is the best representation of the data, we performed some statistical tests. We made use of the Bayesian Information Criterion (Schwarz, 1978), BIC = χ^2 + k ln N, where k is the number of model parameters and N is the number of data points. The BIC assess model fits penalized for the number of estimated parameters. We also compute chi-square (χ^2) and reduced chi-square (χ^2/ν), being ν the number of degrees of freedom equal to the total number of data points minus the number of fitting parameters for each model combination. Producing this statistical analysis for all the possible combinations of model components would not be very efficient since some of the possible combinations are trivially not the best-fit answer. Therefore, we exclude some of them and pre-selected five different model combinations (modules) using visual inspection as a criterion, and calculated the previously mentioned parameters for each one. Our results for the passband of 1.5 Å is shown in Table 2.3. Tests on other passbands also showed similar results. Based on the values of the table, the models without the flare (component A) and exoplanetary atmosphere absorbing signal (component C) are very poor. Without considering component B, the χ^2, χ^2/ν and BIC values did not change much and even slightly decreased. It is important to keep in mind that the differential limb-darkening is a physical effect that inevitably exists. Without this effect the exoplanetary signal must be overestimated. Therefore, although the goodness of the fit did not change much, component B was also included in defining the best model combination. Thus, briefly, from the minimization of the three statistical tools, we conclude that a good representation of the data is given by a combination of the model components A, B, and C plus the normalization constant D. The final models are introduced in equation 2.9 and the best-fit model for all of the passbands are shown in Figure 2.6. As can be seen in this figure and in Figure 2.4-A, near the end of the observation the flare model does not perfectly fit the data. One probable reason is the shape of the flare at Ca II K lines is slightly different from the shape in sodium lines.

TABLE 2.3: Statistical tests for some model combinations for the 1.5 Å passband.

Test	Module	*k	*N	χ^2	χ^2/ν	BIC
1	A×B×C + D	4	244	312	1.29	333
2	A×B + D	2	244	330	1.36	341
3	A×C + D	4	244	308	1.29	331
4	B×C + D	4	244	365	1.52	382
5	A + E	2	244	356	1.47	367

Furthermore, we tested whether assuming a constant model for the limb darkening effect has an impact on our results. A change in the LD model would be the product of miscalculated limb darkening values. Since there is no empirical way to test the accuracy of the LD values, we carried out the following test: Any change in the limb darkening

values would mostly change the amplitude of the two features centered around the mid-transit point, either by increasing or decreasing it. Therefore, we ran our whole fitting algorithm two more times, arbitrarily increasing this amplitude by 50% and decreasing it by the same amount with respect to its original shape. After computing the excess depths in the exact same fashion as explained in this work but with the LD model component changed, we observed no significant difference between different results when 1σ errors are being considered. Thus, the precision of our data does not allow for a limb darkening fitting.

2.4.2 Exoplanetary sodium line

Similar to (Albrecht, 2008) and (Zhou & Bayliss, 2012), our data clearly show a reduction of the exo-atmospheric absorption in the middle of the transit which is caused by the radial velocity shifts of the planetary sodium signal inside the broad stellar sodium line. We use this effect to model the sodium D-lines in the atmosphere of HD 189733b. According to our model parameters, we estimated the planetary sodium line depth, A_{Na}, and a measurement of the line width, σ_{Na}. Our best-fit values, along with 1σ errors, are summarized in the last two columns of Table 3.3 for both planetary sodium D_1 and D_2 lines in the three integration bands. We find the values of the line depth and line width for the two narrower passbands to be consistent with each other within the given errors. Obviously this should be the case, since the shape of the planetary signal moving inside the stellar sodium line should be independent of the choice of passband. However, amplitudes and depths at 3 Å are slightly below the error bars of the other two passbands. As we mentioned before (in Section 2.3.1), with this dataset at 3 Å the quality of the data is insufficient most probably due to the flare and short cadence of the data. In here, that must be the reason for very large error bars and underestimated planetary signal. Therefore, when calculating the average of the σ_{Na} and A_{Na}, we exclude the results of the 3 Å data. The average line depth and width are $\bar{\sigma}_{Na} \simeq (0.098 \pm 0.026)$ Å and $\bar{A} \simeq 0.023 \pm 0.007$. We also estimated the equivalent width to be the product of the averaged line depth and the averaged line width, which is $\sim (0.0023 \pm 0.001)$ Å .

In principle, the width of the line potentially contains the information on the line broadening sources (e.g., pressure broadening, rotational broadening, winds). However, here σ_{Na} and A_{Na} are degenerate and therefore we cannot robustly interpret the physical conditions of the atmosphere directly from them. It is only the product of these two values that indicates a physical meaning from equivalent width of the exoplanetary sodium that blocks the star. We note that in principle it is possible to break this degeneracy by comparing the sodium line profile to the profile obtained from the complete transmission spectrum. The complete spectrum can be obtained from the division of in-transit spectra by the out-of-transit spectra, similar to the methods of Wyttenbach et al. (2015) and Redfield et al. (2008). However, we did not use that method because

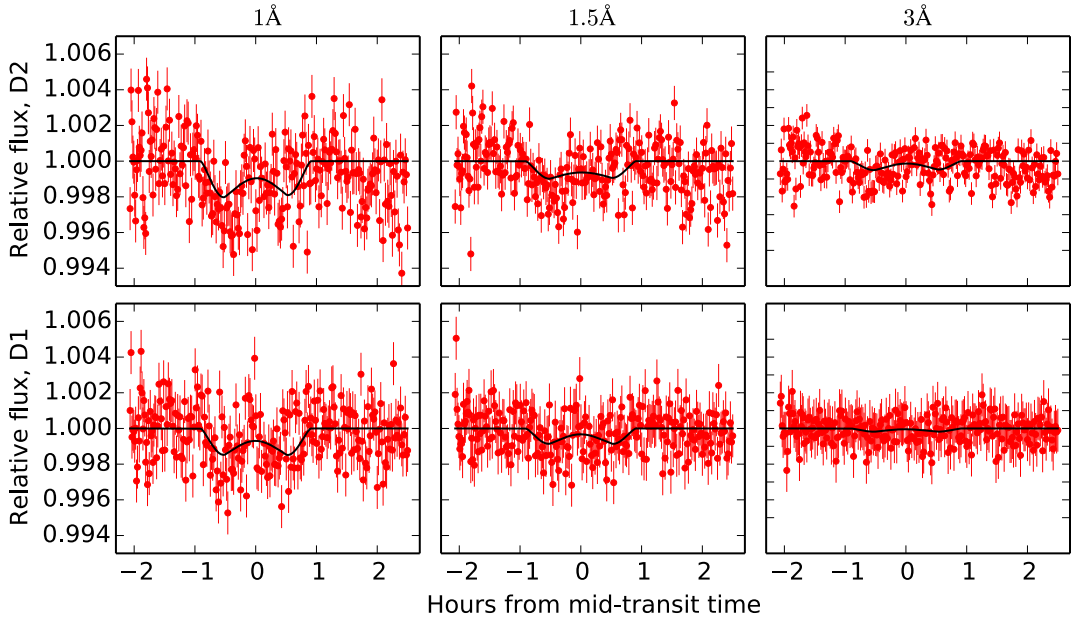

FIGURE 2.7: The excess light curves in three integration passbands for both sodium D_1 and D_2 after correcting for the flare and differential limb-darkening components.

of very high intrinsic variability and activity of this star, especially during the time of this observation, which prevented us from achieving the required alignment between the spectra. In [the] upcoming [chapter], we will investigate this further by analyzing a planet orbiting a less active star.

2.4.3 Excess light-curve depths

For a better visualization of the outcome, in Figure 2.7 we show all of the excess light curves after removing the flare and differential limb-darkening components. The only model plotted over the data in this figure is the planetary RV model component. In our models, we did not use any transit light-curve model directly and so the amount of the additional depth that has been added to the light curve here can be achieved by measuring the equivalent width of the exoplanetary sodium line. The additional excess to the light curve is then the equivalent width divided by the integrated flux of each passband divided by the reference band level. Table 2.4 shows the values of the excess light curves for the three integration bands (1 Å, 1.5 Å, and, 3Å) as the average of sodium D_2 and D_1 lines. As expected, these light curves show that the depth of the excess light curve increases with the decrease of the width of the integration passband. This is due to a higher contribution of the star in the wider passbands compared to that of the planet.

In all cases the derived excess depth obtained from the Na D_2 line for a given integration band is deeper than the one obtained from the Na D_1 line. This has also been found in Huitson et al. (2012). One possible scenario is explained by looking at

TABLE 2.4: Computed values for the relative absorption depth in [%] of the light curve.

Stellar line	Excess depth
1Å	
Average(D_1, D_2)	0.72 ± 0.25
1.5Å	
Average(D_1, D_2)	0.34 ± 0.11
3Å	
Average(D_1, D_2)	0.20 ± 0.07

the strength of the absorption signal, which is proportional to the contrast between the stellar sodium line and the planetary sodium line. In the case of Na D_2 the stellar line is deeper and therefore the contrast is smaller. Thus, the signal in Na D_2 appears larger than the transmission signal in Na D_1.

2.4.4 Potassium and neutral calcium lines

Potassium and calcium are also among the alkali metals. After sodium, for the computed effective temperature of HD 189733b, models of exoplanet atmospheres predict potassium as a prominent absorption feature (Seager & Sasselov, 2000; Fortney et al., 2010). To investigate the presence of these alkali metals in the HD 189733b atmosphere, we apply the same method to study the potassium line at 7699 Å and a pronounced neutral calcium line at 6122.22 Å. However, we were not able to detect any signature of exoplanetary potassium and calcium in their excess light curves within their noise. We attribute this to the quality of the data rather than to the chemical composition of the exoplanet atmosphere: The computed standard deviation of our potassium excess light curve is 1.2 ppt, while the amplitude of potassium derived from models is predicted to be 0.24 ppt (Pont et al., 2013). Therefore, our data are not precise enough to produce reliable results around these wavelengths. For the calcium excess light curve, the standard deviation of the excess light curve is 1.0 ppt. Although the data is slightly more accurate, in agreement with Pont et al. (2013) we did not detect any calcium absorption. This could probably mean that the quality of the data in both observations are not sufficient to detect the neutral calcium. An alternative explanation could be that the calcium abundance is not in the limit of detection.

2.4.5 Comparison with previous work

Previous measurements of the excess absorption of the sodium in HD 189733b for passbands between 1 and 80 Å, along with our results, are shown in Figure 2.8. Bibliographic values are taken from Wyttenbach et al. (2015), Huitson et al. (2012), Redfield et al. (2008), Jensen et al. (2011), and Cauley et al. (2016). Huitson et al. (2012) used low-resolution spectra of STIS/HST and obtained the excess depths for wide ranges of

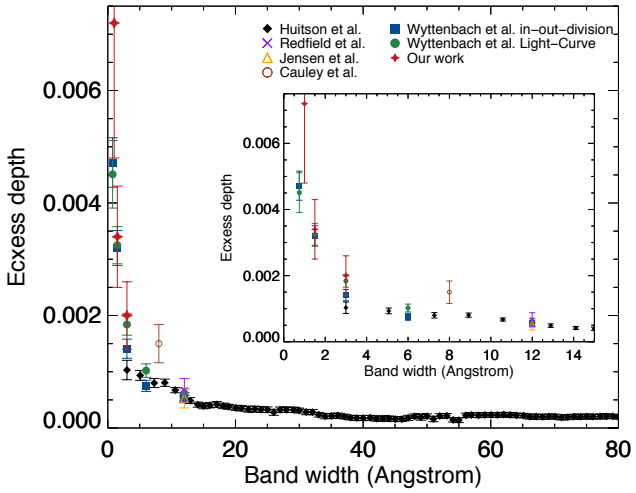

FIGURE 2.8: Our averaged excess depths for each integration band centered at the sodium lines (red filled stars) compared to previous works.

integration bands from 3 to 80 Å around the sodium feature (black filled diamonds). Wyttenbach et al. (2015) used high-resolution data obtained with HARPS and performed ground-based transmission spectroscopy using integration bands of 0.75, 1.5, 3, 6, and 12 Å. They used two approaches: One by fitting a transit model on the excess light curve (green filled circles) and the other by investigating the residuals of the in-transit divided by the out-of-transit spectra (in-out division; blue filled squares). Redfield et al. (2008) and Jensen et al. (2011) both used the same set of data taken by the high-resolution spectrograph mounted at the Hobby Eberly Telescope (HET) and tried to detect the exo-atmosphere by applying the in-out division approach (yellow unfilled triangle and purple cross). Finally, using the same approach, Cauley et al. (2016) analyzed a single transit observation of HiRES on Keck (unfilled brown circle). In our work we introduced a new approach for an accurate measurement of the exoplanetary transmission signal. Compared to previous measurements this approach is unbiased by stellar differential limb-darkening effect, stellar flaring activity, and the changing RV bump. Our estimated values of the additional absorption by the exoplanetary atmospheric sodium are indicated by the red filled stars in Figure 2.8. In comparison to other studies, our data points show stronger absorption with larger error bars. The main reason for this difference must be the correction of the bulgy shape in the middle of the transit excess light curve caused by differential limb-darkening and changing radial velocity effects. In other words, not considering an increase in flux near the mid-transit time would underestimate the absorption depth, thus producing smaller values. The error bars in our work are larger by about a factor of 3. This is reasonable since our model has more components and therefore consists of fewer degrees of freedom.

The differential limb-darkening model calculations performed in this work can be compared with those computed by Czesla et al. (2015). The purpose of this [chapter] is

to consider the line cores to actually search for the planet signatures. Therefore, the cores of the lines are investigated, where the effects of the flare and the planets are present. Czesla et al. (2015) only considered the wings of the sodium lines where the effects of stellar activity and the planet are not present (or only marginally). Furthermore, we use ratios rather than differences, but as shown in Czesla et al., this is a small effect for small-amplitude variability (Eq. 7 in Czesla et al. 2015). Moreover, Czesla et al. (2015) use Kurucz models, while we use PHOENIX angle resolved synthetic spectra. A difference between PHOENIX and Kurucz is that the former is calculated in spherical symmetry, the latter in plane parallel, which is justified because the atmosphere in main sequence stars is thin and the curvature does not play a role. However, getting the LD correct for our needed order of precision, the plane parallel geometry is probably insufficient. In this respect, the phoenix model is considered to be better.

2.4.6 Rough estimation of Na number density in the HD 189733b atmosphere

Stellar abundances can be obtained from equivalent widths (EWs) of spectral lines, using a relation called the "curve of growth". For small equivalent widths (i.e., weak lines) the equivalent width of a line is proportional to its number density. In this work we computed the equivalent width of HD 189733b as the product between the line depth and the line width, $\ln(\mathrm{EW}) = \ln(\mathrm{A_{Na}}\times\mathrm{FWHM}) = \ln(\mathrm{A_{Na}}\times 2\sqrt{2ln(2)}\ \sigma_{\mathrm{Na}})$ = -5.02, corresponding as expected to the weak line regime. Assuming a scale height of 100 km above the clouds, the number density of sodium in the atmosphere of HD 189733b is 10^4 atoms/cm^3, close to the value that Heng et al. (2015) estimated.

2.4.7 Further considerations in the model budget

Despite carrying out a meticulous analysis of the model components in this work, there are other aspects that might have a second-order impact on our data. For example, stellar spots and stellar rotation are two physical effects that deform the stellar spectral line shape and, therefore, might influence the derived excess light curves. In this work these effects were ignored for the two reasons. First, with respect to stellar rotation, HD 189733 is a slow rotating star (Winn et al., 2007, ∼12 days) and since the exposures are equally distributed along the transit this effect, if any, should be averaged out in our all-transit integrations (Dravins et al., 2015; Wyttenbach et al., 2015). Second, to measure the influence of occulted and unocculted stellar spots, in addition to the rotational period and amplitude of the modulation of the total stellar flux (which would give us an idea of the spot coverage at the moment of the observations) we would have needed simultaneous broad-band observations (Pont et al., 2013; McCullough et al., 2014). Indeed, the use of simultaneous observations with low-resolution instruments is

a good way to detect spot crossing events. A question that we will be able to answer with new high-resolution observations simultaneous to broad-band data is whether the change in excess depth observed in this work could have been created by unaccounted spot signal. With only the present data set we cannot assess this.

2.5 Conclusions

We used high-resolution spectra of UVES to measure the sodium absorption in the transmission spectrum of the hot-Jupiter HD 189733b. In this work we applied a new approach based on the changing radial velocity of the exoplanet. To this end, we analyzed six excess light curves in sodium D_1 and D_2 that were integrated in three different bands. We modeled a combination of three main effects on each data set and extracted some information about the exo-atmospheric sodium. These effects are a stellar flare starting close to mid-transit time, the differential limb-darkening effects, and the planetary sodium line profile that is moving inside the stellar sodium line because of the change in the radial velocity of its orbit.

We confirm the ground-based detection of sodium in the upper atmosphere of HD-189733b. Close to the mid-transit time a bump appears in the excess light curves, which is caused by the radial velocity changes of the planet while moving in its orbit with respect to its parent star. By modeling this effect we estimate the equivalent width of the exoplanetary sodium line by an estimation of its width and depth. In the future, with the improvement in the quality of observations, this might be used to better constrain the physical conditions in the upper atmosphere of exoplanets as part of the atmospheric models. The average equivalent width of the two sodium lines is 0.0023 ± 0.0010 Å. The average depth of the excess light curve is 0.72 ± 0.25 % at 1 Å, 0.34 ± 0.11 % at 1.5 Å, and 0.20 ± 0.06 % at 3 Å, in good agreement with previous research.

Finally, in this work we learn the following. First, in high-resolution transmission spectroscopy at any wavelength, Ca H & K or H_α should be always observed simultaneously when monitoring flaring activity consistency. Second, depending on some parameters, such as the temperature of the star, the width of the stellar sodium line, and the orbital velocity of the planet, the bump that appears in the mid-point of the excess light curves can originate from changing radial velocity effects and/or from the differential limb-darkening effect. A careful treatment of these two factors must be carried out. Finally, in an observation with short cadence and a large number of data points, the radial velocity bump can be better studied.

Acknowledgements: S. Khalafinejad acknowledges funding by the DFG in the framework of RTG 1351 and thanks I. Snellen, S. Albrecht, and the anonymous referee for their suggestions and advice. Accomplishment of this work was obtained through assistance, advice, and scientific discussions with many other people, especially at Hamburg Observatory and Center for Astrophysics (CfA). S.

Khalafinejad would like to specifically thank M. Holman, S. Czesla, M. Güdel, B. Fuhrmeister, A. K. Dupree, M. Payne, H. Müller, P. Ioannidis, and M. Salz for their valuable support and assistance. C. von Essen acknowledges funding for the Stellar Astrophysics Centre provided by The Danish National Research Foundation (grant No. DNRF106). T. Klocová acknowledges support from RTG 1351 and DFG project CZ 222/1-1.

[Appendix figure:]

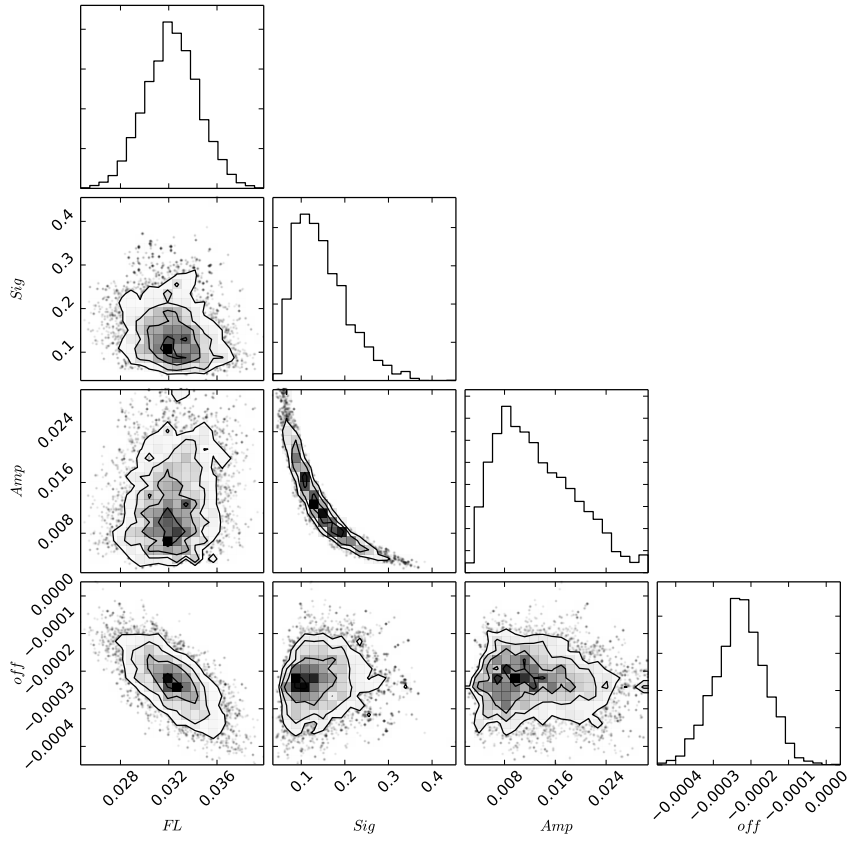

FIGURE A.1: Posterior distributions of the model parameters fitted in this work in the shape of histograms, along with their correlation plots. Values are computed from the 1.5 Å excess light curve around the sodium D_2 line. Here **FL** is the flare scaling parameter, **Sig** is width of the exoplanetary Gaussian profile, **Amp** is the amplitude of the exoplanetary Gaussian profile, and **off** is the normalization constant for the flare model.

2.6 Supplementary sections

The contents of this section are not a part of the published manuscript in A&A journal. I add this section as a complement in this thesis.

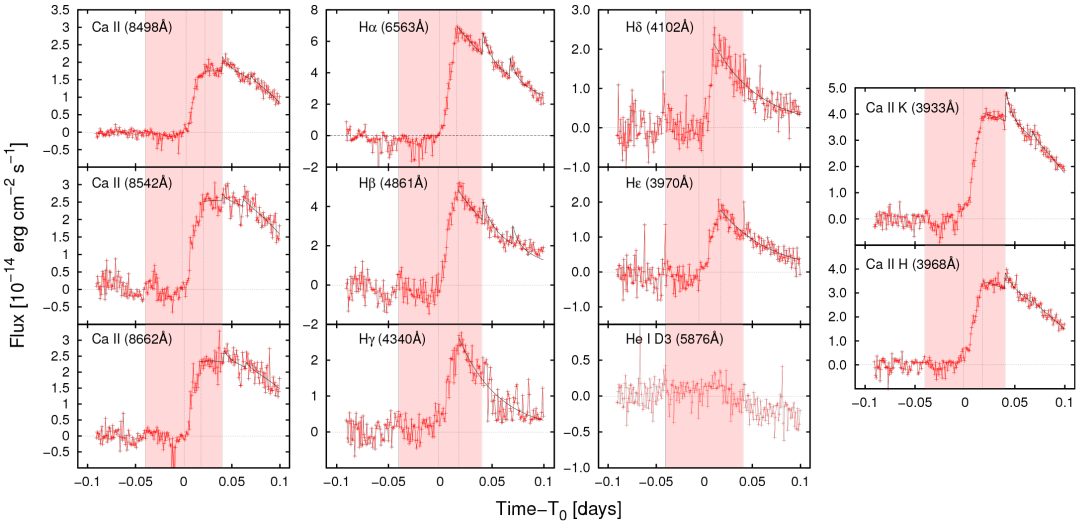

FIGURE 2.9: Evolution of a flare in HD 189733 obtained through temporal evolution of activity indicating lines. Red data points are the measured flux values with their corresponding 1σ error, solid black line is the best fit of the flare decay phase, Dashed vertical black lines represent the beggining and peak of the flare in each spectral line. Horizental dashed line mark a quiscent zero level and the pink shaded area shows the duration of the transit (taken from Klocova et al., 2017).

2.6.1 Observed flare in HD 189733b

In the manuscript by Klocova et al. (2017), we extensively investigated the flaring event in HD 189733, during the transit. In this study, these authors obtained the temporal evolution of the core of several chromospheric optical spectral lines, namely, Ca II H & K lines (3933, 3968 Å), H_α (6563 Å), H_β (4861 Å), H_γ (4341 Å), H_δ(4102 Å), H_ϵ (3970 Å), Ca II infrared triplet (8498 Å , 8542 Å , 8662 Å) and He I D3 (5875.6 Å), which are depicted in Figure 2.9. As the figure shows, almost all of lines show a similar behaviour and as already extensively discussed in Section 2.3.2.1, the flare could have similarly affected the core of the Na I D-lines, hence it needs careful consideration in the analysis of the exoplanetary atmospheres. In this work, these authors estimate the total energy release of the star in the studied optical chromospheric lines (except He I D3) to be $\sim 7.8 \times 10^{31}$ erg, which place the observed flare in the range of moderate stellar flares observed in K- and M-type stars.

2.6.2 Transmission spectrum: Division of in-transit by the out-of-transit spectra:

To see the contribution of the additional absorption of the exoplanetary atmosphere directly in the high-resolution spectra and obtain the transmission spectrum in a wavelength region around the sodium lines, one approach is to divide the an average of in-transit spectra by an average of the out-of-transit spectra (see Chapter 3). However, using our data set of HD 189733, dividing the in-transit spectra by the out-of-transit

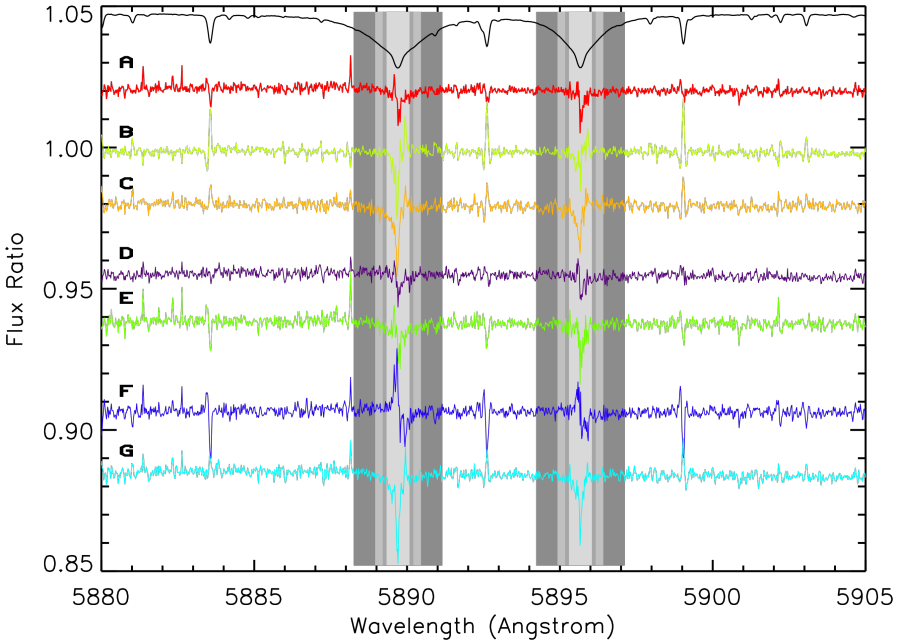

FIGURE 2.10: Residuals of different combinations of in-transit by the out-of-transit spectra. For clarity, all profiles are given an offset from value 1. The spectrum at the top shows a scaled stellar spectrum. **A:** Average of all in-transit by all of the out-of-transit spectra. **B:** Average of the out-transit before ingress (out_1) by the average out-transit after egress (out_2). **C:** Average of the first half of the in-transit (in_1) by the average of the second half of the in-transit spectra (in_2). **D:** Division of in_2 by out_2. **E:** Division of in_1 by out_1. **F:** Division of in_2 by out_1. **G:** Division of in_1 by out_2. The shaded gray ares show passbands of 0.75, 1, 1.5 and 3 Å.

spectra is biased by the high level of intrinsic stellar variability (stellar flare). Thus we cannot make a robust conclusion with this method. Nevertheless, we quickly tested this approach on our data and the results are shown in Figure 2.10. In this figure, we show the division of different combinations of in-transit by the out-of-transit spectra, as well as divisions of the first half of the in- or out-transit data by their second half (in_1/in_2 or out_1/out_2). These divisions should in principle result in no signal, hence it is a good way to test the method. Here we briefly discuss residuals of the division: In most of the residuals a deep-spike pattern can be seen, even in division of out_1 by out_2, which we expect it to be a flat residual with the value of 1. The dark green profile (E) which is the division of the in_1 by out_1, both taken before the flare, can be the right answer, however this requires further detailed analysis, i.e., consideration of the exoplanetary changing radial velocity effect, differential limb-darkening, etc. The development of the framework for the use of this approach is completed in Chapter 3 of this thesis.

2.6.3 Statistical requirement: MCMC analysis

In this section I briefly introduce the MCMC method, which is partly based on a lecture given by Prof. David Kipping at Sagan Workshop 2016[1]. This online lecture is very

[1] http://nexsci.caltech.edu/workshop/2016/agenda.shtml

useful for learning the principles of MCMC principles, particularly regarding applications on exoplanetary data analysis. I narrow-down the explanations to the requirements of my analysis.

Having a set of observations, we often need to fit a model with adjustable parameters to the data. Best-fit parameters are frequently defined as those quantities which results in minimum difference between the model and the data. The problem here is that the data is never exact and is associated with error (or noise). Thus the fit is never perfect. We need to evaluate the goodness of a fit and to know the uncertainties on the values of the best-fit parameters (William H. Press, 2002). The Markov chain Monte Carlo method is a useful statistical tool to study the uncertainty on the parameters.

A Markov chian is a sequence of random variables, having the following property: Given the present state of the system, the probability of moving into any particular new state dependents only on the current state and is independent of the past history. The MCMC method is based on Bayes' theorem (see equation 2.10), which describes the probability of a proposition, based on prior knowledge of conditions related to it and actual data. Sampling the posterior distributions of possible values of each parameter is the heart of the MCMC method which is based on Monte Carlo approximation and a random walk algorithm. Each guess about the fitting parameters is made considering the previous choice of parameters. The sequence of guessed values that bring us closer to the real values, make a chain and allows to obtain the posterior probabilities, which are the main outcome of the MCMC procedure. In the following we first introduce the posterior probability distribution and then then we discuss the sampling from this distribution based on construction of a Markov chain.

Posterior probability distribution:

Briefly, for the case of an exoplanetary transit, *given a set of observational data such as photometric transit light curve, the MCMC procedure allows us to study the posterior probability distributions of the light curve model parameters.* The following equation describes the posterior probability, which is the joint probability distribution of some parameter of interest (θ), conditioned upon some data ($\mathcal{D}$) and a model ($\mathcal{M}$).

$$P(\theta|\mathcal{D},\mathcal{M}) = \frac{P(\mathcal{D}|\theta,\mathcal{M})P(\theta|\mathcal{M})}{P(\mathcal{D}|\mathcal{M})} \tag{2.10}$$

In this equation,
$P(\theta|\mathcal{D},\mathcal{M})$ is the posterior probability ($\mathcal{P}$),
$P(\mathcal{D}|\theta,\mathcal{M})$ is the likelihood function ($\mathcal{L}$),
$P(\theta|\mathcal{M})$ is the prior (Π), and
$P(\mathcal{D}|\mathcal{M})$ is a normalization factor, known as evidence ($\mathcal{Z}$), or the marginal likelihood of the data.

Assuming normally distributed un-correlated noise (white noise), the likelihood function had the following form:

$$\mathcal{L} = \prod_{i=1}^{N} \frac{\exp(-\frac{1}{2}\frac{r_i^2}{\sigma_i 2})}{(2\pi)^{\frac{1}{2}}\sigma_i} \tag{2.11}$$

where, N is the number of data points, r_i is the residuals obtained after subtraction of the model from the data, and σ_i is the measurement uncertainty. Thus,

$$\log \mathcal{L} = c - \frac{1}{2}\chi^2 \tag{2.12}$$

where, c is a constant resulted from the constant terms in equation 2.11 and chi-square (χ^2) is $\sum_{i=1}^{N} \left(\frac{r_i}{\sigma_i}\right)^2$.

The prior is the probability distribution that express knowledge about the values of the fitting parameters before the data is taken into account. There are different types of priors: For instance, *informative* priors which are created from the available information form the past or *un-informative* priors which are created to reflect a balance among outcomes when no information is available. Setting physical lower and upper boundaries is an example of uniform, uninformative priors that we used in our analysis.

Sampling from the probability distribution:

A MCMC algorithm samples from the probability distribution based on the construction of a Markov chain. After a number of steps, the status of the chain is used as a sample of the distribution and the quality of the sample improves by increasing the number of steps.

Assume two parameters a and b as the components of θ and define a likelihood function as well as priors. Figure 2.11 shows the parameter space of this example. In the parameter space, only one point represents the true values of the parameters, however we can only reach a certain area around that point. In the figure this area is the green circle (high-$\mathcal{P}$, high-$\mathcal{L}$, low-χ^2 region). For the sampling, the calculation of the posterior ($\mathcal{P}$) can start from a random point in the parameter space and, based on a random walk algorithm, sample the region of high posterior probability. Different sampling algorithms can be applied for rejecting or accepting a random move in the states of the Markov chain. One of the samplers is the Metropolis (Metropolis et al., 1953), that we explain here as an example.

The Metropolis rule states,

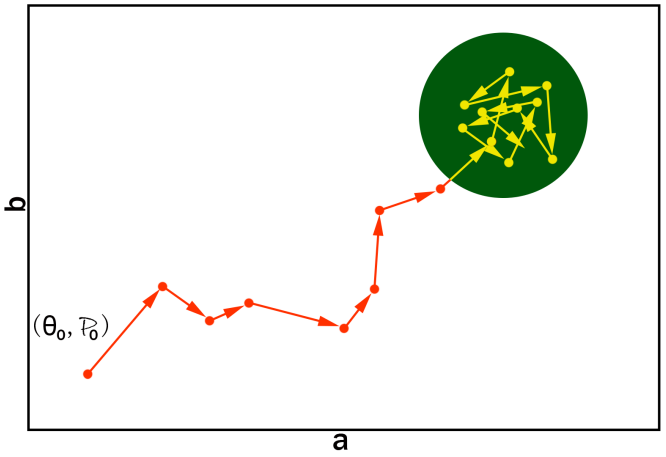

FIGURE 2.11: The sampling. The region with higher posterior probability is shown in green. The sampling of posterior probabilities starts from a random point and jumps to a trial point. The successful jumps create the Markov chain. Burn-in steps are shown in red.

if $\mathcal{P}_{trial} > \mathcal{P}_i$,

accept the jump, so

$\theta_{i+1} = \theta_{trial}$

if $\mathcal{P}_{trial} < \mathcal{P}_i$,

accept the jump with probability: $\frac{\mathcal{P}_{trial}}{\mathcal{P}_i}$

where i is the step number, $\mathcal{P}_i$ is the posterior probability of an accepted step and $\mathcal{P}_{trial}$ is the posterior probability at the new proposal step of the Marchov chain. The last line of the algorithm ($\frac{\mathcal{P}_{trial}}{\mathcal{P}_i}$), shows that the normalization factor introduced in Equation 2.10 cancels out, hence does not play a role in the sampling. Through this algorithm we reach the true answer within a certain error-bar. The successful jumps from a chain, are called Markov Chain. The steps that are taken before reaching the green zone, are known as the *burn-in* stage, which are usually excluded from the sampling in order to increase the precision.

Other sampling algorithms such as Metropolis-Hastings algorithm (Metropolis et al., 1953; Hastings, 1970) and affine-invariant sampling (e.g., Goodman & Weare, 2010) are also based on this algorithm. The emcee package (Foreman-Mackey et al., 2013), that we used in our analysis, uses an affine-invariant sampler. The difference is that instead of updating only one set of model parameters, it updates an ensemble of parameters at each step.

Chapter 3

The atmosphere of WASP-17b

Narrow-band transmission spectroscopy is a method for understanding the chemical and physical properties of upper exoplanetary atmospheres. Due to large absorption cross-sections, resonance lines of atomic sodium D-lines (at 5889.95 Å and 5895.92 Å) produce larger transmission signals compared to other species. Our aim is to unveil the physical properties of WASP-17b through an accurate measurement of the sodium absorption in the transmission spectrum. We analyze 37 high-resolution spectra observed during a single transit of WASP-17b with the MIKE instrument on the 6.5 meter Magellan Telescopes. To check the occurrence of stellar flaring activity, we measure the temporal variations of H_α and Ca II Infrared Triplet (IRT) lines. Then we obtain the excess absorption light curves in wavelength bands of 0.75, 1, 1.5 and 3 Å around the center of each sodium line (i.e., the light curve approach). We model the effects of differential limb-darkening, and changing planetary radial velocity on the light curves. We also analyze the sodium absorption directly in the transmission spectrum, which is obtained through dividing in-transit by out-of-transit spectra (i.e., the division approach). We then compare our measurements with a radiative transfer atmospheric model. We detect no considerable stellar flaring activity on this F-type star. Our analysis result in a tentative detection of exoplanetary sodium: We measure the width and amplitude of the exoplanetary sodium feature to be $\sigma_{\rm Na} = (0.128 \pm 0.078)$ Å and $A_{\rm Na} = (1.7 \pm 0.9)\%$ in the excess light curve approach and $\sigma_{\rm Na} = (0.85 \pm 0.034)$ Å and $A_{\rm Na} = (1.3 \pm 0.6)\%$ in the division approach. By comparing our measurements with a simple atmospheric model, we retrieve an atmospheric temperature of $1550\ ^{+170}_{-200}$ K and radius (at 0.1 bar) of $(1.81 \pm 0.02)\ R_{\rm Jup}$ for WASP-17b.

S. Khalafinejad, M. Salz, P. Cubillos, et al.
submitted to A&A

3.1 Introduction

Transmission spectroscopy, pioneered by Charbonneau et al. (2002), is a very successful observational method to unveil the chemical and physical properties of hot-Jupiter atmospheres. During an exoplanetary transit, a fraction of the stellar light passes through the planet's atmosphere, hence a fraction of this light is absorbed. As a result, signatures of the chemical compositions of the atmosphere will be imprinted on the transmitted light at certain wavelengths, making the radius of the exoplanet to appear larger at these wavelengths.

In the optical region the resonant doublets of sodium (Na) and potassium (K), are predicted to have larger absorption cross sections, hence, a larger absorption in the transmitted signal of these lines are expected (Seager & Sasselov, 2000; Fortney et al., 2010). Thus, these lines have been used as diagnosis of the exoplanetary atmospheres (e.g., Vidal-Madjar et al., 2011; Huitson et al., 2012; Sing et al., 2012; Wyttenbach et al., 2017). In addition, at optical wavelengths it is possible to infer, for instance, water vapor (Allart et al., 2017) and atmospheric hazes (Pont et al., 2008; Sing et al., 2016) and molecular features of TiO (e.g., Hoeijmakers et al., 2015; Sedaghati et al., 2017).

Different types of instruments unveil different aspects of an exoplanetary atmosphere. For instance, using low-resolution transmission spectroscopy, we can investigate hazes, clouds, Na, and K, in the deeper layers of exoplanetary atmospheres. On the other hand, by means of high-resolution narrow-band transmission spectroscopy in the Na doublet region, we can access the information on upper atmospheric layers and the layers above the hazes and clouds (Kempton et al., 2014; Morley et al., 2015).

Exoplanetary transit spectral observations are influenced by different effects, mostly of stellar origins. These can be flares, spots, differential limb-darkening and rotation effects. A successful detection of the exoplanet's atmosphere requires a proper consideration of these effects. We already investigated sodium in HD 189733b as a prototypical target: HD 189733A is a very active K-type star. After correcting for stellar flaring activity and stellar differential limb-darkening effects, we could detect the signatures of sodium in the exoplanet (Khalafinejad et al., 2017). Here, we intend to apply a similar approach on transit observations of WASP-17b, a hot-Jupiter orbiting an inactive F-type star. Obtaining a comparative view of different targets helps to better understand the influence of stellar activity of different stellar type in transmission spectroscopy and better introduce the modest conditions and requirements for an exoplanetary atmospheric detection through a single transit observation.

In this study, we use the high-resolution spectral data of Zhou & Bayliss (2012), who used a single transit observation of WASP-17b and claimed the detection of sodium by obtaining the excess light curve depth in passbands of 1.2 Å to 1.8 Å (with steps of

0.1 Å) around the center of sodium lines and measured the depths by fitting a simple light curve model. We analyze the sodium absorption in WASP-17b with a new approach, and we intend to improve and complete the previous analysis by Zhou & Bayliss (2012): We rely on their extraction of the raw excess light curve and go beyond their work, first by accounting for the stellar limb-darkening effect and changes in the radial velocity of the planet in the excess light curves. The second additional consideration is that, in addition to the detection of Na, we constrain the physical characteristics of WASP-17b by modelling the sodium transmission spectrum of the planet. Finally, we additionally investigate the behaviour of the H_α and Ca II infra-red triplet (IRT) lines during the transit to inspect the stellar activity and possibly the exoplanet's atmospheric hydrogen absorption from the upper atmosphere of this highly inflated (Anderson et al., 2010) exoplanet.

The structure of this [chapter] is as follows: In section 3.2, we introduce the hot-Jupiter WASP-17b. Then in Section 3.3 we describe the observation, and the steps of data reduction. In Section 3.4, we investigate the stellar activity through H_α and Ca II IRT. Section 3.5 focuses on detection of exoplanetary atmospheric sodium using the excess light curves, and Section 3.6 presents the method and results for extraction of the transmission spectrum at the region of sodium lines. In Section 3.7 we discuss the results and compare the observations with an atmospheric model. Finally in Section 3.8 we summarize our conclusions. [In section 3.9 we compare the results of WASP-17b to HD 189733b.]

3.2 The system WASP-17

WASP-17b is an inflated hot-Jupiter, with a mass of 0.49 M_{Jup}, a radius of 1.99 R_{Jup} and an orbital period of ∼3.7 days (Anderson et al., 2010) and it is in a retrograde motion (Triaud et al., 2010; Bayliss et al., 2010). Its host star is of spectral type F6V, with a magnitude of V = 11.6 (Høg et al., 2000). The parameters of the system used in this work are summarized in Table 2.1. WASP-17b has a very low density, $\sim 0.06\rho_{Jup}$, and a high equilibrium temperature, ∼1800 K (Anderson et al., 2011). Thus, it is expected to have a very large atmospheric scale height. In consequence, this hot-Jupiter has become one of the few very well studied targets for atmospheric characterization with transmission spectroscopy. For instance, Wood et al. (2011) used medium-resolution ($\mathcal{R} = \frac{\lambda}{\Delta\lambda} \sim 12,500$) observations with the GIRAFFE fiber-fed spectrograph on the VLT and reported a sodium detection with an excess absorption of (1.46 ± 0.17)%, (0.55 ± 0.13)% and (0.49± 0.09)% in passbands of 0.75 Å , 1.5 Å and 3 Å , respectively. Zhou & Bayliss (2012) used the Magellan Inamori Kyocera Echelle (MIKE) spectrograph

($\mathcal{R} \sim 48,000$) on the Magellan Telescopes for the same purpose. By applying the narrow-band transmission spectroscopy technique they detected a $(0.58 \pm 0.13)\%$ signal at the core of sodium D-lines (D_2 at 5889.95 Å and D_1 at 5895.92 Å) in a passband of 1.5 Å.

Later, low-resolution broad-band observations in the optical and IR region were performed. Bento et al. (2014) used multi-color broad-band photometry with SDSS 'u','g','r' filters (covering wavelengths from 325 to 690 nm) and found a tentative evidence of higher planetary radius in the r-band, consistent with sodium absorption feature. Using the Hubble Space Telescope (HST) WFC3 instrument, Mandell et al. (2013) analyzed low-resolution transmission spectroscopy in the IR region (1.1 -1.7 μm). Their analysis of the band-integrated time series suggests water absorption and the presence of haze in the atmosphere of WASP-17b. Nortmann et al. (2015) used FORS2 at the VLT, and after dealing with instrumental systematics, derived the optical transmission spectrum of WASP-17b in the region between 800 and 1000 nm. Their transmission spectrum hints at a strong absorber in the bluer wavelength region. In addition, based on their tested theoretical models, tentative signatures of a TiO and VO or a potassium and water atmosphere have been observed, but these models cannot fully explain their observations. Sing et al. (2016) used HST (STIS and WFC3) and Spitzer observations, and obtained a full optical to mid-IR transmission spectrum ($\sim 0.3\mu$m - 5μm) of a sample of hot-Jupiters including WASP-17b. The atmospheric absorption at ~5900 Å(wavelength of sodium) in WASP-17b is the highest of all the other hot-Jupiters in the sample and it is about 4 times larger in WASP-17b compared to HD 189733b. Sedaghati et al. (2016) analyzed low-resolution ($\mathcal{R} \sim 2,000$) transit observations of FORS2 and obtained the broad-band transmission spectrum of WASP-17b with a bin size of 100 Å in the wavelength range of 5700 to 8000 Å, where they detected a cloud-free atmosphere and potassium absorption with a 3σ confidence level. Heng (2016)'s work also suggested a nearly cloud-free atmosphere at visible wavelengths.

3.3 Observations and data reduction

On the night of 2010 May 11, one single transit of the hot-Jupiter, WASP-17b, was observed with the MIKE spectrograph, mounted on the 6.5m Magellan II (Clay) Telescope. During the observation 37 spectra, with an exposure time of 600 seconds each, were obtained. In addition, slit widths of 0.35 arcsec was chosen, resulting in a spectral resolution of $\mathcal{R} \sim 48,000$ in the wavelength range of 5000 to 9500 Å. The spectra have a pixel scale of ~ 0.04 Å and a resolution element of about 0.12 Å. In the sodium doublet region, the S/N of our spectra is about 80 per pixel. Two of the spectra with poor signal-to-noise (S/N < 60) and high airmass were discarded. These correspond to the first and last exposures. The details of the observations, along with the initial data reduction of the echelle spectra, are fully discussed by Bayliss et al. (2010).

Parameter	Symbol	Value
Mid-transit time	T_0 ($\mathrm{HJD_{UTC}}$)	2454577.85806 ± 0.00027
Orbital Period	P (days)	3.7354380 ± 0.0000068
Transit duration	T_{14} (days)	0.1830 ± 0.0017
Ingress/egress duration	T_{12} =$\mathrm{T_{34}}$ (days)	0.0247 ± 0.0017
Orbital inclination	i (°)	86.83 ± 0.62
Semi-major axis	a (au)	0.05150 ± 0.00034
Planet mass	M_p ($\mathrm{M_{Jup}}$)	0.486 ± 0.032
Planet radius	R_p ($\mathrm{R_{Jup}}$)	1.991 ± 0.081
Planet surface gravity	log g_P (cgs)	2.448 ± 0.042
Stellar effective temperature	T_eff (K)	6650 ± 80
Stellar surface gravity	log g (dex)	4.161 ± 0.026
Metallicity	[Fe/H]	-0.19 ± 0.09
Stellar radius	R_S ($R_\odot$)	1.572 ± 0.056
Projected stellar rotation velocity	$v\sin(i)$ ($\mathrm{kms^{-1}}$)	10.05 ± 0.88
Planet to star area ratio	$(R_\mathrm{P}/R_\mathrm{S})^2$	0.01696 ± 0.00026

TABLE 3.1: Adopted values for the orbital and physical parameters of WASP-17 used in this work. For consistency, all values are taken from Anderson et al. (2011).

3.3.1 Spectral data reduction in Na, H_α and Ca II IRT

The spectra were analyzed in wavelength bands with a width of a few hundred Angstroms in three regions: Na (5800-6100 Å), H_α (6500-6700 Å), and Ca II IRT (8400-8700 Å). Data preparation before performing the main analysis mainly consists of spectral normalization, spectral alignment and telluric line removal. The data reduction in the Na doublet, H_α and Ca II IRT regions follows a similar procedure. For the spectral normalization and removal of telluric features in the Na region we rely on the data reduction by Zhou & Bayliss (2012). Here we accurately align the spectra in the Na wavelength region, in addition we perform a complete reduction around the H_α and Ca II IRT lines.

We shift the spectra into the stellar rest frame. To correct the misalignment between exposures, we select 8,7, and 14 stellar spectral lines in the vicinity of the Na doublets, H_α, and Ca II IRT lines respectively and fit Gaussians to determine the line centers. Each spectrum is shifted by the mean offset of the line centers with reference to the first observation. The resulting misalignments in each region are shown as radial-velocity (RV) shifts in Fig. 3.1 (top). All regions show a similar pattern, with maximum difference of $\sim$1 $\mathrm{km\,s^{-1}}$ between exposures. We then correct cosmics via linear interpolation over the affected spectral ranges and interpolate all spectra onto a common wavelength grid, increasing the sampling by a factor of four to minimize interpolation errors. 5th-order polynomials are used to normalize the continuum.

The airmass value of each exposure is also shown in Figure 3.1 (bottom). Changes of airmass cause variations in the telluric features (mainly water at these wavelengths) with a similar trend. To remove the tellurics in the sodium region, the method by Zhou & Bayliss (2012) is followed: The observations of the rapidly rotating B star, HD 129116,

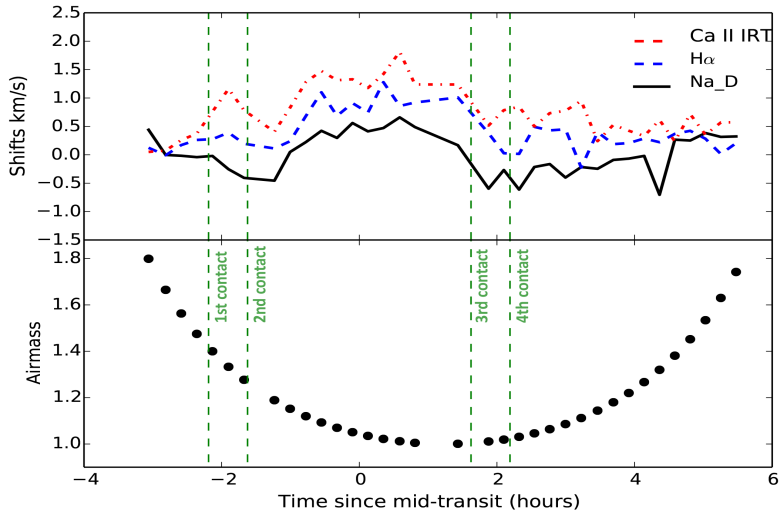

FIGURE 3.1: Top: Spectral misalignments in three regions around the Na doublet, Hα and Ca II IRT line. The vertical dashed lines show the times of the transit contacts. **Bottom:** Airmass value for each exposure (two of the exposures with airmass larger than 1.8 are not shown).

are used as a template. For each exposure, this telluric template is scaled to fit the prominent telluric water lines and then the spectra are divided by the template. As explained in Zhou & Bayliss (2012), no telluric sodium is observed. The spectra of WASP-17 are affected by interstellar sodium lines which has wavelength shifts of about 1 Å with respect to the stellar lines.

The removal of the Earth's atmospheric features in the Hα and Ca II IRT regions is a bit different. Telluric lines are stronger in the Hα range and we devise an approximate approach to remove them. A high resolution telluric transmission spectrum of Moehler et al. (2014) for an airmass of 1.5 is fitted to the average stellar spectrum. This fitting procedure has three free parameters: The stellar radial velocity, the amplitude of the telluric lines, and the width of a Gaussian with which the telluric spectrum is convolved to model the instrumental resolution. In a second step, the observation run is split into five sections and for each of the five mean spectra, we again fit the telluric spectrum by only adjusting the amplitude of the telluric lines. During the observation night, this amplitude follows a trend that resembles the airmass trend, and we fit a 2nd order polynomial to the amplitude evolution. Each spectrum is then divided by the shifted and convolved telluric reference spectrum with the amplitude derived from the polynomial. In the individual spectra, strong telluric lines are effectively reduced at the 90% level. Figure 3.2 shows the average spectrum of WASP-17 in the H_α and Ca II IRT regions with the telluric transmission spectrum and the uncorrected spectrum for the Hα range. The telluric correction has little impact on the resulting Hα equivalent widths (see Section 3.4.1).

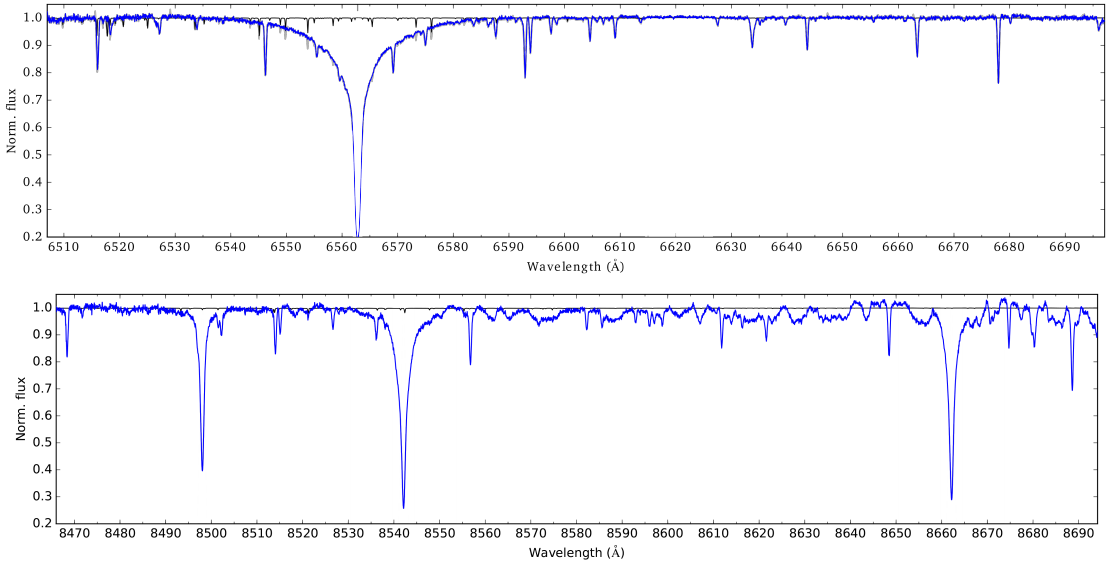

FIGURE 3.2: Average Hα and Ca II IRT spectra (blue). Black lines show a telluric transmission spectrum used for the telluric correction in the Hα region. The uncorrected spectrum is shown in gray in the Hα panel.

3.4 Data analysis: stellar activity

Using high-resolution transit spectra, we have two possible approaches to detect the exoplanetary sodium embedded inside the stellar spectrum: One is to integrate in narrow passbands inside the stellar absorption lines (with a reference band in the continuum) and investigate the additional contribution of the planetary atmosphere to the obscuring of the stellar light during the transit (excess light curve approach). The other is to directly obtain the exoplanetary transmission spectrum by dividing the in-transit spectra by the out-of-transit spectra (division approach).
In this section we investigate the stellar activity and then, in the next sections, we perform the narrow-band transmission spectroscopy both through excess light curve and division approaches.

3.4.1 Investigations of stellar activity

Stellar spots (e.g., Oshagh et al., 2013; Czesla et al., 2009), plage regions (e.g., Oshagh et al., 2014) and flaring activity (e.g., Klocova et al., 2017), are the main sources of false signals in the interpretation of transmission spectra.

Small bumps or dips in the photometric transit light curves and deformations of the high-resolution spectral lines shapes can be signatures of stellar variability caused by spots and flares. Investigations of spots with this method are easier for the case of very fast rotating stars (e.g., Wolter et al., 2005; Reiners, 2012). In this work, we do not have any simultaneous photometric observations and the star is a slow rotator, however we are still able to perform an in-depth study of flaring events.

Chromospheric lines such as H_α (at 6563 Å) and Ca II IRT (at 8498, 8542, 8662 Å) are indicators of stellar activity (e.g., Cincunegui et al., 2007; Martínez-Arnáiz et al., 2010; Chmielewski, 2000; Andretta et al., 2005; Busà et al., 2007; Klocova et al., 2017), but also other stellar lines such as the sodium D-lines can be affected by stellar activity (e.g., Cessateur et al., 2010). We must assure that the photospheric and the chromospheric lines in the optical region are not affected by the stellar activity during our observation.

Additionally, the H_α line can indicate signatures of hydrogen escape from the upper atmosphere of hot gas planets (Cauley et al., 2016, 2017a). Due to its low mean density and a high irradiation level, WASP-17 b is expected to host a strongly evaporating atmosphere (Bourrier et al., 2015; Salz et al., 2016). Therefore, it is reasonable to search for Hα absorption features around the planetary transit.

We compute the equivalent width (EW) of the individual "transmission" spectra in the H_α and all three Ca II IRT lines following Cauley et al. (2017a). Each spectrum is divided by the total mean spectrum and then integrated over the central $\pm$75 km s^{-1}. The EW of the IRT lines is then averaged. Errors are derived from the variation in adjacent +/-500 to 1000 km s^{-1} bands, which underestimates the error of introduced by our analysis, for example by the continuum normalization. Therefore, we follow Czesla et al. (2017) to derive a mean error for the EW curves and scale our values accordingly.

The time evolution of the equivalent widths is shown in Figure 3.3. Both EWs behave similarly: except for the planetary egress, WASP-17 shows a slightly increased activity level during the planetary transit compared to the out-of-transit level. At egress both EW show a dip, which can be caused by stellar variability or by some absorption feature of planetary origin. However, the signal-to-noise is not sufficient to investigate this any further. With a variation of 20 mÅ, the H_α EW of WASP-17 over the transit observations varies slightly stronger than that of HD 189733 (see Cauley et al., 2017a). We exclude a planetary H_α absorption feature with an EW of 20 mÅ, which is equivalent to 1.5% absorption over the integration band. For IRT we exlude 8 mÅ corresponding to 0.3% absorption. WASP-17 is among several other systems with non-detections of H_α absorption (HD 149026, HD 147506, KELT-3 b, and GJ 436 b Jensen et al. 2012; Cauley et al. 2017b). HD 189733 remains the only system with possible H_α absorption caused by the planets evaporating atmosphere (Jensen et al., 2012; Cauley et al., 2017a).

The activity evolution is not caused by tellurics, because both EW show the same behavior, while the H_α region has been corrected for tellurics. Therefore, the activity evolution is genuine and can be used as comparison for the sodium analysis. In the study of Klocova et al. (2017) a moderate flare on the K-type host star HD 189733 affected the IRT EW by about 5 mA (see their Fig. 6). The corresponding time evolution showed a clear flare evolution in the IRT lines and the H_α line. Khalafinejad et al. (2017) showed that the sodium lines were affected by the same flare, but on a much weaker level. The time evolution in all studied lines in that flare was similar. Our data

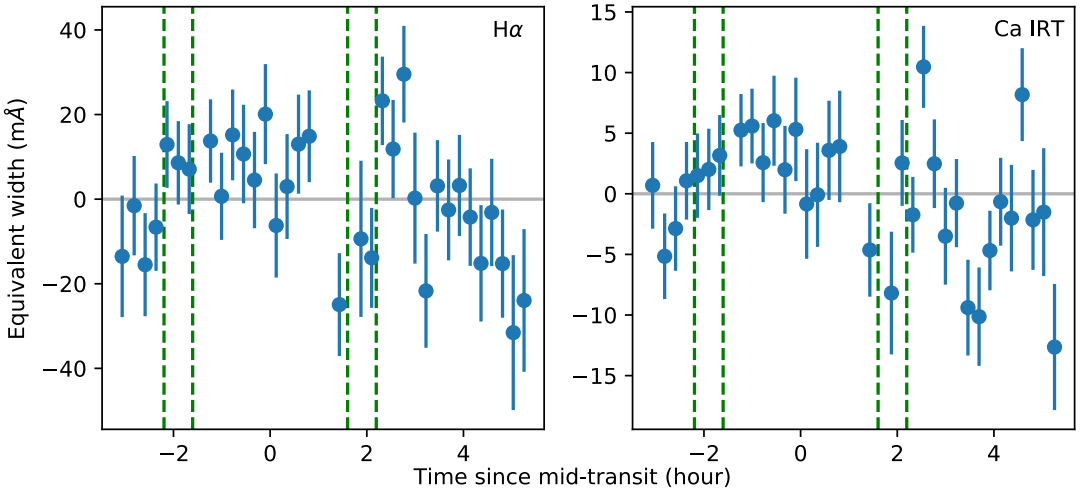

FIGURE 3.3: Time evolution of the equivalent widths of the H_α line and the mean of three Ca II IRT lines. The contact points of the transit are indicated by vertical dashed green lines. The horizontal dashed line shows the reference value of zero. Both lines show some activity evolution over the night, but no stellar flares.

excludes a strong stellar flare. Comparing the time evolution of the acitivity indicators with the sodium excess light curve shows no correlation. Thus, we conclude that the chromospheric activity has not affected the photospheric neutral sodium lines.

3.5 Analysis and results: Excess light curve approach

3.5.1 Extraction and modelling of the excess light curve

The extraction of the raw excess light curves in the sodium doublet region is performed by Zhou & Bayliss (2012), who use integration passbands of 0.75, 1, 1.5 and 3 Å centered on the core of each sodium line and select the interstellar sodium next to D1 (Na line with the longer wavelength) as a reference in the flux integration. For consistency with Zhou & Bayliss (2012), we use the same integration and reference bands. During the transit the radial velocity of the planet changes between -18 to $+18$ kms^{-1}, which results in a Doppler shift of up to $\pm$ 0.35 Å. Thus, with a passband of 0.75 Å we can still be sure that the exoplanetary feature is still located inside the integration band. Here we use a different approach in measuring the exoplanetary signal in the excess light curves. In the analysis of Zhou & Bayliss (2012) the stellar activity, stellar differential limb-darkening (LD) and the changing RV of the exoplanet during transit were not taken into account. In this analysis, we first investigate the stellar flaring activity to make sure that the sodium lines are not affected by chromospheric activity, and then we make a combined model of differential LD and changing RV models to fit the excess light curves; the detailed explanations of these two model components are presented by Khalafinejad

λ-range (Å)	D2:	5888.52-5889.27	5888.40-5889.40	5888.15-5889.65	5887.40-5890.40	5895.50-5898.00
	D1:	5894.48-5895.23	5894.36-5895.36	5894.11-5895.61	5893.36-5896.36	
Average		0.75 Å core	1 Å core	1.5 Å core	3 Å core	ref.
u_1,u_2		0.3651 , 0.1447	0.3850, 0.1589	0.3965 , 0.1802	0.3979 , 0.2144	0.4009 , 0.2306

TABLE 3.2: Limb-darkening coefficients (u_1,u_2) for the average of sodium D_2 and D_1 integration bands (Core) and reference (Ref.) bands with the specified wavelength ranges in the table below.Errors of the limb-darkening coefficients are not shown to avoid visual contamination, but are in all cases on the order of 10^{-3}-10^{-4}.

et al. 2017. To increase the signal-to-noise we use average of both sodium D-lines and do not treat the lines individually.

There are some effects that inevitably influence transit spectra or excess light curves. To accurately model the excess light curves, we take the following effects in to account and consider each as a model component of the final model, which is introduced in Section 3.5.1.4.

3.5.1.1 Differential Limb-darkening (component A)

Stellar limb-darkening depends on wavelength (e.g., Czesla et al., 2015). Thus dividing the flux in the integration band by the reference band, is similar to dividing two light curves with two different limb-darkening coefficients by each other. Thus, this division affects the shape of the excess light curve and needs to be corrected for, specifically in the late type stars where the effect is more prominent. We calculate the limb-darkening coefficients in each passband using the intensity profiles of the PHOENIX model (Hauschildt & Baron, 1999; Husser et al., 2013) and the quadratic limb-darkening law (Kopal, 1950). More details are explained by Khalafinejad et al. (2017); the results are shown in Table 3.2. Since the excess light curves are already averaged out between D1 and D2, we use the average of the coefficients. The signal-to-noise of our data is not enough to consider LD coefficients as fitting parameters, hence this model is considered to be constant and to have no fitting parameters.

3.5.1.2 The changing planetary radial velocity (component B)

The exoplanetary spectral lines move inside the stellar lines due to the Doppler shift caused by the exoplanetary orbital motion. This results in an apparent reduction of the depth of excess light curve at the mid-transit time (Khalafinejad et al., 2017; Albrecht, 2008).

For considering the exoplanetary atmospheric absorption effect in this work, the exoplanetary sodium line is considered as a Gaussian convolved inside the stellar sodium line. This Gaussian moves inside the stellar sodium line with an offset proportional to the change of the radial velocity of the exoplanet by the orbital motion (see equation 8 in Khalafinejad et al., 2017). At the same time, the moving Gaussian causes the dip

in the light curve and a bump near the mid-transit time. The fitting parameters of this components are the width (Gaussian σ_{Na}) and the depth (Gaussian A_{Na}) of the exoplanetary Gaussian profile. Since our raw excess light-curve is the average of both sodium D1 and D2, we model the effect on both stellar sodium lines and then obtain the averages of sigma and amplitude of the Gaussian feature.

3.5.1.3 Neglected Effects

According to Triaud et al. (2010) and Bayliss et al. (2010), WASP-17 has a large spin-orbit misalignment angle ($\sim 150°$), and the Rossiter-McLaughlin (RM) effect does not produce a symmetric RV curve. Therefore, the variations in line shape during the transit do not completely cancel out. Based on Figure 6 in Anderson et al. (2010), the difference between the amplitude of the curve in the blue- and red-shifted parts of the star is about 100 ms^{-1}, which results in a 0.002 Å change of a spectral line position. This value is at least one order of magnitude smaller than what we expect for the width of the exoplanetary sodium feature. Thus we ignore the RM effect in this analysis. We note that we evaluate the influence of the RM effect on measurements of the line centers in the alignment of spectra in Section 3.6.1. However, the maximum radial velocity caused by the RM effect is smaller than the precision of the alignment, thus no evidence of influence of this effect could be detected.

In addition, as mentioned in Section 3.4.1, we cannot take into account the effects of possible spots and plages in this data set. Thus they are neglected considering that photospheric activities in F-type stars are not pronounced.

3.5.1.4 Final model

A combination of the LD and the RV models constitutes the main model, we also consider a normalization constant (offset) as the third model component (C) and consider the model, M, as a function of time, t:

$$\begin{aligned} M(t) &= LD(t) \times RV(t) + offset \\ &\equiv A \times B + C \end{aligned} \tag{3.1}$$

The fitting parameters in this model are the σ_{Na}, A_{Na} and the offset. For exploring the best-fit parameters and their associated uncertainties we apply a Markov Chain Monte Carlo (MCMC) analysis, using the affine invariant ensemble sampler *emcee* (Foreman-Mackey et al., 2013). We employ 20 walkers, with 100 chains each, where the initial positions are synthesized from a Gaussian distribution around our best estimates. All the free parameters have uniform priors imposed. For σ_{Na} and A_{Na} we set a lower bound of 0 and upper bound of 0.3. We allow a burn-in phase of $\sim 50\%$ of the

Passband	$\sigma_{\rm Na}$ (Å)	$A_{\rm Na}$	offset
0.75Å	0.128 ± 0.078	0.017 ± 0.009	0.007 ± 0.001
1Å	0.054 ± 0.040	0.034 ± 0.025	0.005 ± 0.001
1.5Å	0.077 ± 0.074	0.031 ± 0.029	0.002 ± 0.001
3Å	0.036 ± 0.061	0.054 ± 0.067	0.001 ± 0.001

TABLE 3.3: Best-fit values for the model parameters obtained from the Na D_1 and Na D_2 excess light curves in the three integration bands. As a reminder, here $\boldsymbol{\sigma_{\rm Na}}$ is width of the exoplanetary Gaussian profile, $\mathbf{A_{Na}}$ is the amplitude of the exoplanetary Gaussian profile, and **offset** is the normalization constant.

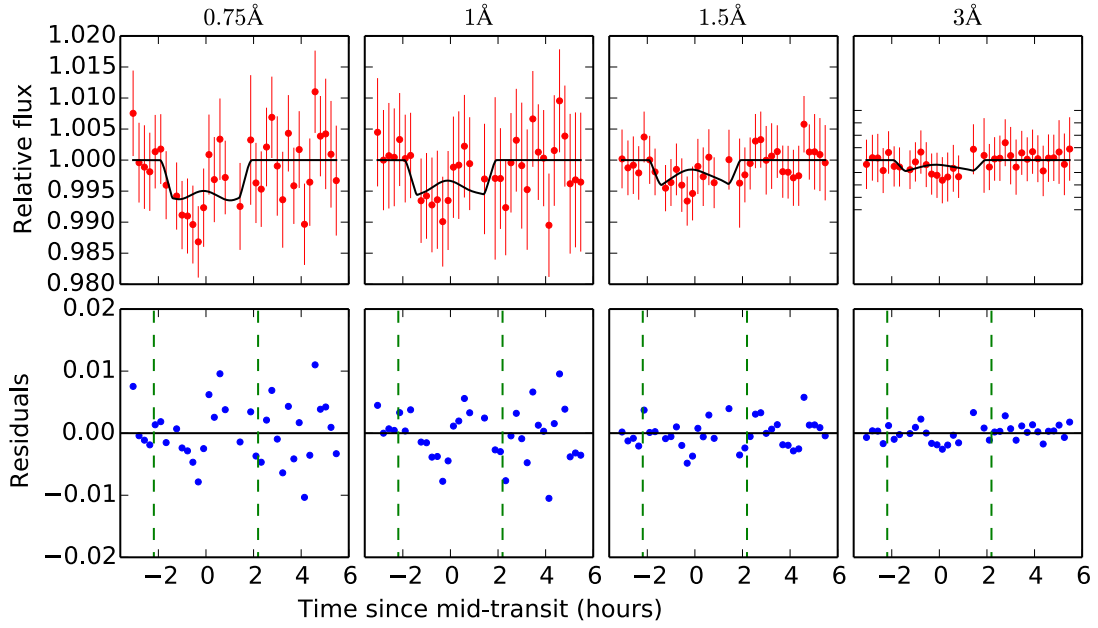

FIGURE 3.4: **Top panels:** Best-fit models plotted over the raw excess light-curves for four passbands. **Bottom panels:** The residuals for each passband. The vertical dashed lines show the times of the transit contacts.

total chain length, beyond which the MCMC is converged. The posterior probability distribution is then calculated from the latter 50% of the chain (see Section 3.5.2 for the results).

3.5.2 Best-fit parameters and uncertainties of the excess light curve models

The best-fit model of each excess light curves are shown in the top panels of Figure 3.4 and the values of the parameters as well as their uncertainties are provided in Table 3.3. The posterior distributions of the fitting parameters and the correlation plots are shown in Figure 3.5 for the 1.5 Å excess light curve. The bottom panels in Figure 3.4 show residuals after subtracting the data from the model. The excess light curves have a large noise level and thus the atmospheric absorption measurements have large uncertainties (see Table 3.3). As Table 3.3 shows, the significance of the signal is about

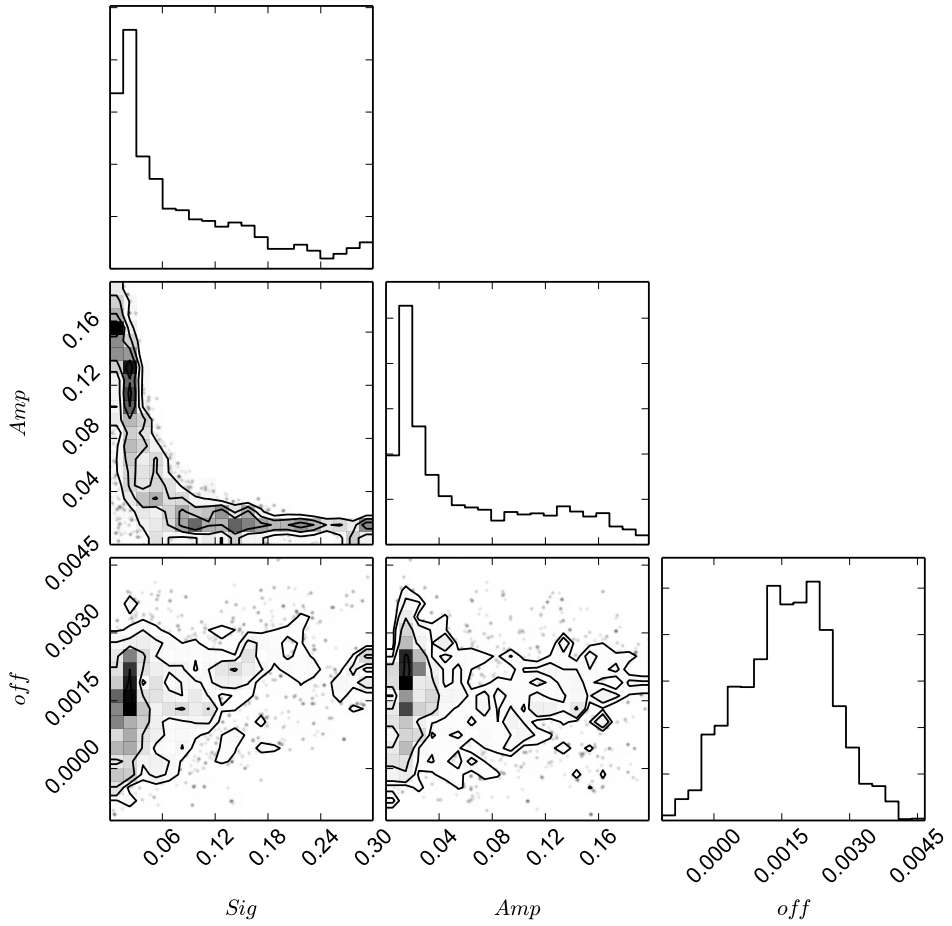

FIGURE 3.5: Posterior distributions of the model parameters fitted in this work in the shape of histograms, along with their correlation plots, for the passband of 1.5 Å.

2σ in our narrowest integration band and the significance level reduces by the increase of the passband. At 1.5 Å there is hardly a signal and the 3 Å passband results in a null outcome. At narrower passbands the contrast between the planetary and stellar flux contributions is smaller, thus a larger signal is expected. The measured exoplanetary signal with this approach is compared with planetary atmospheric models in Section 3.7.3.2.

3.6 Analysis and results: Division approach

3.6.1 Extraction of the exoplanetry spectrum through the division approach

In transmission spectroscopy we compare the spectra taken when the exoplanet is outside the transit with those taken during the transit. Only the in-transit data contain the planet's atmospheric signatures, hence subtracting the out-of-transit spectrum from

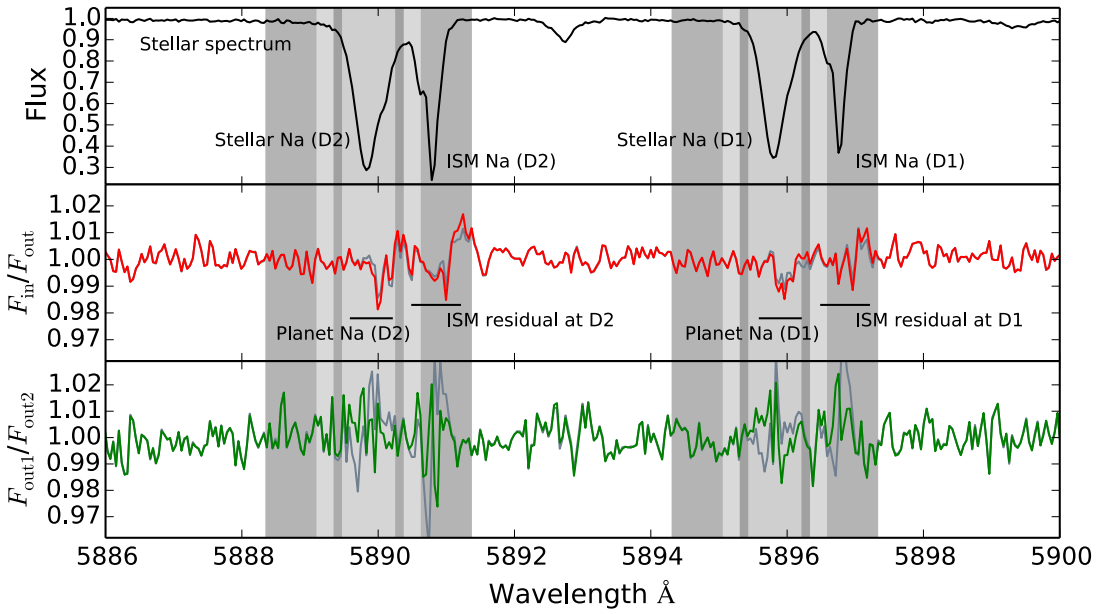

FIGURE 3.6: Transmission spectrum obtained by division approach. The black profile in the **first panel** is the stellar spectrum scaled to fit the plot. The red profile in the **second panel** is the division of the in-transit by the out-of-transit spectra, corrected for the exoplanetary RV shifts. The dark gray profile beneath the red profile is the division after applying the trial manual shifts. The dark gray profile in the third panel is the division of two sets of out of transit spectra by each other. The green profile is the same division shifted with respect to the other by 0.004 Å. Finally, the shaded regions, represent the integration bands at 0.75, 1, 1.5, and 3 Å.

them, can reveal the exoplanetary features within the residuals. The exoplanetary transmission spectrum is given by $(F_{\rm in} - F_{\rm out})/F_{\rm out}$. In this simple equation, the average of all in-transit spectra is considered as $F_{\rm in}$ (master-in) and average of all of out-of transit spectra is considered as $F_{\rm out}$ (master-out). However, this method has a problem: As mentioned before, due to orbital motion the exoplanetary RV changes, and this causes the shifts of the planetary sodium features relative to the stellar spectrum and hence the signal is diluted in the process of division. To overcome this problem, after telluric corrections and alignment of spectra, we divide each individual in-transit spectrum by the master-out spectrum. Then, to line up the exoplanetary features, we shift each residual based on the corresponding calculated radial velocity of the exoplanet in each exposure. We finally co-add all residuals (similar to Wyttenbach et al., 2015, 2017) and normalize the result with the same method explained in Section 3.3.1. We then consider the normalized residual as the transmission spectrum (see Section 3.6.2 and Figure 3.6 (middle panel). By this method we correct for the RV component in the division approach as well.

It is important to note that in narrow-band transmission spectroscopy accurate alignment of the spectra is a very important step of the analysis. In the division slight misalignments can cause systematic dips or spikes in the residuals. The precision of the

alignment depends on signal-to-noise and on the wavelength sampling (or the resolution) of spectra. Simulating the scatter and the wavelength sampling of our spectra on a Gaussian or Voigt distribution, we obtain an uncertainty of up to 0.004 Åfor the line position. This amount of mis-alignment can still be a source of variations in residuals at the location of strong lines compared to the noise level at the continuum. Dividing two sets of out-of-transit spectra by each other is a good approach to test the alignment and the robustness of the signals in transmission spectra. Hence, we also divide the average of out-of-transit spectra in exposures 1 to 4 (F_{out1}) before the ingress by the master-out spectra after the egress in exposures 30 to 34 (F_{out2}) by each other (see Section 3.6.2 and Figure 3.6 (bottom panel). These two sets of out-of-transit spectra have similar airmass, thus it can result in a second order correction of the tellurics. In addition, in the case of this target, we can use the interstellar sodium lines as a reference for evaluation of the alignment. The interstellar lines are constant and thus in the division are expected to result in values that are uniformly scattered around unity. Thus, if the initial alignment does not satisfy this condition, an additional shift can be applied to improve the alignment. In each single division stage in our analysis, we manually shift each in-transit spectrum with respect to the master-out, in a way to minimize the variations of the residuals at the position of interstellar lines. The amount of shifts we apply are between 0 and $\pm$ 0.004 Å (with the steps of 0.0005 Å) which is less than the precision of the initial alignment method. However, the final outcome with this method does not considerably alter the transmission spectrum and the residuals of the interstellar features do not reduce by the additional manual shifts. In Figure 3.6 the result of a set of manual shift trial on in-transit exposures are shown in gray beneath the red profile. In contrast, in the case of division of two sets of out-transit spectra, applying an additional shift of about 0.004 Å to one of the spectra, reduces the scatter of residuals. In Figure 3.6 (bottom panel), gray profile shows the initial division and green profile shows the division after applying the manual shifts.

We also need to think of any effect that causes a difference between the alignment of interstellar and the stellar lines. The RM effect is a possible source that affects the stellar lines but do not affect the interstellar lines. Based on the literature values of the orbital parameters (Anderson et al., 2011), we simulated a model of the RM effect in transit of WASP-17b and reduced it from the values of the spectral mis-alignment introduced in Section 3.3.1. The RM model is shown in Figure 3.7 on top of spectral shift values. The largest difference that the RM effect can cause is up to 0.003 Å which is again below the precision of the initial alignment with our method. The removal of the RM effect from the shifts does not considerably affect the residual outcome (similar to the manual shifts in the second panel). Hence we continue the work while ignoring this effect.

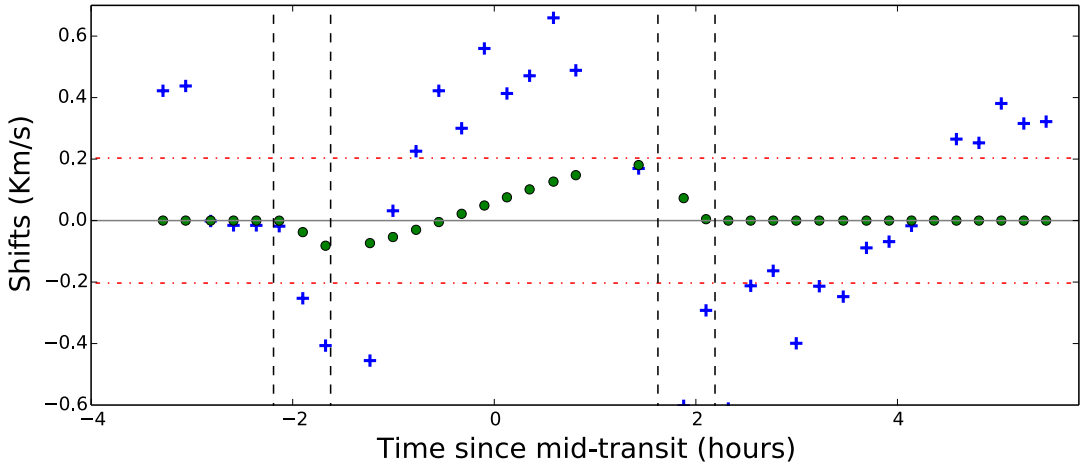

FIGURE 3.7: RM model vs. spectral mis-alignments of sodium region. Blue crosses, show the misalignment in the sodium lines region (already shown in Figure 3.1. Green field circles show the calculated RM effect. Red dash-dotted line shows the alignment precision of the data (± 0.004 Å). The significance of the RM effect is below the precision of the alignment. The vertical dashed lines show the times of the transit contacts.

3.6.2 Transmission spectrum of the division approach

Figure 3.6 summarizes the results of the division approach analysis. The master-out spectrum (or the stellar spectrum) is shown in the top panel, where the stellar and interstellar sodium lines can be clearly seen. The second panel shows the radial velocity corrected transmission spectrum of WASP-17b. The exoplanetary sodium absorption by D1 is visible at 5896 Å and the absorption at D2 is placed at 5890 Å. Fitting a Gaussian in each sodium feature in the transmission spectrum, yields $\overline{\sigma}_{\rm Na} = (0.085 \pm 0.034)$ Å and $\overline{A}_{\rm Na} = (1.3 \pm 0.6)\%$. The error of each Gaussian fit is estimated through a MCMC procedure, where the error bar on each residual data point is equal to standard deviation of continuum region in the residuals scaled by the stellar flux.

Another relatively large feature we see in the residuals (middle panel) is the scatter of data at the location of interstellar sodium lines. We note that the flux values at stellar and interstellar lines are low, thus the S/N of data at the core of these lines are lower compared to the continuum. Hence, larger scatter is inevitably present in the residuals at the location of these lines (further discussed in Section 3.6.3). The scatter at interstellar sodium lines is about 2σ and features at cores of stellar sodium lines are at the level of 3σ.

The division of two sets of out-of-transit spectra by each other are also shown as complementary and comparative information in the last panels of Figure 3.6. Naturally, we expect no feature at the sodium line positions in this profile. We see that the scatter of the points is relatively large at stellar and interstellar sodium line positions. However, the number out-of-transit exposures that build up this profile are less than the profile in the second panel by about a factor of 2 and, on average they are taken at larger airmass

and lower S/N compared to the exposures that build up the profile in the second panel. Hence, even in the continuum the scatter is larger compared to the second panel. Since the features in these residuals at any of the sodium lines sodium lines, do not exceed 3σ we consider the green profile as uniform scatter around unity.

Further discussion on evaluating the robustness of the exoplanetary absorption feature is in Section 3.7. Our observed transmission spectrum is then compared to a planetary atmospheric model in Section 3.7.3.1.

3.6.3 Residuals of the division

The residuals in Figure 3.6 (middle panel) shows relatively larger variations at the interstellar line positions. As discussed in Section 3.6.2 these features are related to the lower S/N at these lines. As can be seen in the top panel of the figure, the interstellar D_2 line has the largest depth among all four sodium lines; the feature of the residual related to this line is also more pronounced. However, other reasons such as mis-alignments smaller than 0.004 Å or changes of spectral line resolutions due to Earth's atmospheric effects can create such features. Looking at the un-binned residuals of Wyttenbach et al. (2017) for the case of WASP-49b, we see larger variations at the small interstellar sodium lines in their data as well. Compared to that work, interstellar lines in our case are stronger. In addition, MIKE is not as stable as HARPS and the resolution of our instrument is smaller by about a factor of two and thus the spectral alignment precision is less by about a factor of two. In any case, a complete removal of these features is not possible with this dataset and we continue the analysis assuming that features of residual at the position of the stellar sodium line are caused by the excess absorption of the exoplanetary atmosphere. The work-flow that we develop here can be applied quickly later to a new set of data.

3.7 Discussion

3.7.1 Excess light curve vs. division approach

In our light curve approach we did not directly measure any light curve depth. We have only estimated the shape of the exoplanetary sodium Gaussian. In the division approach we have obtained the transmission spectrum in the sodium region, where the shape of exoplanetary sodium line is directly visible.

Table 3.3, shows the values of widths and amplitudes of the fitted Gaussian at different passbands. The robustness of the measurements decreases with the increase of passbands, thus we consider the measurement at 0.75 Å as the best measurement. In Table 3.4 we compare the σ_{Na} and the A_{Na} of exoplanetary sodium Gaussian obtained

TABLE 3.4: sigma and amplitude of the exoplanetary Gaussian in light curve approach vs. sigma and amplitude in division approach

	σ_{Na} (Å)	A_{Na}
Light curve approach	0.128 ± 0.078	0.017 ± 0.009
Division approach	0.085 ± 0.034	0.013 ± 0.006

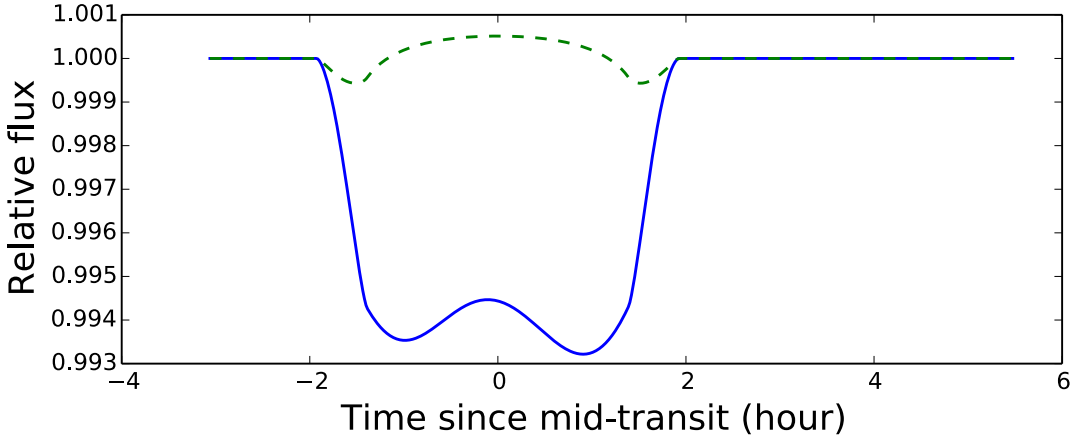

FIGURE 3.8: The differential limb-darkening model component (dashed curve) vs. the radial velocity model component (solid curve) for the integration passband of 0.75 Å.

in light curve approach, with those obtained in division approach. Within the error bars, the values are consistent with each other.

Our measured error bars on the exoplanetary feature are quite large. A comparison of the standard deviation of the data outside the transit with the expected signal at the sodium lines shows that the detection cannot reach confidence levels larger than 2σ and this represents the under-estimation of the error bars in previous analysis of the same data set.

We note that in the division approach we do not apply any differential limb-darkening correction on the spectra and their residuals directly. However, investigation of the model components in Figure 3.8 indicates that the LD model is about an order of magnitude smaller than the exoplanetary absorption effects in a F-type star. Thus the strength of this effect is already within the error bars and can be ignored in the division approach.

The results in the light curve approach show higher level of scatter and that is because we are using a small region of the spectrum (only the core and the reference bands) in this approach, while in the division approach the scatter is lower since for the determination of the error bars a larger region is considered.

TABLE 3.5: Estimated signal in per cent, for both light curve (LC) and Division (Div.) approaches, compared to the measurements by Zhou et al. (2012) and Wood et al. (2011).

Passband (Å)	0.75	1	1.5	3
Signal LC	0.74 ± 0.54	0.55 ± 0.43	0.40 ± 0.29	0.19 ± 0.15
Signal (Div.)	0.46 ± 0.29	0.34 ± 0.20	0.22 ± 0.12	0.12 ± 0.06
Zhou et al.			0.58 ± 0.13	
Wood et al.	1.46 ± 0.017		0.55 ± 0.13	0.49 ± 0.09

3.7.2 Comparison to previous measurements

3.7.2.1 Comparison of absorption signals

In order to be able to compare our measurements with other work, we average out the exoplanetary line flux in different passbands in both approaches. The results are shown in Table 3.5 and the values are compared to measurements by Zhou & Bayliss (2012) and Wood et al. (2011). The measurements are consistent with each other within the error bars. The source of the difference between the measurements must be in RV component correction and in the different approach in measurement of the signal. For example, Zhou & Bayliss (2012) measure directly the depth of the fitted light curve while we measure average of the flux in the fitted exoplanetary sodium line Gaussian. By looking at Figure 3.4 at 0.75 Å and roughly measuring the depth of the modeled light curve, we achieve a similar result to Zhou & Bayliss (2012).

3.7.2.2 Offset between the center of the stellar and planetary sodium lines

By looking at the sodium line center in the top and middle panel in Figure 3.6, we recognize an offset of $\sim$ 0.15 Å (7.5 kms^{-1}) between sodium residuals and the center of stellar sodium line. Wyttenbach et al. (2015) already interpreted a similar shift in HD 189733b as strong winds at the terminator. This can be a possible explanation in the case of WASP-17b as well, however, we must emphasize that the alignment of the exoplanetary features before co-adding the residuals is highly dependent on the accuracy and precision of the calculated radial velocities of the exoplanet relative to its host star. In calculation of the radial velocities, changing the values of orbital parameters, i.e., semi-major axis and period, even within their error bars affects this offset.

3.7.3 Atmospheric physical properties

3.7.3.1 Comparison to atmospheric models: Division approach

Here we describe a first approach at retrieving high-resolution transmission spectra of the sodium doublet lines. To model the WASP-17b high-resolution transmission spectrum and obtain a physical description of the data, we use the open-source Python Radiative

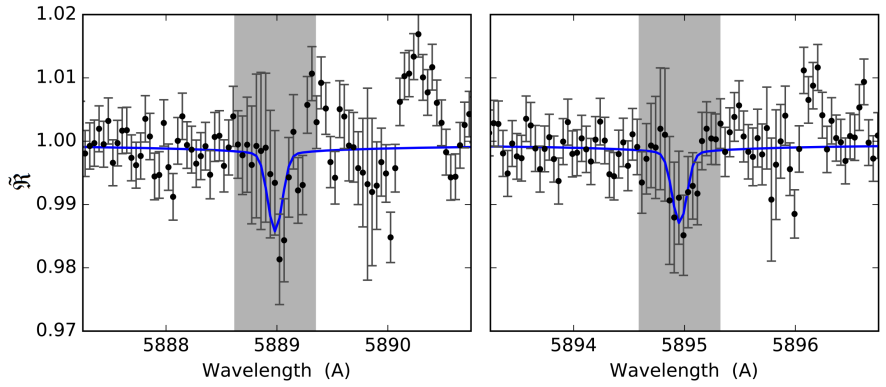

FIGURE 3.9: High-resolution spectrum (black points with 1σ error bars) and best-fitting model (solid blue line) around the sodium doublet lines. The shaded area denotes the wavelength region used to constrain the models.

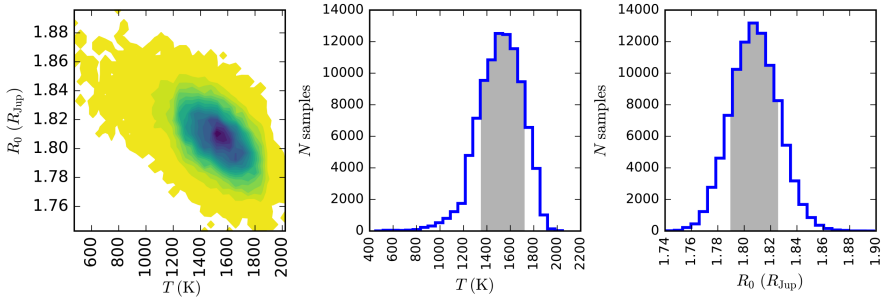

FIGURE 3.10: Pairwise (left) and marginal (middle and right) MCMC posterior distributions of the atmospheric temperature and the planetary radius at 0.1 bars. The shaded area in the marginal posterior histograms denote the 68% highest-probability-density region of the posteriors.

Transfer in a Bayesian framework (Pyrat Bay[1], Cubillos et al., in prep.), based on the Bayesian Atmospheric Radiative Transfer package (Blecic, 2016; Cubillos, 2016).

Due to the wavelength normalization (Section 3.6.1), high-resolution transmission spectra do not constrain the planet-to-star radius ratio (as is the case for lower-resolution transmission spectroscopy). For the narrow wavelength range covered by our observations, the spectra are dominated by the strong sodium doublet lines embedded into the Rayleigh absorption, which sets a continuum transmission level around the sodium lines. Thus, this data traces the differential transmission modulation of the sodium lines with respect to the Rayleigh continuum.

The Pyrat-Bay model initially computes the modulation spectrum or spectrum ratio (Brown, 2001),

$$M(\lambda) = \frac{f_{\rm in}(\lambda) - f_{\rm out}(\lambda)}{f_{\rm out}(\lambda)}, \tag{3.2}$$

[1] http://pcubillos.github.io/pyratbay

where $f_{\rm in}(\lambda)$ and $f_{\rm out}(\lambda)$ are the in- and out-of-transit flux spectrum, respectively. To replicate the wavelength normalization of the high-resolution data, the code calculates

$$\tilde{\Re} = \frac{1 - M(\lambda)}{1 - M(\lambda_{\rm ref})} = \frac{f_{\rm in}(\lambda)/f_{\rm in}(\lambda_{\rm ref})}{f_{\rm out}(\lambda)/f_{\rm out}(\lambda_{\rm ref})}, \tag{3.3}$$

where $\lambda_{\rm ref}$ is a wavelength far away from the sodium lines.

To produce the transmission spectra, the Pyrat-Bay code solves the radiative-transfer equation for a 1D atmospheric model consisting of spherically concentric layers, in hydrostatic equilibrium. For the WASP-17b data, we sample the atmosphere between 100 and 10^{-15} bar with 200 layers. Our forward model incorporates opacities for H_2 Rayleigh scattering (Lecavelier Des Etangs et al., 2008), and the sodium lines (Burrows et al., 2000). Other opacity sources like collision induced absorption do not play a significant role at the observed wavelengths. We also discard cloud opacities, based on previous transmission observations of this planet (Sing et al., 2016; Sedaghati et al., 2016).

For the retrieval we consider the simplified case of a solar-abundance atmosphere with thermochemical-equilibrium compositions (Blecic et al., 2016). Thus, we retrieve two atmospheric parameters, the atmospheric temperature (T, as an isothermal profile) and the radius of the planet (R_0) at a reference pressure $p_0 = 0.1$ bar (necessary to solve the differential hydrostatic equation).

To explore the parameter space, Pyrat-Bay uses the differential-evolution Markov-chain Monte Carlo (MCMC) algorithm (Cubillos et al., 2017), constrained by the high-resolution data in the region having a width of three times the half-width at half maximum, around each sodium line. We also fit the modulation (Eq. 3.2) to the optical broad-band transit depth 0.01524 ± 0.00027 (Sedaghati et al., 2016).

Figures 3.9 shows our atmospheric model over the high-resolution transmission data (residuals) and Figure 3.10 shows the bestfit model and the parameter posteriors, respectively. We retrieve an atmospheric temperature of $T = 1550^{+170}_{-200}$ K, which is consistent to 1σ with the planet's equilibrium temperature (1770 ± 35) K, and a reference radius of $R_0 = (1.81 \pm 0.02)\ R_{\rm Jup}$.

3.7.3.2 Comparison to atmospheric models: Excess light curve approach

The model that fits the residuals at the sodium lines in division approach, can be used for comparison to the excess light curve absorption signals. For this purpose after applying the instrumental broadening, we change the sampling of the models to match the sampling of the observations and then average out the model in different passbands the same way that we estimate the absorption signal in the observations. The result of this comparison is shown in Figure 3.11. As the figure shows the model and observed measurements match with each other. The χ^2 value of this comparison is ~ 0.5. We also compare the model with a constant line that has a value equal to the mean of the

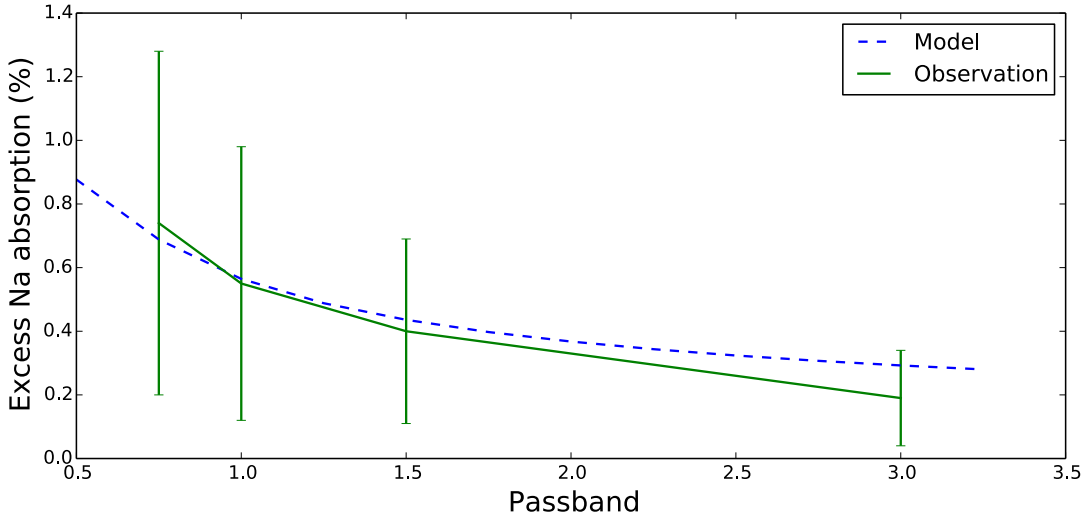

FIGURE 3.11: Atmospheric model vs. observation in the excess light curve approach. The dashed blue line is the result of averaging atmospheric model at the sodium absorption features in different passbands. The green data, attached to each other by the solid line, are the result of our excess light curve measurements in four different passbands.

observed data points. This comparison results in a χ^2 value of ~ 3.8. Due to large error bars non of the fits are statistically good. In addition, it is not practical to apply an independent atmospheric model fit to this approach, since the current model is already well within the large error bars.

3.8 Summary and conclusions

The aim of this work is the atmospheric characterization of the bloated hot-Jupiter, WASP-17b, using narrow-band transmission spectroscopy method at the sodium lines. We used 37 high-resolution spectra taken during a single transit of the target, using MIKE instrument on Magellan Telescopes. Our analysis consists of three main sections: (1) Investigation of the stellar activity through chromospheric lines of H_α and Ca II IRT, (2) investigation of the exoplanetry sodium absorption through the excess light curves in narrow pass-bands and (3) through the division of in-transit by the out-of-transit spectra.

We detect no strong chromospheric line absorption or any considerable stellar variability during the observations. In the excess light curves we detect tentative signatures of exoplanetary sodium with the Gaussian width of (0.128 ± 0.078) Å and Gaussian amplitude of $(1.7 \pm 0.9)\%$. Through the the division approach the measured Gaussian width and amplitudes are (0.085 ± 0.034) Å and $(1.3 \pm 0.6)\%$ respectively. Finally, in order to extract some of the physical properties we compare our results with the planetary atmospheric models. Our conclusions are listed below:

- Our re-analysis of this data set suggests an under-estimation of the uncertainties in the exoplanetary absorption signal measured by Zhou & Bayliss (2012).
- High-precision alignment (> 0.004 Å) and high signal-to-noise (> 100) of the spectra are crucial in achieving a robust ground-based transmission spectrum through a single transit observation.
- The division of two sets of out-of-transit spectra must be shown for better evaluation of the true exoplanetary signal in the division approach.
- Comparing our measurements with the Pyrat-Bay retrieval model, for WASP-17b we constrained an atmospheric temperature of 1550^{+170}_{-200} K, and a reference radius at 0.1 bar of (1.81 ± 0.02) $R_{\rm Jup}$
- During narrow-band transmission spectroscopy of sodium lines, simultaneous high-resolution spectral observation of the stellar activity indicators, such as Ca II H & K, H_α and Ca II IRT, reveals possible effects of stellar flaring activity on transmission spectra.
- We have developed a framework for narrow-band transmission spectroscopy. This framework can be applied on a higher quality data, for achieving more robust exoplanetary signals at higher confidence level.

Acknowledgements

S. Khalafinejad would like to firstly thank M. Holman for providing the required funding for visiting the Center for Astrophysics (CfA), where we could establish this work. In addition, we acknowledge *Deutsche Forschungsgemeinschaft (DFG),* in the framework of RTG 1351 and MIN faculty of Hamburg University for providing the second part of funding of this project. C. von Essen acknowledges funding for the Stellar Astrophysics Centre, provided by The Danish National Research Foundation (Grant DNRF106). We would also like to thank B. Fuhrmeister and S. Czesla and for their technical support and L. Fossati, M. Lindle, M. Guedel, T Lueftinger and J. Hoeijmakers for their scientific support and suggestions. We additionally appreciate the National Collaborative Research Infrastructure Strategy of the Australian Federal Government, who supported the access to the Magellan Telescopes. Finally, we thank contributors to Numpy (van der Walt et al., 2011), SciPy (Jones et al., 2001), Matplotlib (Hunter, 2007), the Python Programming Language, and the free and open-source community.

3.9 Supplementary sections

This section is not a part of the submitted manuscript and is added to the thesis for the comparison of our investigated targets.

3.9.1 HD189733b vs. WASP-17b

In order to be able to compare the results of HD 189733b to WASP-17b, we first need to make all the analysis steps identical. The method of calculation of the planetary absorption signal is different for each target (Section 2.4.3 Vs. Section 3.7.2.1). In the case of HD 189733b, we compared the ratio between the averaged exoplanetary sodium with the stellar sodium line at different passbands. This approach always contains the same amount of contribution from the planetary line and just the stellar line input changes at different integration band widths. We modified this flaw in the case of WASP-17b by averaging the values of the planetary Gaussian profile in different passbands. We re-calculated the absorption signals for HD 189733b and the final results after the modification of HD 189733b is shown in Table 3.6 and compared to WASP-17b.

Target	1 Å	1.5 Å	3 Å
HD 189733b	0.30 ± 0.14	0.18 ± 0.10	0.10 ± 0.04
WASP-17b	0.55 ± 0.43	0.40 ± 0.29	0.19 ± 0.15

TABLE 3.6: Modified measurements of the absorption signal in HD 189733b at each passband vs. absorption signals in WASP-17b (values are in percent)

In both targets only a single transit is observed, which has the advantage of saving the observing time and costs. However this caused the signal-to-noise of spectra around the sodium doublet not to be larger than ∼100 per pixel for the case of HD 189733b and not more than ∼ 80 for WASP-17b.

The confidence level of the measurements for WASP-17b is lower than HD 189733b, which is not surprising considering that WASP-17 is a star 4 magnitudes dimmer than HD 189733, the telescope used for the observation is 2 m smaller and the resolution of the instrument is also smaller. The larger scale height of WASP-17b cannot compensate for the difference in magnitudes and the telescope size.

The host star of HD 189733b is an active K-type star and the flaring activity of this star has affected the exoplanetary atmospheric signal. No strong flaring activity was observed in the host star of WASP-17b. Flaring activity can be mitigated in the excess light curve approach through comparisons to the activity indices or the equivalent widths. However, there is no clear way to mitigate their effects directly on the line shape in the division approach. Hence, the division approach was not applied on HD 189733b.

We can therefore only compare the targets in the light curve approach. In the comparative study of Sing et al. (2016), atmospheric models show an absorption in sodium doublet region of WASP-17b larger than the absorption signal in HD 189733b by about a factor of ∼2 (and the measured data is larger by a factor of 4). Comparing the results of our excess light curve measurements of WASP-17b to the results of sodium absorption in HD 189733b measured with the same method by Khalafinejad et al. (2017), we find a close difference between the targets: WASP-17b shows larger absorption signals

by factors of 1.8, 2.2, 1.9, at 1, 1.5, and 3 Å respectively. Still results from more targets are required to make a robust conclusion out of such a comparison.

Chapter 4

Outlook

This thesis focused on the development of an optimized framework for high-resolution transmission spectroscopy in a narrow wavelength band inside the broad atomic lines such as sodium.

To sum up, I used the spectral data of two inflated hot-Jupiters, HD 189733b and WASP 17b taken with the high-resolution ground-based echelle spectrograph, UVES, mounted on the 8.2-m VLT and MIKE on 6.5-m Magellan Telescopes, respectively. My analysis was based on two approaches, namely the excess light curve approach and the division approach, focused on Na double lines. In my framework the stellar flaring activity, stellar differential limb-darkening and the changing planetary RV effect, were carefully taken into consideration. Both planets revealed signatures of sodium at a confidence level between 2 to 3 σ. Through the changing planetary RV effect, I explained a bump that was typically observed in the exoplanetary atmospheric light curves. I also directly measured the shape of exoplanetary spectral line from the excess light curves. To complete this framework and obtain a physical description of the data, I used a radiative transfer atmospheric model and retrieved the exoplanetary temperature and radius. This framework can be quickly applied to other targets, in order to obtain a complete comparative view of exoplanetary atmospheres.

I begin this chapter by a discussion on the advantages, limitations and improvements of the high-resolution narrow-band transmission spectroscopy. I then make predictions about the achievements in exoplanetary research for the next 5 to 10 years.

4.1 Advantages, limitations and improvements

The high-resolution transmission spectroscopy in narrow bands inside broad stellar atomic lines (e.g. Na, K) is a strong method for unveiling the exoplanetary atmospheric properties.

The host star plays a very important role in hindering exoplanetary signatures, and high-resolution spectroscopy allows the identification and mitigation of the stellar originated effects. For instance, the cores of the spectral lines of Ca II H&K, H_α, and Ca II IRT are diagnosis of the stellar flaring activity. The broad wavelength coverage of high-resolution instruments such as UVES and MIKE is perfectly suitable for this purpose. Even a single transit observation of these instruments on board 6 to 10 meter ground-based facilities, can be sufficient to perform atmospheric studies on giant inflated exoplanets, orbiting bright stars. Hence, applying this method on a larger sample of giant exoplanets is relatively time-economic and quickly reachable.

Due to planetary orbital motion, high-resolution transmission spectroscopy, also provides the opportunity for the detection of the moving planetary signal inside the broad stellar line, hence it is possible to obtain clues about the shape of the exoplanetary spectral features from the excess light curve without any need for construction of the transmission spectra. This is very useful for the cases that the spectral lines are highly affected by the stellar activity.

Differential spectro-photometry broadly used in low-resolution transmission spectroscopy is limited by the availability of at least one comparison star in the field. However, through the high-resolution technique no reference stars are required, which allows self-calibration of the data. Hence, the high-resolution technique is applicable to larger samples.

The use of the high-resolution narrow-band technique also has some limitations. This technique is only applicable to broad lines. To search for narrow molecular lines such as water lines, TiO and VO, high-dispersion or low-resolution transmission spectroscopy must be applied. In addition, to investigate the scattering slopes at the optical blue part of the transmission spectra, we need to use differential spectro-photometry through the low-resolution technique. Moreover, the alignment precision in this technique depends on the spectral resolution and the signal-to-noise ratio (S/N) of the spectra. For example, spectra with resolution of $\sim$ 40,000 and S/N of $\sim$ 80 lead to an alignment precision of $\sim$ 0.004 Å. Hence, the narrow-band technique is limited by the spectral alignment precision.

The modelling framework developed in this thesis can be improved, first by investigating the effects of occulted spots through conducting simultaneous spectro-photometric observations and studying the anomalies in the light curve during the primary transit (see Section 1.3.1.1). Second, it is required to consider the stellar rotation effects which

causes a deformation of the stellar spectral lines and movements of the spectral line center (see Section 1.3.1.3). This effect was investigated through modelling the Rossiter-McLaughlin effect in Section 3.6.1 of this thesis. However, the effect was negligible in the case of WASP-17b, but generally it must be taken into account. Last but not least, is to take in to account the differential limb-darkening model in the division approach.

4.2 Future outlook

The field of exoplanetary science is rapidly growing. Within the next 5 to 10 years, we expect breakthroughs in the detection and characterization of many small and low-mass exoplanets, which brings us to the closest position to find an Earth-twin. There are also many open questions regarding planet formation, migration and evolution that still need to be addressed through the study of giant and mid-sized exoplanets. Over the last 15 years Hubble and Spitzer space telescopes as well as giant (10-m class) ground-based telescopes have made landmark contributions to the characterization of giant exoplanets and, since 2009, the Kepler space telescope has made a revolutionary impact on the detection of exoplanets and the understanding of the exoplanet population. In general, the majority of currently known exoplanetary host stars are relatively faint ($V > 10$), which means that only a handful of exoplanets are accessible to these characterization studies. To increase our understanding of exoplanets, especially smaller ones, planets around bright, cool stars need to be observed. There are several ongoing and upcoming missions that will address our current needs. In the following, I itemize some of our expected achievements through some of these missions:

- **Finding bright targets: TESS** will conduct a 2-year all sky survey to find planets around bright G, K and M type stars. Compared to the Kepler mission, TESS will observe 30-100 times brighter stars and it is expected to find a few thousand exoplanets, among which about 500 Earth-sized and super-Earth exoplanets are foreseen. Hence, TESS-discovered exoplanets will form an invaluable sample of prime candidates for in-depth characterization using JWST, CHEOPS and ground-based telescopes within the next decades. Since TESS targets will be bright, it is unlikely that a reference star with comparable brightness will be available within a reasonable field of view around the target. Therefore, applications of high-resolution transmission spectroscopy will play an important role in the atmospheric characterization of these targets.

- **Accurate radius measurements:** The **CHEOPS** mission will examine known exoplanets orbiting nearby and bright stars. CHEOPS will be able to measure the radius of rocky exoplanets with a precision (within 10% accuracy) even higher than TESS, hence it will yield accurate densities and planetary bulk compositions.

- **Expansion of the ground-based atmospheric studies over the Earth-size exoplanets: ESPRESSO** will be available soon on VLT. This instrument will characterize rocky and Earth-size exoplanets from the ground using the radial velocity method. Compared to HARPS, which has already greatly contributed to the detection and characterization of giant exoplanets, the stability and calibration accuracy of ESPRESSO is higher. Besides, it will be mounted on the 8.2-m VLT compared to 3.6-m La Silla. Hence, it will be capable of studying fainter targets and smaller exoplanets. Using high-resolution techniques ESPRESSO will also allow the atmospheric characterization of transiting and non-transiting rocky and Neptune-mass exoplanets.

- **Atmospheric characterization of a wide range of exoplanets:** Another breakthrough in the characterization of exoplanets is expected through take place with the advent of **JWST**. This space telescope, which is planned to be launched in 2019, will be able to obtain high-quality low-resolution transmission and dayside spectroscopy of a variety of exoplanets at wavelengths longer than 0.65 microns. Through the analysis of the JWST data, many of our current open questions, such as the origin and composition of exoplanets, will be addressed. For instance, we need to measure the C/O and metal abundances in both giant and terrestrial exoplanets to understand where in the protoplanetary disk the planet is formed. Furthermore, we should figure out how closely they match their hot star compositions and compare those with our Solar System planets. Moreover, as the most exciting part of JWST mission, the atmospheric characterization of Earth-like and super-Earth exoplanets will finally become possible(Greene et al., 2016). One of the limitations of JWST is that, it will not be able to observe at wavelengths shorter than $\sim$ 0.65 microns, while the information about the hazes and atomic sodium and potassium lines are in the scattering slope of the transmission spectrum in the blue and UV wavelengths. The primary selected targets of this mission (Stevenson et al., 2016) are observable from the ground using the current facilities. Complementary, ground-based observations from $\sim$ 0.35 - 0.7 microns, will be the key to interpret the exoplanetary atmosphere through a complete transmission spectrum.

- **Finding bio-signatures:** Within the next decade, with the commence of the 30 m-class generation of ground-based telescopes i.e., **GMT, TMT** and **ELT**, a revolution in ground-based exoplanetary characterization will take place. One of the most exciting achievements will be the robust detection of bio-signatures, such as O_3 and O_2 in the atmospheres of low-mass planets existing in the habitable zones of their host stars. Although such studies are very challenging and costly,

they are feasible through long-term high-resolution spectroscopic observations of these targets (e.g., Rodler & López-Morales, 2014).

- **Finding habitable exoplanets around M-dwarfs:** M-dwarfs are the most abundant type of stars. Their habitable zones are relatively close to them and since there is a relatively smaller contrast between the size and the mass of the small rocky exoplanets and small late-type stars, finding terrestrial planets around M-dwarfs is relatively easy. The ground-based attempts to find and characterize small rocky exoplanets in the habitable zone of M-dwarfs has already initiated. In addition, the occurrence rate of exoplanets with 0.5-4 $R_{\oplus}$ is relatively high (between 0.15 to 0.6 planet per an M-dwarf, Kopparapu, 2013; Dressing & Charbonneau, 2013). Currently, projects such as **MEarth** and **CARMENES** are focusing on the detection and characterization of such systems. MEarth has already started searching for terrestrial exoplanets around M-dwarfs using the transit detection technique, while CARMENES is searching for the same type of exoplanets using the radial velocity technique. Through other surveys and individual investigations also other terrestrial exoplanets around nearby stars have been detected. Two of the recent discoveries are the detection of several temperate terrestrial planets around TRAPPIST-1 (Gillon et al., 2017) and Proxima Centaury b as the closest terrestrial planet to the Earth (Anglada-Escudé et al., 2016). Applying the high-resolution transmission spectroscopy that I developed here, is also very useful to study exoplanets around M-dwarfs.

Not too long ago, finding an Earth-like planet capable of harbouring life outside the Solar System was just a topic of science fiction stories. So far, we have found some of the Earth-size exoplanets, and currently we are preparing the early stages of an in-depth characterization and understanding of these systems. The next decades of exoplanetary research mainly focus on the investigation of various planetary type formation and evolution scenarios as well as finding proper conditions for the formation of life on exoplanets.

Bibliography

Agol, E., Cowan, N. B., Knutson, H. A., et al. 2010, ApJ, 721, 1861

Albrecht, S. 2008, PhD thesis, Leiden Observatory, Leiden University, P.O. Box 9513, 2300 RA Leiden, The Netherlands

Albrecht, S., Winn, J. N., Marcy, G. W., et al. 2013, ApJ, 771, 11

Allart, R., Lovis, C., Pino, L., et al. 2017, A&A, 606, A144

Anderson, D. R., Hellier, C., Gillon, M., et al. 2010, ApJ, 709, 159

Anderson, D. R., Smith, A. M. S., Lanotte, A. A., et al. 2011, MNRAS, 416, 2108

Andretta, V., Busà, I., Gomez, M. T., & Terranegra, L. 2005, A&A, 430, 669

Anglada-Escudé, G., Amado, P. J., Barnes, J., et al. 2016, Nature, 536, 437

Barman, T. S., Macintosh, B., Konopacky, Q. M., & Marois, C. 2011, ApJ, 733, 65

Basri, G., Borucki, W. J., & Koch, D. 2005, New A Rev., 49, 478

Bayliss, D. D. R., Winn, J. N., Mardling, R. A., & Sackett, P. D. 2010, ApJ, 722, L224

Bean, J. L., Désert, J.-M., Seifahrt, A., et al. 2013, ApJ, 771, 108

Beaulieu, J.-P., Bennett, D. P., Fouqué, P., et al. 2006, Nature, 439, 437

Bento, J., Wheatley, P. J., Copperwheat, C. M., et al. 2014, MNRAS, 437, 1511

Berta-Thompson, Z. K., Irwin, J., Charbonneau, D., et al. 2015, Nature, 527, 204

Bienayme, O. & Turon, C., eds. 2002, EAS Publications Series, Vol. 2, GAIA : a European space project

Birkby, J. L., de Kok, R. J., Brogi, M., et al. 2013, MNRAS, 436, L35

Birkby, J. L., de Kok, R. J., Brogi, M., Schwarz, H., & Snellen, I. A. G. 2017, AJ, 153, 138

Blecic, J. 2016, ArXiv e-prints

Blecic, J., Harrington, J., & Bowman, M. O. 2016, ApJS, 225, 4

Bonnefoy, M., Zurlo, A., Baudino, J. L., et al. 2016, A&A, 587, A58

Borkovits, T., Rappaport, S., Hajdu, T., & Sztakovics, J. 2015, MNRAS, 448, 946

Borucki, W. J., Koch, D., Basri, G., et al. 2010, Science, 327, 977

Borucki, W. J., Koch, D., Jenkins, J., et al. 2009, Science, 325, 709

Borucki, W. J., Koch, D. G., Lissauer, J. J., et al. 2003, in Proc. SPIE, Vol. 4854, Future EUV/UV and Visible Space Astrophysics Missions and Instrumentation., ed. J. C. Blades & O. H. W. Siegmund, 129–140

Bouchy, F., Moutou, C., Queloz, D., & the CoRoT Exoplanet Science Team. 2009, ArXiv e-prints

Bourrier, V., Lecavelier des Etangs, A., Ehrenreich, D., Tanaka, Y. A., & Vidotto, A. A. 2016, A&A, 591, A121

Bourrier, V., Lecavelier des Etangs, A., & Vidal-Madjar, A. 2015, A&A, 573, A11

Boyajian, T., von Braun, K., Feiden, G. A., et al. 2015, MNRAS, 447, 846

Broeg, C., Fortier, A., Ehrenreich, D., et al. 2013, in European Physical Journal Web of Conferences, Vol. 47, European Physical Journal Web of Conferences, 03005

Brogi, M., de Kok, R. J., Albrecht, S., et al. 2016, ApJ, 817, 106
Brogi, M., Snellen, I. A. G., de Kok, R. J., et al. 2012, Nature, 486, 502
Brown, T. M. 2001, ApJ, 553, 1006
Burrows, A., Marley, M. S., & Sharp, C. M. 2000, ApJ, 531, 438
Burrows, A. S. 2014, Nature, 513, 345
Busà, I., Aznar Cuadrado, R., Terranegra, L., Andretta, V., & Gomez, M. T. 2007, A&A, 466, 1089
Carter, J. A., Agol, E., Chaplin, W. J., et al. 2012, Science, 337, 556
Catala, C., Auvergne, M., Baglin, A., et al. 1995, in ESA Special Publication, Vol. 376, Helioseismology, 549
Catalano, S., Biazzo, K., Frasca, A., et al. 2002, Astronomische Nachrichten, 323, 260
Cauley, P. W., Redfield, S., & Jensen, A. G. 2017a, ArXiv e-prints
Cauley, P. W., Redfield, S., & Jensen, A. G. 2017b, AJ, 153, 81
Cauley, P. W., Redfield, S., Jensen, A. G., & Barman, T. 2016, AJ, 152, 20
Cauley, P. W., Redfield, S., Jensen, A. G., et al. 2015, ApJ, 810, 13
Cegla, H. M., Lovis, C., Bourrier, V., et al. 2016, A&A, 588, A127
Cessateur, G., Kretzschmar, M., Dudok de Wit, T., & Boumier, P. 2010, Sol. Phys., 263, 153
Charbonneau, D., Brown, T. M., Latham, D. W., & Mayor, M. 2000, ApJ, 529, L45
Charbonneau, D., Brown, T. M., Noyes, R. W., & Gilliland, R. L. 2002, ApJ, 568, 377
Chauvin, G., Lagrange, A.-M., Dumas, C., et al. 2004, A&A, 425, L29
Chmielewski, Y. 2000, A&A, 353, 666
Cincunegui, C., Díaz, R. F., & Mauas, P. J. D. 2007, A&A, 469, 309
Crossfield, I. J. M., Barman, T., & Hansen, B. M. S. 2011, ApJ, 736, 132
Crossfield, I. J. M., Hansen, B. M. S., Harrington, J., et al. 2010, ApJ, 723, 1436
Cubillos, P., Harrington, J., Loredo, T. J., et al. 2017, AJ, 153, 3
Cubillos, P. E. 2016, ArXiv e-prints
Currie, T., Burrows, A., Madhusudhan, N., et al. 2013, ApJ, 776, 15
Currie, T., Debes, J., Rodigas, T. J., et al. 2012, ApJ, 760, L32
Czesla, S., Huber, K. F., Wolter, U., Schröter, S., & Schmitt, J. H. M. M. 2009, A&A, 505, 1277
Czesla, S., Klocová, T., Khalafinejad, S., Wolter, U., & Schmitt, J. H. M. M. 2015, A&A, 582, A51
Czesla, S., Molle, T., & Schmitt, J. H. M. M. 2017, ArXiv e-prints
de Kok, R. J., Brogi, M., Snellen, I. A. G., et al. 2013, A&A, 554, A82
Dekker, H., D'Odorico, S., Kaufer, A., Delabre, B., & Kotzlowski, H. 2000, in Society of Photo-Optical Instrumentation Engineers (SPIE) Conference Series, Vol. 4008, Optical and IR Telescope Instrumentation and Detectors, ed. M. Iye & A. F. Moorwood, 534–545
Deming, D., Seager, S., Harrington, J., & Richardson, L. J. 2005, Spitzer Proposal, 260
Deming, D., Wilkins, A., McCullough, P., et al. 2013, ApJ, 774, 95
Demory, B.-O., Gillon, M., de Wit, J., et al. 2016, Nature, 532, 207
Demory, B.-O., Gillon, M., Seager, S., et al. 2012, Spitzer Proposal, 90208
Désert, J.-M., Lecavelier des Etangs, A., Hébrard, G., et al. 2009, ApJ, 699, 478
Désert, J.-M., Sing, D., Vidal-Madjar, A., et al. 2011, A&A, 526, A12
Désert, J.-M., Vidal-Madjar, A., Lecavelier Des Etangs, A., et al. 2008, A&A, 492, 585
Di Gloria, E., Snellen, I. A. G., & Albrecht, S. 2015, A&A, 580, A84
Dravins, D., Ludwig, H.-G., Dahlen, E., & Pazira, H. 2015, in Cambridge Workshop on Cool Stars, Stellar Systems, and the Sun, Vol. 18, 18th Cambridge Workshop on Cool Stars, Stellar Systems, and the Sun, ed. G. T. van Belle & H. C. Harris, 853–868
Dreizler, S., Reiners, A., Homeier, D., & Noll, M. 2009, A&A, 499, 615
Dressing, C. D. & Charbonneau, D. 2013, ApJ, 767, 95
Dumusque, X., Pepe, F., Lovis, C., et al. 2012, Nature, 491, 207

Dumusque, X., Santos, N. C., Udry, S., Lovis, C., & Bonfils, X. 2011, A&A, 527, A82

Duncan, D. K., Vaughan, A. H., Wilson, O. C., et al. 1991, ApJS, 76, 383

Dyudina, U., Zhang, X., Li, L., et al. 2016, ApJ, 822, 76

Ehrenreich, D., Bourrier, V., Wheatley, P. J., et al. 2015, Nature, 522, 459

Faigler, S. & Mazeh, T. 2011, MNRAS, 415, 3921

Fischer, P. D., Knutson, H. A., Sing, D. K., et al. 2016, ApJ, 827, 19

Foreman-Mackey, D., Conley, A., Meierjurgen Farr, W., et al. 2013, emcee: The MCMC Hammer, Astrophysics Source Code Library

Fortney, J. J., Shabram, M., Showman, A. P., et al. 2010, ApJ, 709, 1396

Frasca, A., Biazzo, K., Catalano, S., et al. 2005, A&A, 432, 647

Fressin, F., Torres, G., Charbonneau, D., et al. 2013, ApJ, 766, 81

Fulton, B. J., Petigura, E. A., Howard, A. W., et al. 2017, AJ, 154, 109

Gaia Collaboration, Prusti, T., de Bruijne, J. H. J., et al. 2016, A&A, 595, A1

Gardner, J. P., Mather, J. C., Clampin, M., et al. 2006, Space Sci. Rev., 123, 485

Gaudi, B. S. & Winn, J. N. 2007, ApJ, 655, 550

Gibson, N. P., Aigrain, S., Barstow, J. K., et al. 2013, MNRAS, 428, 3680

Gillon, M., Triaud, A. H. M. J., Demory, B.-O., et al. 2017, Nature, 542, 456

Goodman, J. & Weare, J. 2010, Communications in applied mathematics and computational science, 5, 65

Gould, A., Udalski, A., Shin, I.-G., et al. 2014, Science, 345, 46

Gray, D. F. 2004, Advances in Space Research, 34, 308

Greene, T. P., Line, M. R., Montero, C., et al. 2016, ApJ, 817, 17

Hartman, J. D., Bakos, G., Stanek, K. Z., & Noyes, R. W. 2004a, AJ, 128, 1761

Hartman, J. D., Bakos, G., Stanek, K. Z., & Noyes, R. W. 2004b, AJ, 128, 1761

Hastings, W. 1970, Biometrika, 57, 97

Haswell, C. A. 2010, Transiting Exoplanets (Cambridge CB2 8RU,UK: Cambridge University Press)

Hauschildt, P. H. & Baron, E. 1999, Journal of Computational and Applied Mathematics, 109, 41

Heng, K. 2016, ApJ, 826, L16

Heng, K., Wyttenbach, A., Lavie, B., et al. 2015, ApJ, 803, L9

Henry, G. W. & Winn, J. N. 2008, AJ, 135, 68

Hoeijmakers, H. J., de Kok, R. J., Snellen, I. A. G., et al. 2015, A&A, 575, A20

Høg, E., Fabricius, C., Makarov, V. V., et al. 2000, A&A, 355, L27

Holman, M. J. & Murray, N. W. 2005, Science, 307, 1288

Huitson, C. M., Sing, D. K., Vidal-Madjar, A., et al. 2012, MNRAS, 422, 2477

Hunter, J. D. 2007, Computing In Science & Engineering, 9, 90

Husser, T.-O., Kamann, S., & Dreizler, S. 2015, A&A submitted

Husser, T.-O. & Ulbrich, K. 2014, in Astronomical Society of India Conference Series, Vol. 11, Astronomical Society of India Conference Series, 53–56

Husser, T.-O., Wende-von Berg, S., Dreizler, S., et al. 2013, A&A, 553, A6

Jensen, A. G., Redfield, S., Endl, M., et al. 2012, ApJ, 751, 86

Jensen, A. G., Redfield, S., Endl, M., et al. 2011, ApJ, 743, 203

Johnson, J. A., Winn, J. N., Bakos, G. Á., et al. 2011, ApJ, 735, 24

Jones, E., Oliphant, T., Peterson, P., et al. 2001, SciPy: Open source scientific tools for Python, [Online; accessed 2017-02-12]

Kane, S. R., Horne, K., Street, R. A., et al. 2003, in Astronomical Society of the Pacific Conference Series, Vol. 294, Scientific Frontiers in Research on Extrasolar Planets, ed. D. Deming & S. Seager, 387–390

Kempton, E. M.-R., Perna, R., & Heng, K. 2014, ApJ, 795, 24

Khalafinejad, S., von Essen, C., Hoeijmakers, H. J., et al. 2017, A&A, 598
Kilpatrick, B. M., Lewis, N. K., Kataria, T., et al. 2017, AJ, 153, 22
Klocova, T., Czesla, S., Khalafinejad, S., Wolter, U., & Schmitt, J. H. M. M. 2017, ArXiv e-prints
Knutson, H. A., Charbonneau, D., Allen, L. E., et al. 2007, Nature, 447, 183
Koch, D. G., Borucki, W. J., Basri, G., et al. 2010, ApJ, 713, L79
Kochukhov, O., Bagnulo, S., Wade, G. A., et al. 2004, A&A, 414, 613
Konopacky, Q. M., Barman, T. S., Macintosh, B. A., & Marois, C. 2013, Science, 339, 1398
Kopal, Z. 1950, Harvard College Observatory Circular, 454, 1
Kopparapu, R. K. 2013, ApJ, 767, L8
Kreidberg, L., Bean, J. L., Désert, J.-M., et al. 2014, Nature, 505, 69
Kreidberg, L., Line, M. R., Bean, J. L., et al. 2015, ApJ, 814, 66
Kreidberg, L. & Loeb, A. 2016, ApJ, 832, L12
Kulow, J. R., France, K., Linsky, J., & Loyd, R. O. P. 2014, ApJ, 786, 132
Lagrange, A.-M., Gratadour, D., Chauvin, G., et al. 2009, A&A, 493, L21
Lecavelier Des Etangs, A., Pont, F., Vidal-Madjar, A., & Sing, D. 2008, A&A, 481, L83
Lin, D. N. C., Bodenheimer, P., & Richardson, D. C. 1996, Nature, 380, 606
Llama, J. & Shkolnik, E. L. 2015, ApJ, 802, 41
Lockwood, A. C., Johnson, J. A., Bender, C. F., et al. 2014, ApJ, 783, L29
Louden, T. & Wheatley, P. J. 2015, ApJ, 814, L24
Lovis, C., Snellen, I., Mouillet, D., et al. 2017, A&A, 599, A16
Lüftinger, T., Fröhlich, H.-E., Weiss, W. W., et al. 2010, A&A, 509, A43
Macintosh, B., Graham, J. R., Ingraham, P., et al. 2014, Proceedings of the National Academy of Science, 111, 12661
Mancini, L., Esposito, M., Covino, E., et al. 2015, A&A, 579, A136
Mandel, K. & Agol, E. 2002, ApJ, 580, L171
Mandell, A. M., Haynes, K., Sinukoff, E., et al. 2013, ApJ, 779, 128
Marois, C., Zuckerman, B., Konopacky, Q. M., Macintosh, B., & Barman, T. 2010, Nature, 468, 1080
Martínez-Arnáiz, R., Maldonado, J., Montes, D., Eiroa, C., & Montesinos, B. 2010, A&A, 520, A79
Mayor, M., Lovis, C., & Santos, N. C. 2014, Nature, 513, 328
Mayor, M. & Queloz, D. 1995, Nature, 378, 355
Mayor, M., Udry, S., Naef, D., et al. 2004, A&A, 415, 391
McCullough, P. R., Crouzet, N., Deming, D., & Madhusudhan, N. 2014, ApJ, 791, 55
McLaughlin, D. B. 1924, ApJ, 60
Mesa, D., Gratton, R., Berton, A., et al. 2011, A&A, 529, A131
Metropolis, N., Rosenbluth, A. W., Rosenbluth, M. N., Teller, A. H., & Teller, E. 1953, J. Chem. Phys., 21, 1087
Millholland, S. & Laughlin, G. 2017, AJ, 154, 83
Moehler, S., Modigliani, A., Freudling, W., et al. 2014, A&A, 568, A9
Morley, C. V., Fortney, J. J., Marley, M. S., et al. 2015, ApJ, 815, 110
Motalebi, F., Udry, S., Gillon, M., et al. 2015, A&A, 584, A72
Müller, H. M. 2016, Limb-darkening Measurements on Exoplanet Host Stars and the Sun
Muterspaugh, M. W., Lane, B. F., Kulkarni, S. R., et al. 2010, AJ, 140, 1657
Nikolov, N., Sing, D. K., Burrows, A. S., et al. 2015, MNRAS, 447, 463
Nortmann, L., Dreizler, S., Bean, J. L., & Barman, T. 2015, submitted to A&A
Nortmann, L., Pallé, E., Murgas, F., et al. 2016, A&A, 594, A65
Ohta, Y., Taruya, A., & Suto, Y. 2005, ApJ, 622, 1118
O'Neal, D., Saar, S. H., & Neff, J. E. 1996, ApJ, 463, 766
Oshagh, M., Santos, N. C., Boisse, I., et al. 2013, A&A, 556, A19

Oshagh, M., Santos, N. C., Ehrenreich, D., et al. 2014, A&A, 568, A99
Owen, J. E. & Wu, Y. 2017, ArXiv e-prints
Pepe, F., Mayor, M., Delabre, B., et al. 2000, in Proc. SPIE, Vol. 4008, Optical and IR Telescope Instrumentation and Detectors, ed. M. Iye & A. F. Moorwood, 582–592
Perryman, M., Hartman, J., Bakos, G. Á., & Lindegren, L. 2014, ApJ, 797, 14
Piskunov, N. & Kochukhov, O. 2002, A&A, 381, 736
Placek, B., Knuth, K. H., & Angerhausen, D. 2014, ApJ, 795, 112
Pollacco, D. 2005, Astronomy and Geophysics, 46, 1.19
Pollacco, D. L., Skillen, I., Collier Cameron, A., et al. 2006, PASP, 118, 1407
Pont, F., Bouchy, F., Melo, C., et al. 2005, A&A, 438, 1123
Pont, F., Gilliland, R. L., Moutou, C., et al. 2007, A&A, 476, 1347
Pont, F., Knutson, H., Gilliland, R. L., Moutou, C., & Charbonneau, D. 2008, MNRAS, 385, 109
Pont, F., Sing, D. K., Gibson, N. P., et al. 2012, ArXiv e-prints
Pont, F., Sing, D. K., Gibson, N. P., et al. 2013, MNRAS, 432, 2917
Poppenhaeger, K., Schmitt, J. H. M. M., & Wolk, S. J. 2013, ApJ, 773, 62
Quanz, S. P., Crossfield, I., Meyer, M. R., Schmalzl, E., & Held, J. 2015, International Journal of Astrobiology, 14, 279
Quanz, S. P., Schmid, H. M., Geissler, K., et al. 2011, ApJ, 738, 23
Quintana, E. V., Barclay, T., Raymond, S. N., et al. 2014, Science, 344, 277
Ranalli, P., Hobbs, D., & Lindegren, L. 2017, ArXiv e-prints
Redfield, S., Endl, M., Cochran, W. D., & Koesterke, L. 2008, ApJ, 673, L87
Reiners, A. 2012, Living Reviews in Solar Physics, 9, 1
Ricker, G. R., Winn, J. N., Vanderspek, R., et al. 2015, Journal of Astronomical Telescopes, Instruments, and Systems, 1, 014003
Rodler, F. & López-Morales, M. 2014, ApJ, 781, 54
Rodler, F., Lopez-Morales, M., & Ribas, I. 2012, ApJ, 753, L25
Rossiter, R. A. 1924, ApJ, 60
Rudolf, N., Günther, H. M., Schneider, P. C., & Schmitt, J. H. M. M. 2016, A&A, 585, A113
Sackett, P. D. 1999, in NATO Advanced Science Institutes (ASI) Series C, Vol. 532, NATO Advanced Science Institutes (ASI) Series C, ed. J.-M. Mariotti & D. Alloin, 189
Sahlmann, J., Lazorenko, P. F., Ségransan, D., et al. 2014, A&A, 565, A20
Salz, M., Schneider, P. C., Czesla, S., & Schmitt, J. H. M. M. 2016, A&A, 585, L2
Sanchis-Ojeda, R., Winn, J. N., Marcy, G. W., et al. 2013, ApJ, 775, 54
Schneider, J. 2011, in EPSC-DPS Joint Meeting 2011, 3
Schneider, J. & Chevreton, M. 1990, A&A, 232, 251
Schwarz, G. 1978, The annals of statistics, 6, 461
Schwarz, R., Haghighipour, N., Eggl, S., Pilat-Lohinger, E., & Funk, B. 2011, MNRAS, 414, 2763
Seager, S. 2014, Proceedings of the National Academy of Science, 111, 12634
Seager, S. & Mallén-Ornelas, G. 2003, ApJ, 585, 1038
Seager, S. & Sasselov, D. D. 2000, ApJ, 537, 916
Sedaghati, E., Boffin, H. M., Jeřabková, T., et al. 2016, ArXiv e-prints
Sedaghati, E., Boffin, H. M. J., MacDonald, R. J., et al. 2017, Nature, 549, 238
Selsis, F., Wordsworth, R. D., & Forget, F. 2011, A&A, 532, A1
Shporer, A. & Hu, R. 2015, AJ, 150, 112
Sing, D. K., Fortney, J. J., Nikolov, N., et al. 2016, Nature, 529, 59
Sing, D. K., Huitson, C. M., Lopez-Morales, M., et al. 2012, MNRAS, 426, 1663
Sing, D. K., Lecavelier des Etangs, A., Fortney, J. J., et al. 2013, MNRAS, 436, 2956
Sing, D. K., Pont, F., Aigrain, S., et al. 2011, MNRAS, 416, 1443

Sing, D. K., Vidal-Madjar, A., Désert, J.-M., Lecavelier des Etangs, A., & Ballester, G. 2008, ApJ, 686, 658

Smette, A., Sana, H., Noll, S., et al. 2015, A&A, 576, A77

Snellen, I., de Kok, R., Birkby, J. L., et al. 2015, A&A, 576, A59

Snellen, I. A. G. 2004, MNRAS, 353, L1

Snellen, I. A. G., Albrecht, S., de Mooij, E. J. W., & Le Poole, R. S. 2008, A&A, 487, 357

Snellen, I. A. G., de Kok, R. J., de Mooij, E. J. W., & Albrecht, S. 2010, Nature, 465, 1049

Sparks, W. B. & Ford, H. C. 2002, ApJ, 578, 543

Stevenson, K. B., Lewis, N. K., Bean, J. L., et al. 2016, PASP, 128, 094401

Strassmeier, K. G. 2002, Astronomische Nachrichten, 323, 309

Tennyson, J., Yurchenko, S. N., Al-Refaie, A. F., et al. 2016, Journal of Molecular Spectroscopy, 327, 73

Tinetti, G., Carey, S., Allard, N., et al. 2007, Spitzer Proposal, 461

Tinetti, G., Deroo, P., Swain, M. R., et al. 2010, ApJ, 712, L139

Torres, G., Winn, J. N., & Holman, M. J. 2008, ApJ, 677, 1324

Traub, W. A. & Oppenheimer, B. R. 2010, Direct Imaging of Exoplanets, ed. S. Seager, 111–156

Triaud, A. H. M. J., Collier Cameron, A., Queloz, D., et al. 2010, A&A, 524, A25

van der Walt, S., Colbert, S. C., & Varoquaux, G. 2011, Computing in Science & Engineering, 13, 22

Vidal-Madjar, A., Désert, J.-M., Lecavelier des Etangs, A., et al. 2004, ApJ, 604, L69

Vidal-Madjar, A., Lecavelier des Etangs, A., Désert, J.-M., et al. 2003, Nature, 422, 143

Vidal-Madjar, A., Sing, D. K., Lecavelier Des Etangs, A., et al. 2011, A&A, 527, A110

von Essen, C., Schröter, S., Agol, E., & Schmitt, J. H. M. M. 2013, A&A, 555, A92

Wakeford, H. R., Sing, D. K., Evans, T., Deming, D., & Mandell, A. 2016, ApJ, 819, 10

William H. Press, Saul A. Teukolsky, W. T. V. B. P. F. 2002, Numerical Recipes in C++ (Cambridge CB2 8RU,UK: Cambridge University Press)

Winn, J. N. 2007, in Astronomical Society of the Pacific Conference Series, Vol. 366, Transiting Extrapolar Planets Workshop, ed. C. Afonso, D. Weldrake, & T. Henning, 170

Winn, J. N., Holman, M. J., Henry, G. W., et al. 2007, AJ, 133, 1828

Winn, J. N., Howard, A. W., Johnson, J. A., et al. 2011, AJ, 141, 63

Wolszczan, A. & Frail, D. A. 1992, Nature, 355, 145

Wolter, U., Schmitt, J. H. M. M., Huber, K. F., et al. 2009, A&A, 504, 561

Wolter, U., Schmitt, J. H. M. M., & van Wyk, F. 2005, A&A, 435, 261

Wood, P. L., Maxted, P. F. L., Smalley, B., & Iro, N. 2011, MNRAS, 412, 2376

Wyttenbach, A., Ehrenreich, D., Lovis, C., Udry, S., & Pepe, F. 2015, A&A, 577, A62

Wyttenbach, A., Lovis, C., Ehrenreich, D., et al. 2017, A&A, 602, A36

Yan, F., Fosbury, R. A. E., Petr-Gotzens, M. G., Pallé, E., & Zhao, G. 2015, ApJ, 806, L23

Yee, J. C., Han, C., Gould, A., et al. 2014, ApJ, 790, 14

Zeng, L., Sasselov, D. D., & Jacobsen, S. B. 2016, ApJ, 819, 127

Zhou, G. & Bayliss, D. D. R. 2012, MNRAS, 426, 2483

Zurlo, A., Vigan, A., Galicher, R., et al. 2016, A&A, 587, A57

Acknowledgements

I am grateful to many people, from family, friends and colleagues, who helped me in different ways to accomplish my academic studies. I became passionate for astronomy since I joined Shiraz Astronomical Society during my high school time and afterwards I decided to professionally pursue observational astronomy. To achieve this goal, after finishing my bachelor in Physics at Shiraz University, I started my master in astronomy at Leiden Observatory in the Netherlands and later my PhD at Hamburg Observatory, in Germany. Studying abroad was not only an advantage for me to deeply dig into modern observational astronomy, but also it opened my views about life and humanity. During my studies at Shiraz, Leiden and Hamburg Universities, and during my short-term research stay at Harvard-Smithsonian Center for Astrophysics (CfA) and Vienna Observatory, I have met a lot of nice and helpful friends and colleagues, who have assisted me in scientific achievements and/or in social life.

First of all, I would like to thank Jürgen Schmitt, who hired me as a PhD student and gave me the opportunity to grow independently in the world of science. You gave me the freedom to define my own research project and to make my own international scientific collaboration network which I believe both are very important in performing a successful project. I am grateful to my co-advisor Stefan Dreizler. We had the chance to meet during the regular meetings of the Hamburg-Göttingen research training group (DFG Graduiertenkolleg 1351) and also through Skype whenever needed. In addition to your scientific support, I would like to thank your positive moral attitudes which were always inspiring for me.

I appreciate Carolina von Essen, for all her help and advise regarding the PhD projects and for the very warm friendship. I will never forget the day that I arrived to Hamburg and you welcomed me at the train station. I am thankful to Michael Salz and Birgit Fuhermeister for proofreading my thesis and giving me useful feed-backs. I have found both of you very helpful and calm people during all these four years that we shared an office with each other.

Living in Hamburg would be very difficult without the presence of friends such as Volker, Imola and Sebatian. Thank you for all of your help including assistance regarding legal issues and taxes! I will always praise your open social interactions and your preference of humanity over nationality. Volker, thank you for helping in the German transition of the abstract and for inviting me and my family to have delicious Hungarian meals.

I would like to simply say thank you to many other friends and colleagues at Hamburg Observatory who helped me in different aspects regarding scientific problems or technical issues, specifically, Stefan Czesla, Uwe Wolter, Holger Müller, Tereza Klocova, Tobias Schmidt, Panos Ioannidis, and Johannes Martin. In addition, I acknowledge, Angelika,

Anke, Wiebke and Astrid, for not only solving the administration and bureaucratic issues, but also for your energetic smiles, and all the plannings for the Christmas parties of the observatory. I appreciate Shadi, Mahya, Afsaneh, and Bahar for holding the social programs in the Iranian community which helped me to survive the loneliness of living in Germany.

I am grateful to Matthew Holman for providing me the opportunity of research stay at CfA and I would like to thank Matthew Payne for his mentorship during the first few months of my stay. In addition, I am very thankful to Mercedes Lopez-Morales and George Zhou for the collaboration that started there and made the platform of my last publication.

Through my frequent visits to Austria, I was delighted to meet Manuel Güdel and Theresa Lüftinger from Vienna Observatory as well as Luca Fossati, Monika Lendl and Patricio Cubillos from Graz space research center. I appreciate communication and the useful scientific discussions with all these researchers, which were very helpful and effective for my scientific work. Manuel, I additionally thank you for offering me a postdoc position, however unexpected transfer of my husband from Vienna to Heidelberg now may change my plans regarding moving to Vienna, but anyways I look forward to having a close collaboration with all of you soon.

I am thankful to Jens Hoeijmakers for continuation of the friendship and scientific collaboration that started during my master studies in Leiden. In addition, I am grateful to Koen Maaskant and Alexander Tielens for their mentorship on the short-term reach project on the study of the gaps in protoplanetary disks which started in Leiden and ended in my first PhD publication (not included in this thesis).

Back to my high school and bachelor time in Iran, I would like to thank Mr. Lashani, the first person who inspired me with the beauties of the night sky through a night expedition in the suburb of Shiraz, and Mr. Shirabadi, my very talented high school teacher, who helped me to deeply perceive the basics and the beauties of physics. I am also grateful to Ali Dariush, Ahmad Poostforoush, Mehdi Jahanmiri,and Nematollah Riazi, whose very interesting undergraduate courses highly motivated me and made me to continue with astronomy.

More than anyone else, I owe a huge debt of gratitude to my parents, who have been my main supporters everywhere, in all times. Living far away from you, for seven years now, has been very difficult, but your support, love and affection were always with me, even from a distance of 5000 km. You both are the strongest and most successful people I have ever known and I am truly proud of you. Father, I miss you very much and the saddest thing in my life is not to be able to see you anymore. Mother, you are my treasure, thank you for your unlimited source of love! I am also thankful for my beloved brother, Saeed for inspiring me with science and technology since childhood, for supporting me and believing in me all the time. I also acknowledge my parents

in law and grandmother in law for their everyday moral support and affection, during the last few years. Finally, I have a few words for my ever lasting love and my closest friend, Mohammad. We got married almost the same time that I started my PhD. Although, the constraints of life has not yet allowed us to live together in one city, your companionship has been with me all the time during these years. You are my happiness and my strongest source of positive feelings and peace. You gave me self-confidence and made me calm whenever I was stressed about my work. Also thank you for your help in corrections of the figures of my thesis. Without your presence and love, I would not be able to accomplish my PhD; without your shine, my sky would be very dark anywhere I was!

Eidesstattliche Versicherung / Declaration on oath

Hiermit versichere ich an Eides statt, die vorliegende Dissertationsschrift selbst verfasst und keine anderen als die angegebenen Hilfsmittel und Quellen benutzt zu haben. Die eingereichte schriftliche Fassung entspricht der auf dem elektronischen Speichermedium. Die Dissertation wurde in der vorgelegten oder einer ahnlichen Form nicht schon einmal in einem fruheren Promotionsverfahren angenommen oder als ungenugend beurteilt.

Hamburg, den Unterschrift